Cross-correlation of Stochastic Gravitational Wave Background and Galaxy Number Counts and Its Angular Power Spectrum

A DISSERTATION
SUBMITTED TO THE FACULTY OF THE GRADUATE SCHOOL
OF THE UNIVERSITY OF MINNESOTA
BY

Kate Ziyan Yang

IN PARTIAL FULFILLMENT OF THE REQUIREMENTS
FOR THE DEGREE OF
DOCTOR OF PHILOSOPHY

Vuk Mandic

September, 2025

Acknowledgements

I am very grateful to these people who helped me during my time in graduate school. I thank Prof. Vuk Mandic guiding me as my advisor throughout my eight years of studying and researching, without whom finish this dissertation would not be possible. I also thank Prof. Claudia Scarlata, who is also my committee chair, for providing innumerable help and advices on my research. I thank Dr. Andrew Matas for helping me to start when I first joined the group in the spring semester of 2018. I also thank Dr. Sharan Banagiri for introducing me to his research and offering generous help as a nice cooperator to my research. I benefit a lot from the pleasant atmosphere of our group, so I must mention the kindness of our group members: Dr. Rich Ormiston, Erik Floden, Alex Granados, ... thank you all for being so friendly to me.

Dedication

To Mom and Dad.

Abstract

In this dissertation, I present my study of the cross-correlation between the anisotropy in stochastic gravitational-wave background (SGWB) and the distribution of galaxies across the sky. This study will improve the sensitivity of future searches for anisotropy in the SGWB and expand the use of SGWB anisotropy to probe the formation of structure in the Universe. It has three parts.

First, I use the spherical harmonic decomposition of the anisotropic SGWB measured in the second observing run (O2) of LIGO in 50 Hz-wide frequency bands and convert them into pixel-based sky maps in HEALPIX basis. Then I take the galaxies in the Sloan Digital Sky Survey (SDSS) photometric and spectroscopic catalog in 0.1-wide redshift bins and count them in pixels of HEALPIX basis to form number count sky maps at the same angular resolution as the SGWB maps. I compute the pixel-based coherence between the SGWB maps in frequency bands and galaxy count maps in redshift bins and find that the coherence is dominated by the null measurement noise in the SGWB maps and is not statistically significant.

Second, I use the anisotropic SGWB measured in the first three observing runs (O1-O3) of LIGO in 10 Hz-wide frequency bins and galaxy count over-density from the SDSS spectroscopic catalog without binning in redshift to compute the angular power spectra of their auto-correlations and cross-correlation. I compare the observed cross-correlation to the spectra predicted by astrophysical models. I apply a Bayesian formalism to explore the parameter space of the theoretical models, and I set constraints on a set of astrophysical parameters of the astrophysical kernel describing the galactic process of gravitational-wave (GW) emission with or without the inclusion of shot noise.

Third, I estimate the amplitude and spatial anisotropy in the SGWB energy density due to compact binary coalescence (CBC) events occurring in galaxies in the Flagship Mock Catalogue developed by the Euclid Consortium. For each galaxy in the catalogue, I use the simulated stellar mass and star formation to constrain the galaxy's star formation history and predict its contribution to the SGWB. I also compare these predictions to the astrophysical models above and explore the parameter space with an ideal covariance dominated by cosmic variance to set constraints on the parameters.

Contents

List of Tables

List of Figures

Chapter 1

Gravitational Waves

1.1 General Relativity

1.1.1 Special Relativity

The Principle of Special Relativity proposed by Einstein in 1905 states that the laws of nature are invariant under Lorentz space-time coordinate transformations. Following the structures and notations in [1], let's introduce the invariant spacetime interval that is defined as

$$\mathrm{d}s^2 = -c^2\,\mathrm{d}t^2 + \mathrm{d}x^2 + \mathrm{d}y^2 + \mathrm{d}z^2\,, \tag{1.1}$$

where c denotes speed of light, t is time and x, y, z are spatial coordinates. The above equation can be expressed by the contraction of a four-dimensional vector dx^μ:

$$\mathrm{d}s^2 = \eta_{\mu\nu}\,\mathrm{d}x^\mu\,\mathrm{d}x^\nu\,, \tag{1.2}$$

with $\eta_{\mu\nu}$ being the Minkowski space-time metric tensor

$$\eta_{\mu\nu} = \begin{pmatrix} -1 & 0 & 0 & 0 \\ 0 & 1 & 0 & 0 \\ 0 & 0 & 1 & 0 \\ 0 & 0 & 0 & 1 \end{pmatrix}, \tag{1.3}$$

and the subscripts μ, ν go over 0 to 3 as time, x, y and z, so ds^2 is summed over all four dimensions.

From here we can write a Lorentz transformation from the vector dx^α in one spacetime coordinate to another as

$$\mathrm{d}x'^\alpha = \Lambda^\alpha_\beta \, \mathrm{d}x^\beta \tag{1.4}$$

with Λ^α_β being constants and following the restriction

$$\Lambda^\alpha_\gamma \, \Lambda^\beta_\delta \, \eta_{\alpha\beta} = \eta_{\gamma\delta} \, . \tag{1.5}$$

Special relativity describes the physics of inertial frames and explains relativistic effects such as time dilation, length contraction and the relativity of simultaneity.

1.1.2 General Relativity

In the year 1915, Einstein proposed General Relativity (GR), which is a modified theory with inclusion of the acceleration of reference frames. In special relativity, spacetime is considered flat, while in General Relativity, gravity is the curvature of spacetime. This curved spacetime is described by a Lorentzian (or pseudo-Riemannian) metric, with a symmetric tensor $g_{\mu\nu}$ in the signature of $(- \; + \; + \; +)$.

$$\mathrm{d}s^2 = g_{\mu\nu} \, \mathrm{d}x^\mu \, \mathrm{d}x^\nu \, . \tag{1.6}$$

It is defined by

$$g_{\mu\nu} \equiv \eta_{\mu\nu} \, \frac{\partial \xi^\alpha}{\partial x^\mu} \, \frac{\partial \xi^\beta}{\partial x^\nu} \, , \tag{1.7}$$

where $\xi^\alpha(x)$ is the locally inertial coordinate system. $g_{\mu\nu}$ is also the gravitational potential so it determines the gravitational force. The inverse of $g_{\mu\nu}$ is defined as

$$g^{\mu\nu} = \eta^{\alpha\beta} \, \frac{\partial x^\mu}{\partial \xi^\alpha} \, \frac{\partial x^\nu}{\partial \xi^\beta} \, , \tag{1.8}$$

and the product of it and $g_{\mu\nu}$ yields the Kronecker delta

$$g^{\mu\nu} g_{\nu\sigma} = \delta^\mu_\sigma \, . \tag{1.9}$$

The affine connection (or the Christoffel symbol) $\Gamma^{\lambda}_{\mu\nu}$ is a differential operator defined as

$$\Gamma^{\lambda}_{\mu\nu} \equiv \frac{\partial x^{\lambda}}{\partial \xi^{\alpha}} \frac{\partial^2 \xi^{\alpha}}{\partial x^{\mu}\, \partial x^{\nu}} \,. \tag{1.10}$$

It is determined by the derivatives of the metric tensor $g_{\mu\nu}$ as

$$\Gamma^{\lambda}_{\mu\nu} = \frac{1}{2}\, g^{\lambda\sigma} \left(\frac{\partial g_{\nu\sigma}}{\partial x_{\mu}} + \frac{\partial g_{\mu\sigma}}{\partial x_{\nu}} - \frac{\partial_{\sigma} g_{\mu\nu}}{\partial x_{\sigma}} \right). \tag{1.11}$$

In a curved spacetime, differentiation of a tensor does not generally yield another tensor, so we need to use covariant differentiation instead

$$V^{\mu}_{;\lambda} \equiv \frac{\partial V^{\mu}}{\partial x^{\lambda}} + \Gamma^{\mu}_{\lambda\kappa}\, V^{\kappa} \,, \tag{1.12}$$

Parallel transport is a process of moving a vector along a smooth curve so that it stays parallel with respect to the affine connection in Eq. (1.11). This requires its covariant derivative along the curve vanishes, or Eq. (1.12) equals zero. The failure of parallel transport to preserve the vector's direction around an infinitesimal closed loop in curved space reveals the Riemann-Christoffel curvature tensor

$$R^{\lambda}_{\mu\nu\kappa} \equiv \frac{\partial \Gamma^{\lambda}_{\mu\nu}}{\partial x^{\kappa}} - \frac{\partial \Gamma^{\lambda}_{\mu\kappa}}{\partial x^{\nu}} + \Gamma^{\eta}_{\mu\nu}\, \Gamma^{\lambda}_{\kappa\eta} - \Gamma^{\eta}_{\mu\kappa}\, \Gamma^{\lambda}_{\nu\eta} \,. \tag{1.13}$$

The Ricci tensor is formed by using the metric tensor to form linear combinations of $R^{\lambda}_{\mu\nu\kappa}$

$$R_{\mu\kappa} \equiv R^{\lambda}_{\mu\lambda\kappa} = R_{\mu\nu\kappa\delta}\, g^{\nu\delta} \,, \tag{1.14}$$

and the Ricci scalar is formed by

$$R = g^{\mu\kappa}\, R_{\mu\kappa} \,. \tag{1.15}$$

By permuting ν, κ and η cyclically to $R_{\lambda\mu\nu\kappa;\eta}$, we obtain the Bianchi identities

$$R_{\lambda\mu\nu\kappa;\eta} + R_{\lambda\mu\eta\nu;\kappa} + R_{\lambda\mu\kappa\eta;\nu} = 0 \tag{1.16}$$

Contracting λ with ν gives

$$R_{\mu\kappa;\eta} - R_{\mu\eta;\kappa} + R^{\nu}_{\mu\kappa\eta;\nu} = 0 \tag{1.17}$$

Contracting again gives

$$(R_{\mu\nu} - \frac{1}{2} g_{\mu\nu} R)_{;\mu} = 0 \,. \tag{1.18}$$

Therefore we can construct the Einstein tensor $G_{\mu\nu}$ as

$$G_{\mu\nu} = R_{\mu\nu} - \frac{1}{2} g_{\mu\nu} R \,, \tag{1.19}$$

and its covariant derivative is zero

$$G^{\mu}_{\nu;\mu} = 0 \,. \tag{1.20}$$

1.1.3 Einstein Field Equations

Einstein proposed that the Einstein tensor $G_{\mu\nu}$ is proportional to the stress energy tensor $T_{\mu\nu}$ as

$$G_{\mu\nu} = \kappa T_{\mu\nu} \,. \tag{1.21}$$

To find the coefficient κ, we need to consider the Newtonian limit. In a weak static field produced by a non-relativistic mass density ρ, the time-time component of the metric tensor can be approximated as [1] (assuming speed of light $c = 1$)

$$g_{00} \approx -(1 + 2\phi) \,, \tag{1.22}$$

where ϕ is the Newtonian potential $\phi = -G M/r$ at a distance r from the center of a spherical body of mass M, with G being the Newtonian gravitational constant. It is determined by Poisson's equation:

$$\nabla^2 \phi = 4\pi G \rho \,, \tag{1.23}$$

where ∇^2 here is the Laplacian operator, representing the second spatial derivative. The energy density T_{00} for non-relativistic matter is its mass density ρ, revealing

$$\nabla^2 g_{00} = -8\pi G T_{00} \,. \tag{1.24}$$

If we add the speed of light back into this equation, it becomes $\nabla^2 g_{00} = -\frac{8\pi G}{c^4} T_{00}$. In the limit of weak static field produced by non-relativistic matter,

$$G_{00} \approx \nabla^2 g_{00} \,, \tag{1.25}$$

therefore the coefficient should be

$$G_{\mu\nu} = -\frac{8\pi G}{c^4} T_{\mu\nu} \,. \tag{1.26}$$

The stress energy tensor $T_{\mu\nu}$ is symmetric and conserved (in the sense of covariant differentiation), so is $G_{\mu\nu}$. Besides Eq. (1.19), the metric $g_{\mu\nu}$ is also conserved (its covariant derivative is zero), so we can also include a new term equal to $g_{\mu\nu}$ times a constant to the field equation:

$$R_{\mu\nu} - \frac{1}{2} g_{\mu\nu} R - \Lambda g_{\mu\nu} = -\frac{8\pi G}{c^4} T_{\mu\nu} \,. \tag{1.27}$$

This new term is introduced by Einstein in 1917 for cosmological reasons, so Λ is called the `cosmological constant`. This term satisfies all the conditions (symmetric, conserved tensor) but it doesn't satisfy Eq. (1.25), so Λ must be very small to ensure compatibility with Newton's theory of gravitation.

1.2 Gravitational Waves

1.2.1 Weak Field Approximation

Under the weak field limit, the spacetime metric $g_{\mu\nu}$ can be divided into two parts (following the notation and derivations in [2]):

$$g_{\mu\nu} = \eta_{\mu\nu} + h_{\mu\nu}, \text{ where } \left|h_{\mu\nu}\right| \ll 1 \,. \tag{1.28}$$

where the zeroth order term is the Minkowski metric and the first order term $h_{\mu\nu}$ is the weak field perturbation. To the first order in h, the Riemann curvature tensor is approximately

$$R_{\mu\nu\rho\sigma} \approx -\frac{1}{2}(\partial^2_{\mu\sigma} h_{\nu\rho} + \partial^2_{\nu\rho} h_{\mu\sigma} - \partial^2_{\mu\rho} h_{\nu\sigma} - \partial^2_{\nu\sigma} h_{\mu\rho}) \,, \tag{1.29}$$

with the notation $\partial^2_{\mu\nu} = \frac{\partial^2}{\partial x^\mu \partial x^\nu}$. To the first order of h, the Ricci tensor is then

$$R_{\mu\nu} \approx \frac{1}{2}(\Box h_{\mu\nu} - \partial^2_{\lambda\mu} h^\lambda_\nu - \partial^2_{\lambda\nu} h^\lambda_\mu + \partial^2_{\mu\nu} h^\lambda_\lambda)\,. \tag{1.30}$$

where the d'Alembertian operator $\Box = \partial^\mu \partial_\mu = \eta^{\mu\nu}\partial^2_{\mu\nu}$. As we are restricted to the first order of h, we raise and lower indices using the Minkowski metric $\eta^{\mu\nu}$ instead of $g^{\mu\nu}$

$$h^\lambda_\nu \equiv \eta^{\lambda\rho}\, h_{\rho\nu}\,. \tag{1.31}$$

We can define a trace-reversed metric $\bar{h}_{\mu\nu}$ as

$$\bar{h}_{\mu\nu} = h_{\mu\nu} - \frac{1}{2}\,\eta_{\mu\nu}\, h\,, \tag{1.32}$$

where the trace of h is $h = \eta^{\mu\nu}\, h_{\mu\nu}$, so $\bar{h} \equiv \eta^{\mu\nu}\,\bar{h}_{\mu\nu} = h - 2h = -h$. Eq. (1.32) can be inverted to give

$$h_{\mu\nu} = \bar{h}_{\mu\nu} - \frac{1}{2}\,\eta_{\mu\nu}\,\bar{h}\,. \tag{1.33}$$

The Einstein field equations then become

$$\Box\bar{h}_{\mu\nu} + \eta_{\mu\nu}\,\partial^2_{\rho\sigma}\,\bar{h}^{\rho\sigma} - \partial^\rho\partial_\nu\bar{h}_{\mu\rho} - \partial^\rho\partial_\mu\bar{h}_{\nu\rho} - = -\frac{16\pi\,G}{c^4}\,T_{\mu\nu}\,. \tag{1.34}$$

To look at the effect of gauge freedom, we show how $\bar{h}_{\mu\nu}$ transforms under infinitesimal coordinate transformation

$$x^\mu \to x'^\mu = x^\mu + \xi^\mu\,, \tag{1.35}$$

where $\partial\xi^\mu/\partial x^\nu$ is at most of the same order of magnitude of $h_{\mu\nu}$. The new metric is then

$$\bar{h}'^{\mu\nu} = \bar{h}^{\mu\nu} - \partial_\nu\xi_\mu - \partial_\nu\xi_\mu + \eta_{\mu\nu}\,\eta^{\sigma\rho}\,\partial_\sigma\xi_\rho\,, \tag{1.36}$$

to the first order of ξ. Under this transformation, the Riemann curvature tensor $R_{\mu\nu\rho\sigma}$ does not change to the first order of h. So we can choose any gauge ξ_ρ with small derivatives. We choose a gauge that ensures $\bar{h}'$ is traceless:

$$\partial^\nu\bar{h}'_{\mu\nu} = 0\,, \tag{1.37}$$

which is known as the *Lorenz gauge* or the *harmonic gauge*. We are fine to make this choice,

as this coordinate transformation gives

$$\partial'^{\nu}\bar{h}'_{\mu\nu} = \partial^{\nu}\bar{h}_{\mu\nu} - \Box\xi_{\mu}\,. \tag{1.38}$$

We can always find a transformation satisfying $\Box\xi_{\mu} = \partial^{\nu}\bar{h}_{\mu\nu}$. Under these circumstances, the Einstein field equations then become

$$\Box\bar{h}_{\mu\nu} = -\frac{16\pi G}{c^4}\,T_{\mu\nu}\,. \tag{1.39}$$

As we are far away from the source, we can set the stress-energy tensor to be zero ($T_{\mu\nu} = 0$). Under this condition, we can choose $\bar{h}_{\mu\nu}$ to be traceless and transverse, equivalently:

$$\bar{h} = 0\,, h^{0i} = 0\,, h^{i}_{i} = 0\,, \partial^{j}h_{ij} = 0\,. \tag{1.40}$$

for i going over all three spatial dimensions. This is known as the *transverse-traceless gauge* or TT gauge. We denote its metric as h^{TT}_{ij}.

The Einstein field equations in Eq. (1.34) is then reduced to

$$\Box\bar{h}_{\mu\nu} = -\frac{16\pi G}{c^4}\,T_{\mu\nu} = 0\,. \tag{1.41}$$

This is a homogeneous equation with a wave function solution.

1.2.2 Plane Wave Solutions

The solution to the plane wave equations in Eq. (1.41) can be written as

$$h^{\mathrm{TT}}_{ij}(x) = A\,e_{ij}(\mathbf{k})\,\mathrm{e}^{ikx}\,, \tag{1.42}$$

where $k^{\mu} = (\omega/c, \mathbf{k})$ and $\omega/c = |\mathbf{k}|$. A is the amplitude of the wave, $e_{ij}(\mathbf{k})$ is the polarization tensor and $\mathbf{k}$ is the wave vector. From Eq. (1.40), we get that the non-zero terms of h^{TT}_{ij} are in the plane transverse to the direction of wave propagation $\hat{\mathbf{n}} = \mathbf{k}/|\mathbf{k}|$

$$\partial^{i}h^{\mathrm{TT}}_{ij} = 0 = \mathbf{k}^{i}h^{\mathrm{TT}}_{ij}\,, \mathbf{k}^{i}\mathrm{e}^{\mathrm{TT}}_{ij} = 0\,. \tag{1.43}$$

We can choose $\hat{\mathbf{n}}$ along the z axis and h_{ij}^{TT} is symmetric and traceless, then for i, j going over 1,2:

$$h_{ij}^{\mathrm{TT}}(t,z) = \begin{pmatrix} h_+ & h_\times \\ h_\times & -h_+ \end{pmatrix}_{ij} \cos[\omega(t - z/c)]\,, \tag{1.44}$$

or

$$A\, \mathrm{e}_{ij}^{\mathrm{TT}}(\mathbf{k}) = \begin{pmatrix} h_+ & h_\times \\ h_\times & -h_+ \end{pmatrix}, \tag{1.45}$$

so that the polarization tensor can be split into

$$\mathrm{e}_{ij}^{+} = \begin{pmatrix} 1 & 0 \\ 0 & -1 \end{pmatrix}, \;\; \mathrm{e}_{ij}^{\times} = \begin{pmatrix} 0 & 1 \\ 1 & 0 \end{pmatrix}, \tag{1.46}$$

and

$$h_{ij}^{\mathrm{TT}} = \left(h_+\, \mathrm{e}_{ij}^{+} + h_\times\, \mathrm{e}_{ij}^{\times}\right). \tag{1.47}$$

1.2.3 Interaction of Gravitational Waves with Test Masses

The interaction of gravitational waves (GW) and detectors, idealized as sets of test masses, will change the proper distance between the test masses. If we assume two test masses are Δx apart in the x direction, then with a gravitational wave traveling perpendicular to both (in z direction), the proper distance becomes

$$\Delta s = \sqrt{\Delta s^2} = \Delta x \sqrt{1 + h_+ \cos(\omega t)} \approx \Delta x \left(1 + \frac{1}{2}\, h_+ \cos(\omega t)\right). \tag{1.48}$$

Similarly, if the two test masses are separated by Δy apart in the y direction, then

$$\Delta s = \sqrt{\Delta s^2} \approx \Delta y \left(1 - \frac{1}{2}\, h_+ \cos(\omega\, t)\right). \tag{1.49}$$

So with gravitational waves' effect, the proper distance between the two separated masses will change periodically in time, i.e., the proper distance will increase for events separated in the x direction, while for events separated in the y direction, the proper distance will decrease, and vice versa. More generally, if the two test masses are separated by the distance vector $\vec{L}$, the

proper distance between them will be

$$s^2 = L^2 + h_{ij}(t)\, L_i\, L_j\,. \tag{1.50}$$

To the first order of h, we have

$$s \simeq L + h_{ij}\,(L_i\, L_j/2L)\,, \tag{1.51}$$

implying that the change in proper distance is proportional to the initial spatial separation L between the two masses.

Based on the gravitational wave effect we introduced above, we know that for a set of test masses aligned on a circular ring, a transverse gravitational wave will make the ring of test masses become an ellipse along an axis, and return to a round circle, then become an ellipse along the other axis, with the change in time. The process is shown in Figure 1.1.

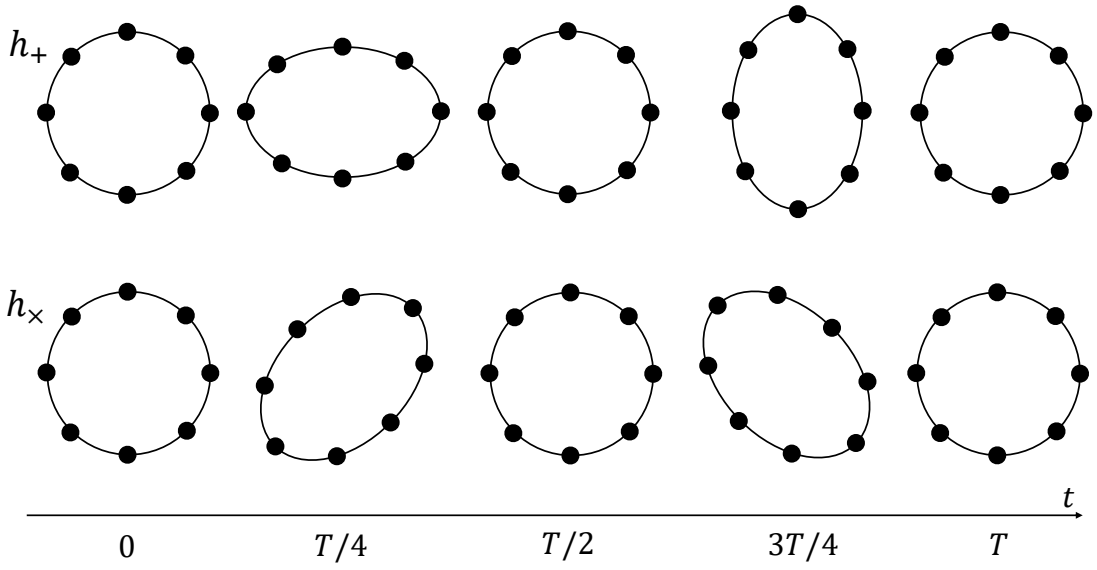

Figure 1.1: The deformation of a set of test masses on a circular ring as a function of time due to the effect of h_+ and $h_\times$ polarization.

1.2.4 Gravitational Wave Generation

The general solution to Eq. (1.39) under the assumption that gravitational wave sources are far away from the observer with distance r, shows that gravitational waves are generated by a quadrupole moment with change in time t:

$$h_{ij}^{\mathrm{TT}} = \frac{2G}{c^4\, r}\, \ddot{I}_{ij}\,(t - r/c)\,, \tag{1.52}$$

where $\ddot{I}_{ij}$ is the second time derivative of the spatial part of the quadrupole tensor I_{ij}, with the dot denoting the derivative with respect to the *coordinate time* t [2]. I_{ij} is related to the mass density ρ by

$$I_{ij} = \int \mathrm{d}\vec{x}^3\, \rho(t, \vec{x}) \left(x_i\, x_j - \frac{1}{3}\, \delta_{ij}\, |\vec{x}|^2 \right). \tag{1.53}$$

Based on the values of Newton's constant G and speed of light c, the pre-factor $2G/c^4\, r$ is of order $10^{-44}\,\mathrm{N}^{-1}$, meaning that to generate gravitational wave events measurable by ground-based detectors whose sensitivity is around $h \sim 10^{-23}$ for time-strains, the events are required to be energetic. For a binary system of objects with mass M, rotating around each other with radius r_0 at frequency f, of a distance r away from the observer, the amplitude of the observed gravitational wave is then

$$|h| = \frac{8G\, M}{c^4\, r}\, (2\pi\, f\, r_0)^2 = \frac{32\, \pi^2\, G}{c^4\, r}\, M\, r_0^2\, f^2\,. \tag{1.54}$$

The typical amplitude of h is usually around 10^{-23}, which is very small.

1.3 LIGO Detectors

When a gravitational wave passes through, it distorts spacetime—stretching it in one direction while compressing it in the perpendicular direction. To detect such waves originating from distant sources, scientists typically use Michelson interferometers. In these devices, a laser beam is split into two perpendicular arms, each ending with a mirror. The light bounces back and forth between the mirrors in each arm, then recombines at the beam splitter, where it interferes. The resulting interference pattern is measured by a photo-detector, revealing subtle changes caused by the passing wave. A sketch of the path of light in a Michelson interferometer is shown in Figure 1.2.

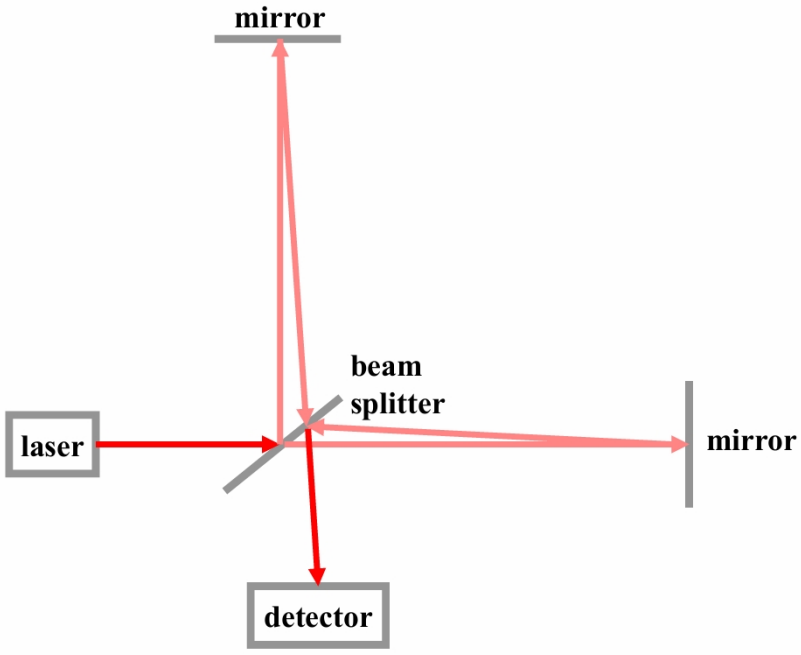

Figure 1.2: A sketch of path of light in Michelson interferometer.

When there is no passing gravitational wave, the two beams interfere destructively, resulting in zero intensity at the photo-detector. When there is a gravitational wave passing through the interferometer, the distance stretches in one arm and compresses in the other arm. Therefore the travel time of light becomes longer in one arm and shorter in the other arm, leading to constructive interference when the beams recombine. As a result, the photo-detector records a higher intensity. If the gravitational wave oscillates, the detected intensity fluctuates accordingly.

Detecting gravitational wave signals simultaneously in multiple detectors significantly increases the confidence that the signal originates from an astrophysical event rather than from instrumental noise. This coincidence across geographically separated detectors helps rule out spurious artifacts and strengthens the case for a genuine gravitational wave detection.

1.3.1 Advanced LIGO Detector Layout

The first generation of LIGO (Laser Interferometer Gravitational-Wave Observatory) detectors includes three interferometers in the United States: two located at Hanford, Washington: H1 and H2 are four kilometers long and two kilometers long; one at Livingston, Louisiana: L1 is

four kilometers long. The initial LIGO detectors operated through 2010, no gravitational wave signal was detected [3].

The second generation of LIGO detectors "Advanced LIGO" (or "aLIGO") [4] are instruments designed and built for the two LIGO observatories in Hanford (H1) and Livingston (L1). They were installed between 2010 and 2014.

The Advanced LIGO detectors are Michelson interferometers of two perpendicular arms with one Fabry-Pérot resonant cavity in each arm to develop phase change throughout the length of an arm. The layout of one advanced LIGO detector is shown in Figure 1.3. As shown in Fig-

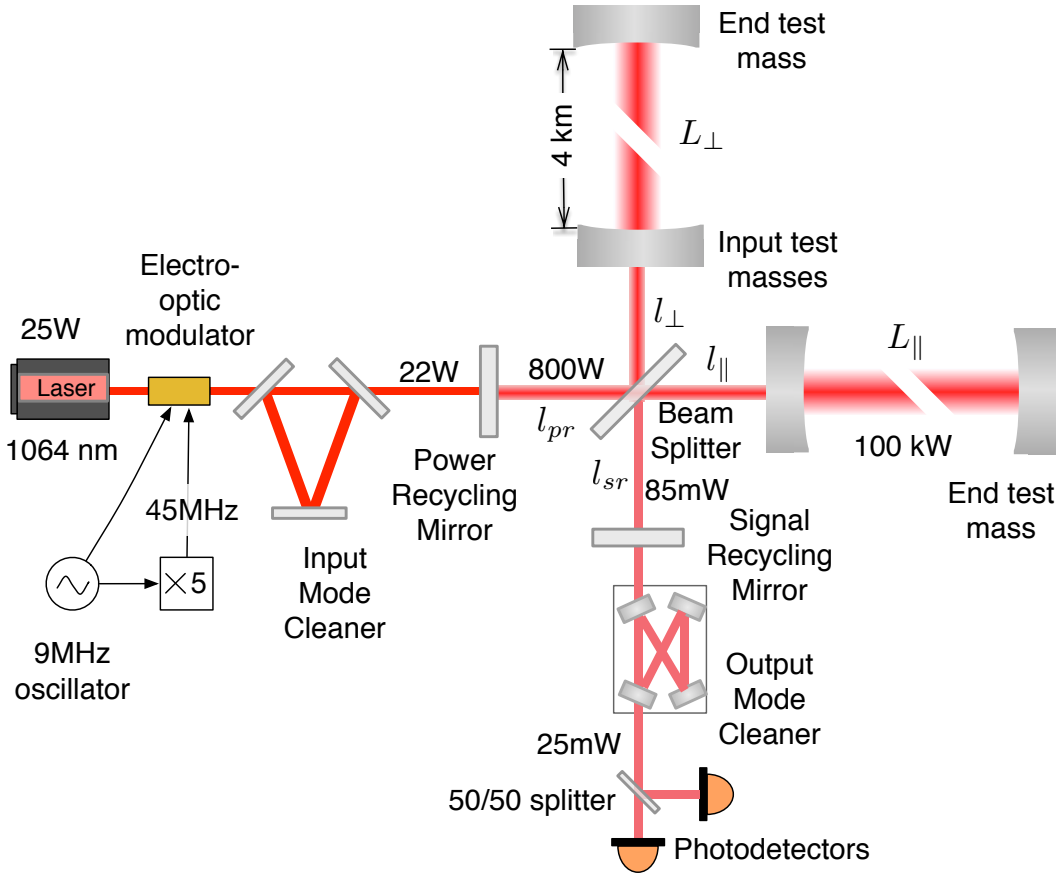

Figure 1.3: Advanced LIGO detector layout. The annotated powers are from O1. This figure is from [3].

ure 1.3, the Michelson interferometer consists of a laser source of wavelength $\lambda = 1064\,\text{nm}$, a

beam splitter (BS) and two (input and end) test masses (mirrors) in each of the two perpendicular arms of four-kilometer length $L_0 = 4\,\mathrm{km}$. As the magnitude of the strain sensitivity can be approximated as $h \sim \frac{\Delta L}{L}$, with ΔL being the variation between the travel lengths L in the two arms, L must be large enough for us to detect GWs whose strain is very small. With the setup of test masses and the inclusion of Fabry-Pérot cavities, L is much extended compared to the original length of the arm L_0. The input mode cleaner (IMC) consists of a triangular Fabry-Pérot cavity and the output mode cleaner (OMC) in the antisymmetric port filters the spatial and frequency modes of the light. There are two more resonant cavities which further increase the travel length: the power recycling mirror (PRM) forms a power recycling cavity in order to increase the power of the laser incident on the Fabry-Pérot cavities; the signal recycling mirror (SRM) in the antisymmetric port similarly forms a signal recycling cavity and broadens the frequency response.

1.3.2 Advanced LIGO Detector Noise

As discussed in the previous subsection, the strain sensitivity of 10^{-23} is required for detection, so the sources of noise or noise-coupling need to be identified and minimized in order to improve the sensitivity of a detector. The Advanced LIGO detectors are sensitive in the broadband frequency from 20 Hz to 5000 Hz. The amplitude spectral densities of all known sources of noise ("noise budget") with respect to frequency are shown in Figure 1.4. For full details about projecting noises from auxiliary channels, see [5]. Here we list some of the important sources of noise.

Quantum noise

The quantum noise is due to the quantum mechanical nature of the laser light in the interferometer. It produces a fundamental floor of the detector sensitivity. It has two types: shot noise and quantum radiation pressure noise. Shot noise is related to the statistical fluctuations of the arrival time of photons at the photo-detector, leading to the fluctuations of the number of photons. The strain of shot noise can be written as [3]

$$L(f) = \frac{\lambda}{4\pi G_{\mathrm{arm}}} \sqrt{\frac{2h\nu G_{\mathrm{src}}}{G_{\mathrm{prc}} P_{\mathrm{in}} \eta}} \frac{1}{|K_-(f)|}\,, \tag{1.55}$$

where h denotes the strain signal, $P_{\rm in}$ is the input power of the detector. The laser carrier frequency $\nu = 2.82 \times 10^{14}$ Hz, the arm cavity build–up $G_{\rm arm} = 270$, signal recycling cavity gain $G_{\rm src} = 9.2$, power recycling gain $G_{\rm prc} = 38$, the fraction of the transmitted power $\eta = 0.75$ [3]. The transfer function K_- of the response of the Advanced LIGO detectors at frequency f due to common and differential coupled cavity poles (f_+, f_-) is

$$K_- = \frac{f_-}{if + f_-} \,. \tag{1.56}$$

where the common coupled cavity pole $f_+ = 0.6\,$Hz and the differential coupled cavity pole $f_- = 335 - -390\,$Hz. The transfer function can be complex, in Eq. (1.55) its magnitude $|K_-(f)|$ is used. Shot noise dominates at high frequency and decreases when laser power increases.

The other type of quantum noise is quantum radiation pressure noise, which is related to the fluctuations of the number of photons hitting the mirrors (test masses) in the arms, exerting a radiation force and causing displacement of the test masses. It can be written as [3]

$$L(f) = \frac{2}{c\,M\,\pi^2\,f^2}\,\sqrt{h\,\nu\,G_-\,P_{\rm arm}}\,|K_-(f)|\,, \tag{1.57}$$

where $M = 40\,$kg is the mass of the test mass, $P_{\rm arm} \approx 100\,$kW is the power circulating in the arm cavities, $G_- = 31.4$ is the differential coupled cavity build-up [3]. This noise is more important at low frequencies and increases when laser power increases, as opposed to shot noise. So the sum of them, which is the total quantum noise, can be minimized to "standard quantum limit" as a function of frequency.

Thermal noise

Thermal noise is also a type of displacement noise and has many sources: thermal motion in the suspension fibers of the test masses, optical coatings and substrates. Suspension thermal noise causes test masses to move due to thermal vibrations of the suspension fibers. Coating Brownian noise is caused by thermal fluctuations of the optical coating. This noise is limited by using the titania-doped tantala/silica coatings and optimizing the thickness of the coatings. Thermal noise due to substrates is limited by choosing the fused silica substrate material.

Seismic noise

Seismic noise comes from motions of the ground around the detectors such as earthquakes, building vibration and anthropogenic activities. The advanced LIGO detectors use the test mass quadruple suspension system which suspends each test mass by quadruple pendula to reduce coupling of ground motion. The pendula are suspended from seismic isolation platforms, the platforms are supported by hydraulically actuated pre-isolation structures. As each of the pendula forms a passive-filter stage and reduces this noise by $(f_0/f)^2$, together they result in suppression to $(f_0/f)^8$, where f_0 is the pendulum resonant frequency, which is about 1 Hz [3, 5].

Other noise sources

There are also other types of noise, such as Newtonian noise and gas residual noise [3, 5]. They are subdominant compared to the sources I mention above. Newtonian noise primarily comes from Rayleigh seismic waves and atmospheric pressure fluctuations. It directly perturbs test masses by gravitational coupling and is expected to limit the designed sensitivity of Advanced LIGO in the 10—20 Hz frequency range. Newtonian noise has not been detected in Advanced LIGO, and is predicted to be below LIGO's sensitivity levels.

Gas residual noise is the displacement and sensing noise caused by residual gas. As the Advanced LIGO optics are located inside vacuum chambers, residual gas disturbs test masses through molecular collisions and alters the laser beam's phase via photon scattering.

1.3.3 Advanced LIGO Observing Runs

The LIGO Scientific Collaboration (LSC) started the first observing run (O1) on September 12, 2015 through January 19, 2016 [3] and detected the first gravitational wave event GW150914 [6, 7], which is a binary black hole merger, with the two black holes of initial masses being 36 and 29 solar masses in the source frame. LSC also detected two other binary black hole mergers: GW151012 [8] and GW151226 [9].

The second observation run (O2) started on November 30, 2016 through August 25, 2017. LSC detected 7 binary black hole mergers: GW170104 [10], GW170608 [11], GW170814 [12], GW170729, GW170809, GW170818, GW170823 [13] and one binary neutron star merger: GW170817 [14]. The first version of the Gravitational Wave Transient Catalog (GWTC-1) [13] covered both the O1 and O2 observing runs and reported all 11 candidates above.

The third observation run (O3) started on April 1, 2019 to September 30, 2019 (O3a) and from November 1, 2019 to March 27, 2020 (O3b). Besides Advanced LIGO, Advanced Virgo and KAGRA also contribute to O3. GWTC-2 [15] and its updated version, GWTC-2.1 [16] included data from O3a. In GWTC-2, 39 new events were added, and in GWTC-2.1, the total number of candidates was raised to 55. GWTC-3 [17] included data from O3b and reported 35 new significant candidates including the first two observed neutron star–black hole mergers. Together we have 90 GW transients in the catalog.

These observations of Advanced LIGO, Advanced Virgo and KAGRA (LVK) through O3 have inspired a series of researches including tests of General Relativity [18], measurements of the Hubble constant H_0 [19], tests of the neutron star equation of state [20], searches for other sources such as Continuous Waves (CW) [21], Gamma-Ray Bursts (GRB) [22, 23].

The fourth observation run (O4) is currently on-going. The first part of it from May 2023 to January 2024 (O4a) is now released, and the catalog GWTC-4.0 [24] contains about 200 compact binary coalescence candidates that are consistent with signals from binary black holes and neutron star–black hole binaries. Updated studies are released following the topics in O3, such as upper limits on the isotropic gravitational-wave background [25], all-sky search for long-duration gravitational-wave transients [26], searches for continuous gravitational waves from known pulsars [27].

1.4 Gravitational Wave Types and Sources

1.4.1 Compact Binary Coalescences

Compact binary systems emit gravitational waves when the two objects rotate around each other. Emitting gravitational waves causes loss of energy, leading to the decrease of orbit radius and increase of rotating frequency until the two objects merge or coalesce. Compact Binary Coalescences (CBC) are binary systems consisting of two black holes, often referred to as binary black holes (BBH), or two neutron stars, similarly binary neutron stars (BNS), or one black hole and one neutron star (BHNS).

The frequency of the gravitational waves emitted by this coalescing binary system will reach its maximum at the time of coalescence, as expressed in the following equation to the lowest

order:

$$f^{\mathrm{GW}}(t) = \frac{1}{8\pi}\Big(\frac{G\mathcal{M}}{c^4}\Big)^{-5/8}\Big(\frac{5}{(t-t_c)}\Big)^{3/8}, \tag{1.58}$$

where t_c is the time of coalescence, $\mathcal{M}$ is the chirp mass:

$$\mathcal{M} \equiv \frac{(m_1 m_2)^{3/5}}{(m_1+m_2)^{1/5}}\,. \tag{1.59}$$

The above merging process produces a "chirp" signal, which produces a sound that is similar to the chirp of a bird when translated to sound waves in the audio band.

1.4.2 Continuous Waves

An individual rapidly rotating neutron star can produce continuous gravitational waves if it is not axisymmetric but elliptical. If the ellipticity of the neutron star is ϵ, then the amplitude of the gravitational wave strain it emitted is

$$h = \frac{16\pi^2 G}{c^4}\,\frac{\epsilon f^2 I_{zz}}{r}\,, \tag{1.60}$$

where I is the moment of inertia, f is the rotating frequency of the star, and ϵ is the ellipticity:

$$\epsilon = (I_{xx} - I_{yy})/I_{zz}\,. \tag{1.61}$$

Rapidly rotating neutron stars emit gravitational waves characterized by nearly constant oscillatory patterns—typically resembling sine or cosine functions—that persist over extended periods. These signals generally do not vary significantly over the observational timescale, which, in LIGO's case, is on the order of a year. Consequently, this class of gravitational wave signals is referred to as "continuous waves". Currently we don't have detection on CW signals in O4a data, see [27].

1.4.3 Burst Events

Supernovae explosions or gamma ray bursts may emit gravitational waves in short durations of the order of seconds. These short gravitational wave events are called "Bursts". These gravitational wave signals are difficult to model. Other unknown or unexpected sources can also emit bursts. For O4a data, [28] presents searches on short-duration gravitational-wave

transients and finds no statistically significant evidence for gravitational-wave transients other than identified BBHs. This paper also evaluates various core-collapse supernova models and finds that gravitational waves can be detected from stellar core-collapse throughout the Milky Way.

1.4.4 Stochastic Background

The stochastic gravitational wave background (SGWB) is the combination of many weak gravitational waves from all across the sky [29, 30]. These gravitational wave events are too faint to be resolved by the detector. There are two types of possible stochastic sources, one has a cosmological origin, the other is astrophysical. The astrophysical stochastic sources may be unresolved compact binary coalescences [31–38], supernovae [30, 39–45], rapid rotating neutron stars [35,46–50] or others. The cosmological sources may date back to the early Universe during the inflationary epoch, or they can come from primordial black holes, cosmic strings [51–61] or the phase transitions [62–68].

The stochastic background is usually described as the gravitational wave energy density per logarithm of frequency, normalized by the critical energy density $\rho_c = 3H_0^2 c^2/(8\pi G)$, where H_0 is the Hubble constant:

$$\Omega_{GW} = \frac{1}{\rho_c}\frac{d\rho_{GW}}{d\ln f} = \frac{f}{\rho_c}\frac{d\rho_{GW}}{df}\,. \tag{1.62}$$

Here the quantity Ω_{GW} is dimensionless. We will discuss this quantity more in detail in the following chapters.

Both the cosmological and astrophysical components of the stochastic gravitational wave background are expected to exhibit anisotropies. These anisotropies stem from three key mechanisms: 1) the uneven distribution and emission of sources; 2) propagation through cosmic structures, which distorts signals via lensing, time-delay and integrated time delay, even if the emission was isotropic [69–71]; 3) kinematic effects from Earth's motion relative to the source frame [72, 73]. Therefore, the energy density of the SGWB may exhibit correlations with anisotropies in electromagnetic (EM) tracers of large-scale structure, such as galaxy number counts, weak lensing signals, cosmic microwave background (CMB), cosmic infrared background (CIB), etc. Measuring these correlations offers new tools to probe matter distribution and its evolution in the Universe. In this dissertation, I aimed at searching for the correlation between the stochastic background and galaxy counts (GC).

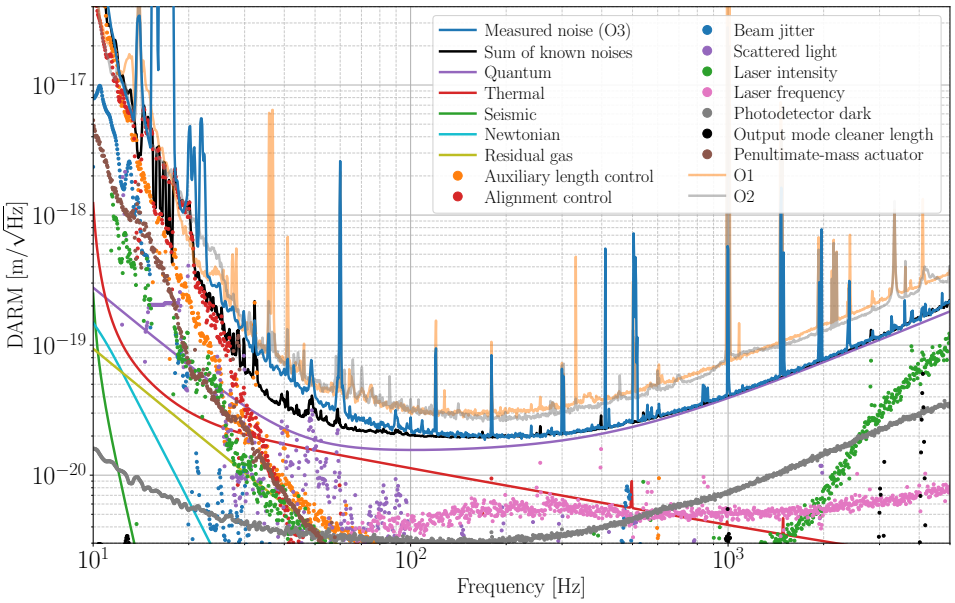

(a) LHO

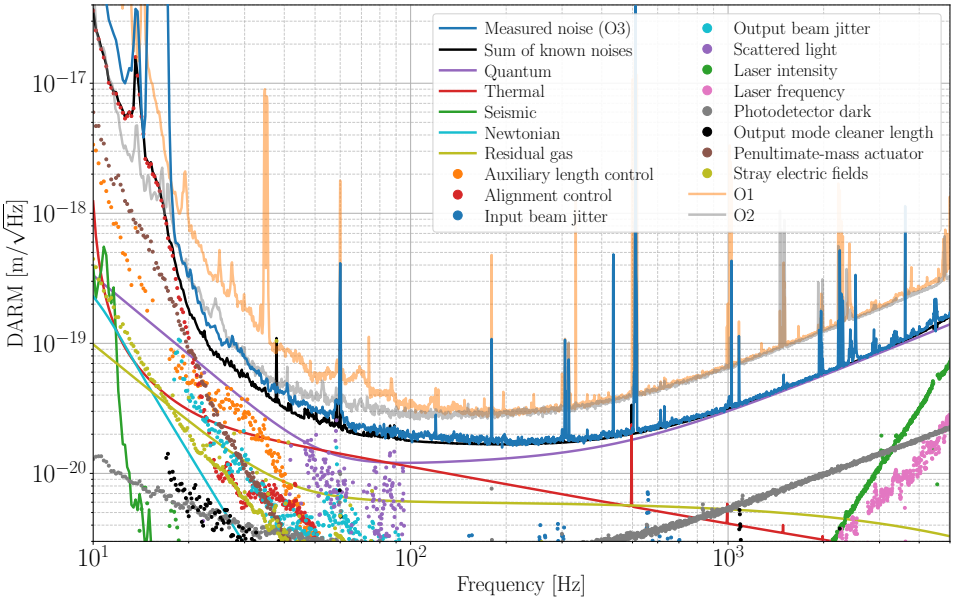

(b) LLO

Figure 1.4: The amplitude spectral density of all known noises in (a) LIGO Hanford Observatory (LHO) and (b) LIGO Livingston Observatory (LLO). Figure cited from [5].

Chapter 2

Cross-Correlation Coherence of Stochastic Gravitational Wave Background and Galaxy Number Counts

2.1 Introduction

By the summer of 2017, LIGO finished its second observation run and detected gravitational waves from 7 binary black hole mergers [12, 13, 74–78] and one binary neutron star merger [79] during this observation run. These detections led to studies on multi-messenger astronomy with gravitational waves, and raised a broad range of topics such as tests of General Relativity (GR) [80, 81], constraints on the equation of state of neutron stars [79], estimates of the rates of BBH and BNS coalescences [74, 82], studies on the progenitor of the BNS merger [79], measurement of the Hubble constant H_0 [83], kilonova associated with the BNS merger [84], and so on.

These observations also imply a relatively strong stochastic gravitational-wave background which is formed by the superposition of the signals of the unresolved BBH and BNS merger across the Universe [37, 38, 85]. As the Advanced Laser Interferometer Gravitational-Wave Observatory (aLIGO) [86] and Advanced Virgo (aVirgo) [87] detectors improve their strain

sensitivities, one of their primary targets will be to detect the SGWB [85, 88]. The prospects for improvements on the strain sensitivity [89] combined with the Bayesian search technique which was newly proposed at that time [90] brought the possibility of detecting SGWB with advanced detectors closer to reality. Due to this discovery potential, much literature emerged, studying the possible anisotropy of the astrophysical SGWB due to binary mergers [69–71, 91–103], and the cosmological SGWB models due to phase transitions [104] and cosmic strings [61]. There are also investigations on the possibility of correlating the anisotropy of SGWB with the anisotropy observed in electromagnetic tracers of the large scale structure, such as galaxy counts and weak lensing [70, 71, 96, 98, 100, 105–109], or the cosmic microwave background [104]. The first theoretical predictions of the angular power spectrum of the SGWB and its cross-correlation with the galaxy number counts or the weak lensing convergence have been made, including the dependence of the cross-correlation power spectrum on SGWB frequency and the galaxy redshift distribution [96].

Cross-correlating the SGWB anisotropy with anisotropy in EM tracers opens up several paths for investigation. First, the GW-EM correlation method is likely to be more sensitive when trying to detect the SGWB anisotropy than the traditional techniques that rely on GW data alone. Second, the GW-EM correlation can be incorporated in a parameter estimation framework to measure the cosmological and astrophysical parameters of the model of the SGWB anisotropy [70, 96, 98, 100, 110]: i.e., to constrain the formation and evolution of structure in the Universe. This step will be presented in Chapter 3 and Chapter 4. Third, cross-correlations with different EM tracers such as galaxy counts or CMB may enable distinguishing different SGWB contributions due to binary mergers or cosmological sources.

In this chapter, I present the first analysis of the GW-EM anisotropy correlations, using the data from the second observation run of aLIGO and the galaxy count distribution from the Sloan Digital Sky Survey (SDSS). I observe no significant correlations in the data and hence place upper limits on the correlation parameter. The rest of this chapter is organized as follows: in Section 2, I review the method for measuring the SGWB anisotropy and then apply it to different frequency bands of aLIGO data to compute SGWB sky maps at different angular resolutions. In Section 3, I review the SDSS catalog and compute the maps of the galaxy count distribution across the sky in several redshift slices. In Section 4, I compute the correlations between the SGWB and SDSS maps and establish the first upper limits on the correlation coefficients. In Section 5, I offer the concluding remarks and discuss the numerous ways of extending this study

in the future.

2.2 SGWB Anisotropy Upper Limit

Stochastic gravitational-wave background arises as a superposition of waves from many incoherent GW sources. Therefore, the SGWB does not have a deterministic waveform; instead, it is characterized by its energy density spectrum. In particular, the frequency and angular GW energy density spectrum $\Omega_{\rm GW}(f, \Theta)$ is defined as

$$\Omega_{\rm GW}(f, \Theta) = \frac{f}{\rho_{\rm c}} \frac{{\rm d}^3 \rho_{\rm GW}}{{\rm d}f \, {\rm d}^2\Theta} \,, \tag{2.1}$$

where $\rho_{\rm GW}$ is the GW energy density, f is frequency, Θ represents a direction on the sky, and $\rho_{\rm c}$ is the critical energy density needed to close the Universe. Past searches for the SGWB anisotropy have assumed that this spectrum can be factorized into frequency and sky-direction parts [88, 111, 112]:

$$\Omega_{\rm GW}(f, \Theta) = \frac{2\pi^2}{3H_0^2} \, f^3 \, H(f) \, \mathcal{P}(\Theta) \,, \tag{2.2}$$

where H_0 is the Hubble constant, $\mathcal{P}(\Theta)$ captures the angular dependence on the sky, and $H(f)$ describes the frequency dependence of the spectrum, typically assumed to take a power-law form

$$H(f) = \left(\frac{f}{f_{\rm ref}} \right)^{\alpha - 3} , \tag{2.3}$$

with some reference frequency $f_{\rm ref}$ and spectral index α. For the SGWB due to BBH and BNS mergers, $\alpha = 2/3$ [37, 38]. Other values of the spectral index are appropriate for other models. In this chapter $f_{\rm ref} = 100$ Hz is applied.

The spatial dependence can be decomposed into any set of basis functions on a sphere, here the spherical harmonics basis is used:

$$P(\Theta) = \sum_{lm} P_{lm} \, Y_{lm}(\Theta) \,. \tag{2.4}$$

The objective of the SGWB anisotropy upper limit analysis is therefore to estimate the parameters $P_{\ell m}$. I adopt the approach developed in [111] and used in past anisotropic SGWB searches [88, 112], which starts with the cross-correlation between the strain time series data of

GW detectors: LIGO Hanford (H1) and LIGO Livingston (L1) in this case,

$$C(f,t) = s_1^*(f,t)\, s_2(f,t)\,, \tag{2.5}$$

where t denotes a time segment, and s_1 and s_2 are the Fourier transforms of the strain time series of H1 and L1 in this time segment. Then one can define *the dirty map* X_ν as follows:

$$X_\nu = \sum_{f,t} \gamma_\nu^*(f,t)\, \frac{H(f)}{P_1(f,t)\, P_2(f,t)}\, C(f,t)\,, \tag{2.6}$$

where the sum is over all frequency bins f and all time segments t. The index ν runs over the spherical harmonic components [i.e. $\nu \equiv (l,m)$], $P_{1,2}(f,t)$ are strain power spectral densities for the two detectors, and $\gamma_\nu(f,t)$ is a geometric factor that is a function of the separation and relative orientation of the LIGO detectors H1 and L1 [111, 113].

The dirty map X_ν represents an estimate of the GW energy density sky distribution convolved with the response of the detectors' antenna patterns. The corresponding uncertainty is described by the covariance matrix, also known as the *Fisher matrix*:

$$\Gamma_{\mu\nu} = \sum_{f,t} \gamma_\mu^*(f,t)\, \frac{H^2(f)}{P_1(f,t)\, P_2(f,t)}\, \gamma_\nu(f,t)\,. \tag{2.7}$$

Estimators of the spherical harmonic coefficients $P_{\ell m}$, also known as the *the clean map*, are then given by [111]

$$\hat{P}_\mu = \sum_\nu (\Gamma_R^{-1})_{\mu\nu}\, X_\nu\,. \tag{2.8}$$

The covariance matrix corresponding to the $P_{\ell m}$'s is the inverse of the Fisher matrix, Γ_R^{-1}. In the weak-signal limit, the following approximations are satisfied:

$$\langle \hat{X}_{\ell m}\, \hat{X}^*_{\ell' m'} \rangle - \langle \hat{X}_{\ell m} \rangle \langle \hat{X}^*_{\ell' m'} \rangle \approx \Gamma_{\ell m, \ell' m'}\,, \tag{2.9}$$

$$\langle \hat{P}_{\ell m}\, \hat{P}^*_{\ell' m'} \rangle - \langle \hat{P}_{\ell m} \rangle \langle \hat{P}^*_{\ell' m'} \rangle \approx (\Gamma^{-1})_{\ell m, \ell' m'}\,. \tag{2.10}$$

In general, the Fisher matrix may be singular, reflecting the fact that the GW detector network may be insensitive to some directions on the sky. The inversion of this matrix therefore requires regularization, which is accomplished by diagonalizing the Fisher matrix and removing the eigenvalues that are close to zero (i.e. typically setting about 1/3 of the lowest eigenvalues

to infinity) [111]. The subscript R in Γ_R^{-1} denotes that the Fisher matrix has been regularized. The regularization does not induce a bias on the clean map $\hat{P}_\mu$.

The angular resolution of this technique is set by a diffraction-like limit [111]:

$$\theta = \frac{c}{2d\,f} \approx \frac{50\,\mathrm{Hz}}{f_\alpha}\,, \tag{2.11}$$

where θ is in radians, d is the distance between H1 and L1 (3000 km), and f_α is typically taken to be the most sensitive frequency in the detector band for a power-law SGWB with spectral index α, and for the given detector noise power spectra [88, 114]. For the BBH/BNS background, $\alpha = 2/3$ and the most sensitive frequency in the past searches was found to be 50-60 Hz, implying a coarse angular resolution of order $\theta \approx \pi/3$ and therefore spherical harmonic decomposition up to $\ell_{\rm max} = \pi/\theta \approx$ 3-4 [88, 112].

In order to probe finer angular scales, the above analysis is conducted in several narrower frequency bands with 50 Hz width: 50-100, 100-150, 150-200, and 200-250 Hz. The higher frequency bands result in better angular resolution, specifically in $\ell_{\rm max} = 4$, 8, 12, and 16, respectively. For the highest $\ell_{\rm max} = 16$, the corresponding angular resolution is $\theta \approx 7.3$ deg. However, the sensitivity of the search is reduced at higher frequencies, both because of the poorer strain sensitivity of the GW detectors above $\sim$ 100 Hz [86, 87], and because of the f^3 term in equation (2.2).

The above analysis procedure is applied to the GW data from the second observing run of aLIGO's detectors H1 and L1. Following the O2 directional searches paper [112], the Virgo data is not included, because Virgo participated for only the last month of O2, which was six months long in total, and because its noise level was higher than that for the LIGO detectors. Hence, including Virgo in this analysis would not result in a significant sensitivity improvement. The O2 data are collected from 16:00:00 UTC on 2016 November 30 to 22:00:00 UTC on 2017 August 25 [112]. I follow the data processing procedure described in [88, 112] and use the same data selection criteria in [112]. Finally, I compute the clean map estimates following equation (2.8), for each of the four frequency bands. The resulting clean maps, sigma maps, and signal-to-noise (SNR) maps for the four frequency bands are shown in Figure 2.1.

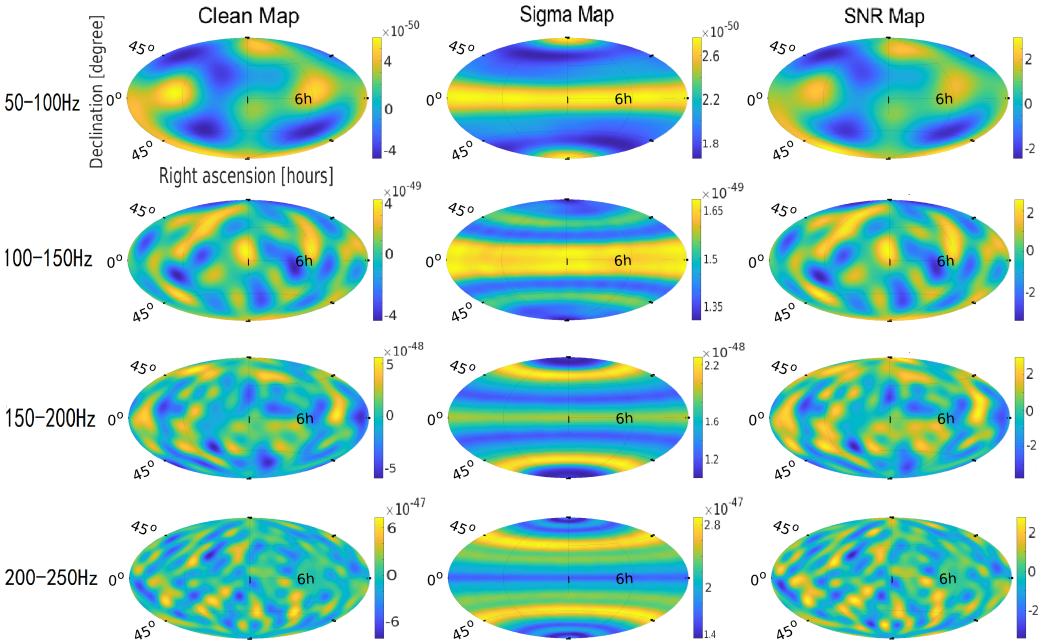

Figure 2.1: LIGO O2 clean maps, sigma maps and signal-to-noise (SNR) maps for the four frequency bands of 50-100, 100-150, 150-200, and 200-250 Hz from top to bottom, with α of 2/3 and $\ell_{\max}$ of 4, 8, 12 and 16, respectively. The horizontal and vertical axis are right ascension in hours and declination in degrees, as shown in the top left panel.

2.3 Galaxy Count Anisotropy

As an example of an EM tracer of matter structure, I use the distribution of galaxy counts across the sky. One of the most complete and largest sky coverage galaxy surveys is the Sloan Digital Sky Survey (SDSS), whose Data Release 16 (DR16) contains observations through 2018 August [115]. The SDSS imaging data contain observations covering almost 1.5×10^4 deg^2 or roughly one third of the sky. The photometric catalog includes approximately 2×10^8 galaxies of the r-band magnitude brighter than $m_r \approx 22.2$. In addition to the imaging observations, SDSS acquired spectra for $\approx 1.8 \times 10^6$ galaxies brighter than $m_r \approx 17.7$. For galaxies fainter than this limit, SDSS provides an estimate of the galaxy photometric redshift based on the analysis of the five photometric bands (hereafter, photo-z). Although the resulting redshifts are substantially more uncertain than those derived from spectroscopic observations, the use of photo-z allows us to increase the sample size considerably.

From the SDSS archive, I select all *galaxies* with magnitudes in the $17 < m_r \leq 21$ range and use the SDSS *type* parameter ($type = 3$) to identify only galaxies. This magnitude range is chosen to ensure a survey completeness level of 90 percent or better, and to minimize the contamination to the galaxy sample by misclassified stars [116]. I also constrain the analysis to include data in a fully contiguous area mostly in the northern Galactic hemisphere. The final photometric galaxy catalog includes 23 million objects with a median photometric redshift of 0.33. For a subsample of 1.4 million galaxies, spectroscopic redshifts are available, with a median spectroscopic redshift of 0.39.

A number of systematic effects can potentially affect the spatial distribution of galaxies on the large scales relevant for the cross-correlation with the GW maps. Here, I consider only the effects of atmospheric seeing variation and Milky Way extinction, as they impact the observed galaxy number counts on degree scales and above [117, 118]. I follow [116] and consider in the analysis only areas of good seeing and minimal Galactic extinction. The seeing is quantified using the average full width at half-maximum (FWHM) of the point spread function during the observations, I exclude from the analysis those sky regions with average FWHM ≥ 1.5 arcsec. This cut is found to exclude ~ 12 percent of the total area. Galactic extinction is characterized via the color excess, $E(B-V)$, I exclude areas with $E(B-V) > 0.13$, which is 15 percent of the total area.

The seeing and galactic extinction cuts can have significant effects on the average number of galaxies in some areas of the sky. In order to obtain unbiased galaxy count maps, the following procedure is applied. In the `HEALPix` [119] basis, the full sky is divided into pixels of the same angular size, which is a convenient choice for the computations of cross-correlations with the GW sky maps. The number of pixels in the `HEALPix` basis is chosen to match the value of $\ell_{\rm max}$ for each frequency band:

$$\#\,\text{pixels} \approx \frac{4\pi}{\theta^2} = \frac{4}{\pi}\,\ell_{\rm max}^2\,. \tag{2.12}$$

A galaxy count map of resolution corresponding to $\ell_{\rm max} = 16$ is needed, which corresponds to an angular scale of $\sim 7^\circ$. In order to compute the systematics in every pixel, I start by producing a `HEALPix` map for the SDSS photometric catalog with a higher resolution, equivalently smaller pixels. These small pixels have an angular scale of 2.4°, which is small enough so that the seeing and galactic extinction do not vary too much for the galaxies within the pixels,

meanwhile is large enough to ensure containing a large number of galaxies (on average $> 10^2$ galaxies). Then I compute the average r-band seeing and extinction for all galaxies in every small pixel. If the average seeing is greater than 1.5 arcsec or the galactic extinction is > 0.13, then all galaxies within this pixel are rejected. To correct for the effect of rejecting pixels, I replace the galaxy count in the rejected pixel with the average galaxy count of all the other small pixels inside one large `HEALPix` pixel corresponding to $\ell_{\rm max} = 16$. Since all objects in the SDSS spectroscopic catalog are also in the SDSS photometric catalog, the same procedure is applied to the spectroscopic catalog as well. The results for both catalogs are shown in Figure 2.2. Since the SGWB due to BBH and BNS mergers at different angular scales is expected to be dominated by binaries at different redshifts [98], I conduct the analysis in several redshift bins, i.e. compute the correlation between SGWB sky maps and the galaxy number sky maps in each redshift bin, respectively. I choose to divide both catalogs into redshift bins of width 0.1 (i.e. 0.0-0.1, 0.1-0.2,...). For the photometric catalog, I extend the analysis up to redshift 0.6, which includes 97 percent of all the galaxies. For the spectroscopic catalog, I go up to 0.7 and the redshift slicing includes 98 percent of galaxies. While the photometric and spectroscopic catalog maps including all redshifts do not appear to be correlated (as shown in Figure 2.2), I confirm that the photometric and spectroscopic maps in each redshift bin are highly correlated.

2.4 SGWB-EM Correlations

Having produced the sky maps for the SGWB in each of the four frequency bands and for the galaxy counts in each of the redshift bins, I then compute the correlations between these maps. Denoting the SGWB energy density in a pixel i as $M_{{\rm GW},i}$ and the galaxy number count in the same pixel as $M_{{\rm GC},i}$, let's define the corresponding fluctuations:

$$\delta M_{{\rm GW},i} = M_{{\rm GW},i} - \langle M_{\rm GW}\rangle, \;\; \delta M_{{\rm GC},i} = M_{{\rm GC},i} - \langle M_{\rm GC}\rangle \,. \tag{2.13}$$

Then we can define the coherence between these fluctuations as

$$\Gamma = \frac{\langle \delta M_{\rm GW}\, \delta M_{\rm GC}\rangle^2}{\langle \delta M_{\rm GW}^2\rangle \langle \delta M_{\rm GC}^2\rangle} \,, \tag{2.14}$$

where the averages (denoted in angle brackets) are computed over all pixels in the corresponding maps.

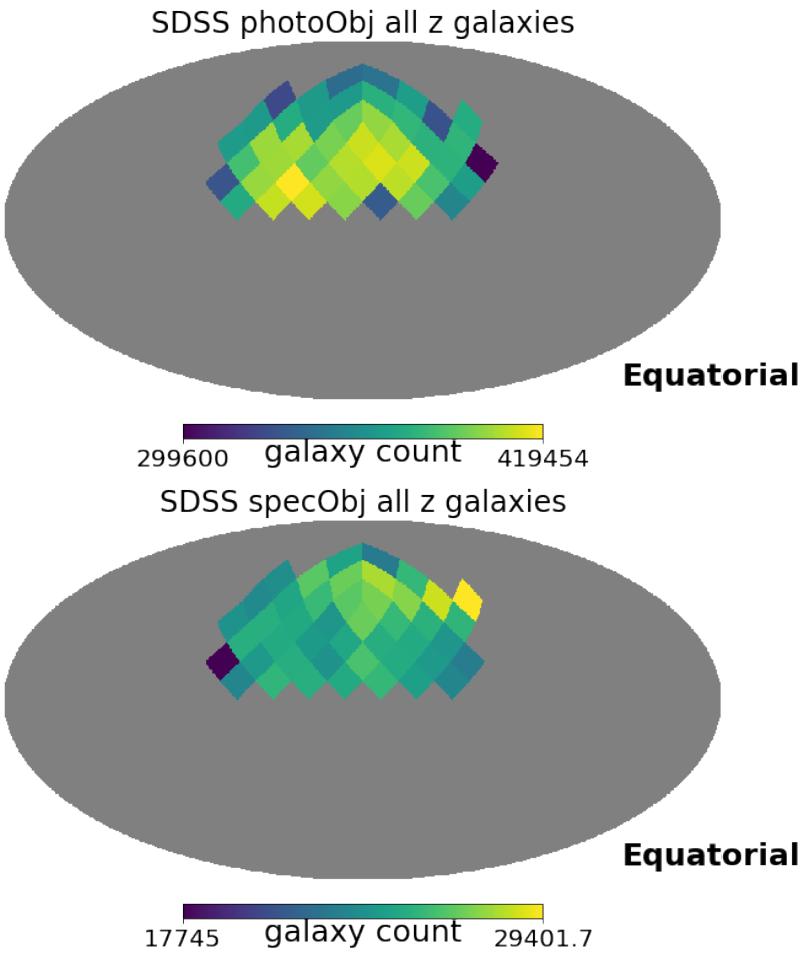

Figure 2.2: `HEALPix` sky maps of SDSS galaxy number counts for an angular resolution corresponding to $\ell_{\rm max} = 16$, after applying the data quality cuts described in the text for the photometric catalog (top) and the spectroscopic catalog (bottom). The color scales with the galaxy count in each pixel.

To assess the significance of the measured coherence, I use simulations. In particular, I generate 10,000 simulated SGWB noise maps assuming zero-mean multivariate Gaussian distribution for $P_{\ell m}$'s described by the regularized inverse Fisher matrix obtained from LIGO data (see Section 2.2). Then I compute Γ for these simulated maps and the galaxy count sky maps in different redshift bins respectively. I then compute the false alarm rate (FAR) as a function of

coherence:

$$\mathrm{FAR}\,(\Gamma) = \frac{\#\,\text{of events} > \Gamma}{\text{total}\,\#\,\text{of events}}\,. \tag{2.15}$$

Figure 2.3 shows an example of the FAR calculation for the specific case of the 50-100 Hz band SGWB map and the full photometric SDSS galaxy catalog. The blue curve is derived from the 10,000 simulations and the red dot denotes the actual measured coherence using the O2 LIGO data. The FAR value of the red dot then gives the *p*-value significance of the measured coherence.

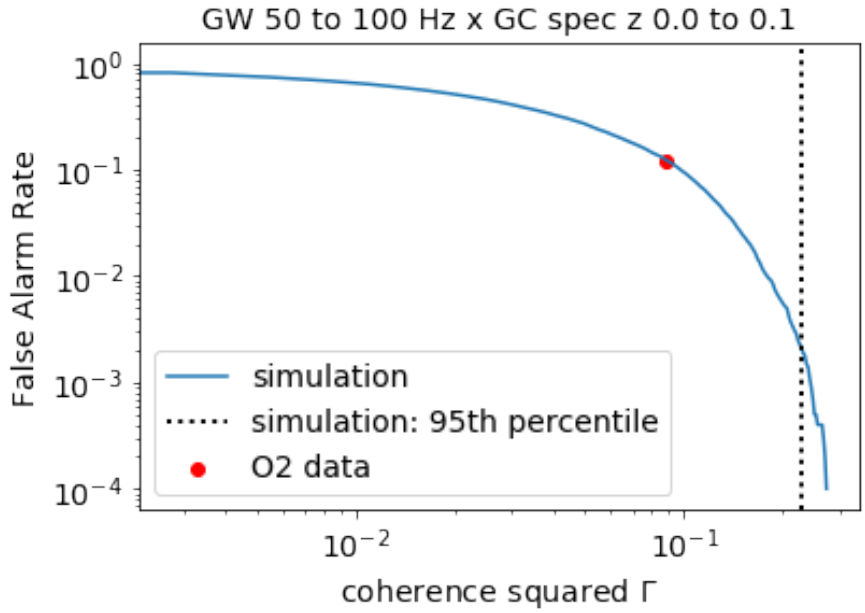

Figure 2.3: The FAR of the coherence squared Γ distribution of 10,000 simulated SGWB sky maps in the 50-100 Hz band and the galaxy count sky maps from the full photometric SDSS catalog (blue curve). The coherence squared Γ obtained from the LIGO O2 data and the same galaxy map is represented as a red dot. The black vertical dashed line represents the 95 percentile of the 10,000 simulations.

I repeat this procedure for all four frequency bands of the GW data and all redshift bins of the SDSS data, and for both the photometric and spectroscopic SDSS catalogs. The resulting *p*-values are shown in Figure 2.4. The *p*-values for the photometric catalog have wider spread than the spectroscopic catalog, which can be explained by the fact that the photometric catalog

Table 2.1: λ_{95} values in units of st^{-1}, for the four GW frequency bands and for the photometric and spectroscopic catalogs assuming the full redshift ranges.

GW frequency (Hz)	50-100	100-150	150-200	200-250
GC photoz	2.7e-49	1.0e-50	1.7e-47	2.1e-47
GC specz	1.1e-49	1.0e-48	1.0e-47	1.2e-46

is more uncertain in redshift and therefore more noisy as galaxy count maps in redshift slices. Above all, it is evident that all p-values are at or above (10^{-1})–(10^{-2}) for both the photometric and spectroscopic galaxy count maps, indicating low statistical significance. Therefore, there is no observation of correlation between SGWB and galaxy count sky maps.

Note that this analysis can be extended to perform model selection and/or parameter estimation. For this chapter, I consider a simple empirical model where I assume that the SGWB energy density fluctuations are proportional to the normalized galaxy density fluctuations:

$$\delta M_{\mathrm{GW},\,i}^{\mathrm{model}} = \lambda \frac{\delta M_{\mathrm{GC},\,i}}{\langle M_{\mathrm{GC},\,i} \rangle} + \delta M_{\mathrm{GW}}^{\mathrm{noise}} \,, \tag{2.16}$$

where the index $i = 1, 2$ represents galaxy count maps of the photometric or spectroscopic catalogs in the full redshift range. The factor λ can therefore be interpreted as the GW strain power per normalized fluctuation in the galaxy number count. One can use the observed value of Γ to constrain the model parameter λ. To do so, I scan the values of the scaling parameter λ: for each value of λ I generate 1000 realizations of the SGWB noise map $\delta M_{\mathrm{GW}}^{\mathrm{noise}}$ similarly to above, and for each realization, I compute the coherence Γ between the corresponding model $\delta M_{\mathrm{GW},\,i}^{\mathrm{model}}$ and the galaxy count map $\delta M_{\mathrm{GC},\,i}$.

Figure 2.5 shows an example of Γ as a function of λ, computed using the SGWB map in the 50-100 Hz frequency band and the full photometric SDSS catalog. Let's define λ_{95} to be the 95 percent confidence upper limit on the scaling factor, i.e. the value of λ that yields coherence Γ larger than the observed coherence in 95 percent of the simulations. For the example shown in Figure 2.5, it is shown that $\lambda_{95} = 2.7 \times 10^{-49}\ \mathrm{st}^{-1}$. This calculation is repeated for all frequency bands for both photometric and spectroscopic catalogs, and the corresponding λ_{95} values are summarized in Table 2.1.

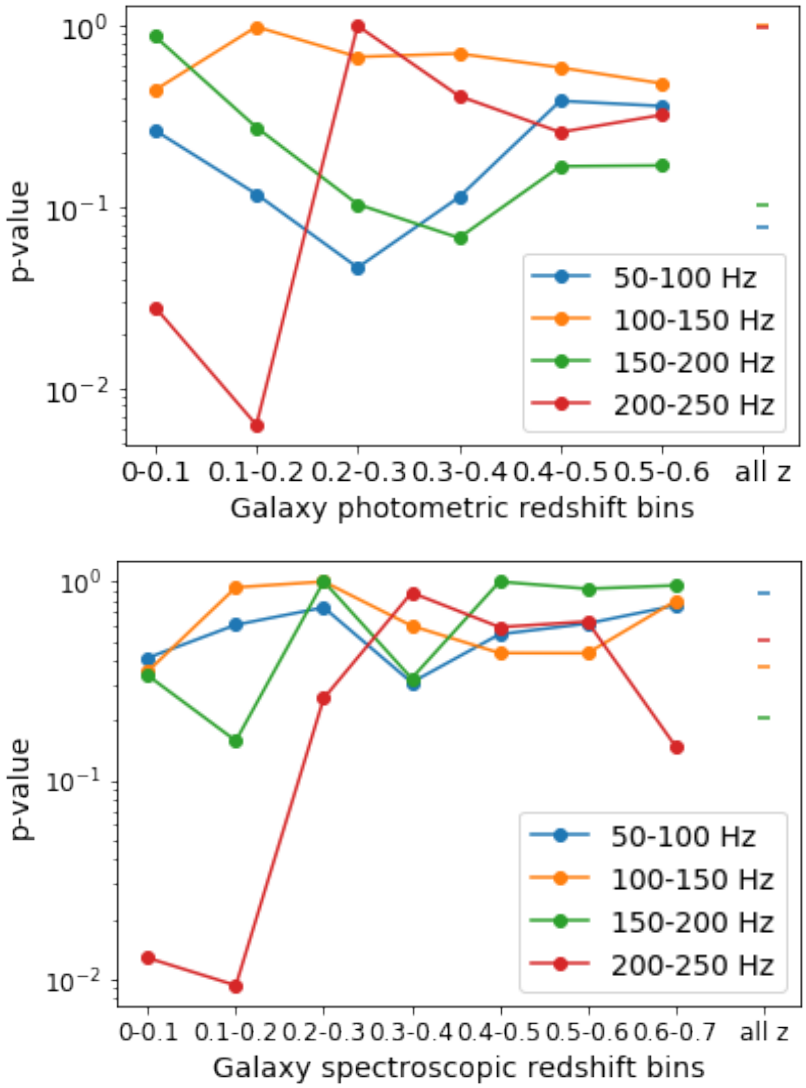

Figure 2.4: The p-value significance of the coherence between the LIGO O2 SGWB maps in different frequency bins and the SDSS galaxy count maps in different redshift slices are shown for the (top) photometric and (bottom) spectroscopic SDSS catalogs. Note that the red and orange underscore in the top figure are partially overlapping. All p-values are larger than (10^{-1})-(10^{-2}), indicating no evidence for correlations between the SGWB and galaxy count maps.

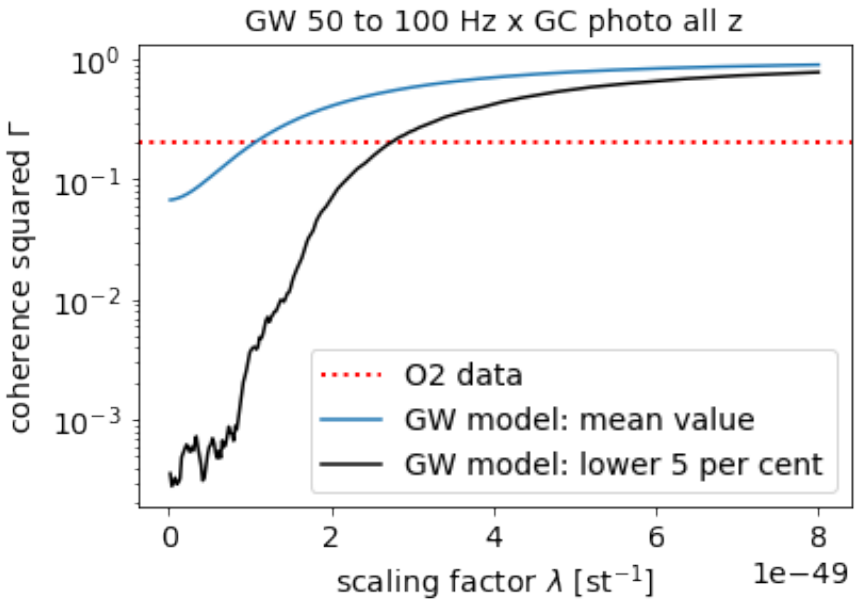

Figure 2.5: Coherence squared Γ for simulated SGWB model maps described in the text is shown as a function of the scaling parameter λ, for the case of SGWB map in the 50-100 Hz band and for the full photometric SDSS catalog. The SGWB model maps were generated by adding the normalized galaxy count map scaled by parameter λ to the SGWB noise map realizations, as defined by equation (2.16). The corresponding mean Γ and its 5th percentile (obtained over 1000 noise realizations at each λ value) are plotted as a function of λ. The red dashed line denotes the Γ value obtained using the O2 data for the same GW band and galaxy catalog. The intersection point between the red dashed line and the 5th percentile curve gives the λ_{95} value.

2.5 Discussion and Conclusions

Searching for the cross-correlations between the SGWB and EM tracers of matter structure offers the possibility of both detecting the SGWB anisotropy sooner and probing cosmological and astrophysical parameters driving the formation of structure. In this chapter, I presented a formalism to measure such SGWB-EM correlations. I used the LIGO data from the O2 and the galaxy catalog data from the SDSS to study the cross-correlations of different GW frequency bands and different redshift slices in galaxy catalogs. I found no evidence for correlations between the SGWB and galaxy catalogs in these data.

There are many possible directions that can be explored in future works. I list some of them

here as follows:

1. In this work I used only galaxy counts to track the matter structure. This can be expanded to use weak lensing survey data, or the cosmic microwave and infrared background data [e.g. from Planck [120, 121]], or the X-ray data measured by *Chandra* X-ray Observatory [122]. Different EM tracers may potentially correlate with different components of the SGWB: for example, galaxy counts or weak lensing may correlate with BBH/BNS SGWB, while the CMB anisotropy may correlate with cosmological SGWB models. Hence, spatial correlations with different EM tracers can help distinguish different SGWB sources.

2. In this work I used LIGO O2 data and galaxy count in SDSS. I will proceed in the next chapter with Advanced LIGO O3 data which results from upgrades of the detectors and improvements of the sensitivity; For galaxy surveys, the *Euclid* [123] and *SPHEREx* [124] missions are expected to produce galaxy surveys that will cover larger parts of sky and see deeper in observational limits as compared to the SDSS catalogs.

3. The Bayesian approach proposed to measure the BBH SGWB [90, 125] promises to be significantly more sensitive to this type of background than the traditional stochastic search techniques (also used in this chapter). This approach can produce the Bayesian posterior distribution of the BBH sky positions which can be used as SGWB maps in this work, and it can possibly extract the redshift distribution of the BBH population, giving rise to the possibility of studying 3D correlations (sky position plus redshift) between the BBH SGWB and the galaxy count catalogs [126].

4. In this work I used a simple empirical model of the correlation between SGWB and galaxy counts to estimate a scaling parameter. This can be expanded to include more sophisticated models of the BBH/BNS SGWB that properly take into account the cosmological and astrophysical evolution [70, 71, 96, 98, 99]. I will explore this in the next Chapter.

In conclusion, searching for the SGWB-EM correlations is a new path for using multi-messenger data to probe astrophysics and cosmology. Upcoming data sets from both GW and EM detectors and telescopes, together with improvements in data analysis techniques, offer innovative approaches to investigating the evolution of structure in the Universe, and perhaps also models of the early Universe.

Chapter 3

Cross-Correlating Angular Power Spectra of Stochastic Gravitational Wave Background and Galaxy Over-Density

3.1 Introduction

Building on Chapter 2, in this chapter I expand my search for cross-correlations between SGWB and galaxy number counts to include model inference. As stated in Chapter 1, SGWB energy density may be correlated with anisotropies in electromagnetic observables such as galaxy counts.

Cosmological SGWB sources produce weak anisotropies ($\sim 10^{-5}$) with a scale-invariant angular power spectrum $\ell(\ell+1)C_\ell \propto$ constant (ℓ parametrizes the angular scale) [104], while astrophysical sources, shaped by large-scale structure, show stronger anisotropies ($\sim 10^{-2}$) and a different scaling given by clustering: $(\ell+1)C_\ell \propto$ constant [61, 70, 71, 91–94, 96, 98, 99, 127–129].

Cosmological SGWB components are continuous and stationary over the observation time, forming an *irreducible* background. Meanwhile, the astrophysical SGWB has a discrete, *popcorn-like* character, leading to a dominant Poissonian shot-noise term in its angular power spectrum

compared to the clustering term [93, 94, 98, 129]. Cross-correlating with galaxy maps can help extract the clustering signal [129].

Cross-correlations are not only observables of structure, but also help to detect SGWB anisotropy by offering higher signal-to-noise ratio (SNR) than the SGWB auto-correlation [96, 98, 129–131] when considering extra-galactic astrophysical GW background.

In this chapter, I focus on the cross-correlations between the anisotropies of SGWB (measured in the third observing run of Advanced LIGO) and the distribution of galaxies across the sky (from SDSS spectroscopic catalog). Assuming that extragalactic compact binary mergers dominate the SGWB around 100 Hz, I use a parameterized astrophysical model in [96, 98, 127] to describe the galactic process of GW emission, and compute the corresponding angular power spectrum of cross-correlation, then compare it to the angular power spectrum extracted from data. Finally I perform a parameter estimation and obtain constraints on the model parameters.

This chapter is structured as follows. In Section 3.2 I will introduce the model predictions for the angular power spectrum of the cross-correlation between SGWB and the galaxy counts distribution. In Section 3.3, I will present the measurement of angular power spectra of SGWB sky maps in narrow frequency bands. In Section 3.4 I will present the measurement of the angular power spectra of the galaxy sky maps from SDSS spectroscopic catalog. In Section 3.5 I will present the measurement of the angular power spectra of SGWB-GC cross-correlation. In Section 3.6 I will use the measured angular power spectra from Section 3.5 to estimate the model parameters introduced in Section 3.2. Finally in Section 3.7, I will conclude my work in this chapter and discuss possible improvements in the future.

3.2 Modeling SGWB-Galaxy Count Angular Power Spectra

3.2.1 Astrophysical Models of Angular Power Spectra

As discussed in Chapter 2, the GW energy density spectrum $\Omega_{\rm GW}(\mathbf{e}, f)$ is a dimensionless quantity that depends on frequency f and angular direction $\mathbf{e}$, and is defined as the GW energy density $\rho_{\rm GW}$ observed in infinitesimal range of logarithmic frequency ($\mathrm{d}\ln f$) and solid angle ($\mathrm{d}^2\mathbf{e}$), then normalized by the critical density of the Universe today $\rho_{\rm c} = 3H_0^2/(8\pi G)$. (The the speed of light is set to be $c = 1$.) We can separate it into two parts: the isotropic background $\bar{\Omega}_{\rm GW}$ which is uniform over all directions, and the anisotropic fluctuation $\delta\Omega_{\rm GW}$ which depends on

the solid angle **e** [70, 71, 98]:

$$\Omega_{\rm GW}(\mathbf{e}, f) = \frac{f}{\rho_{\rm c}} \frac{{\rm d}^3\rho_{\rm GW}}{{\rm d}^2\mathbf{e}\,{\rm d}f}(\mathbf{e}, f) = \frac{\bar{\Omega}_{\rm GW}(f)}{4\pi} + \delta\Omega_{\rm GW}(\mathbf{e}, f)\,. \tag{3.1}$$

The isotropic background is the integral over conformal distance $r = c\,\eta$ where η is the conformal time. r is related to redshift z by a function $z = z(r)$ [132, 133]. The integration range is $[r_*, r_{\rm O}]$, where r_* stands for a maximum distance above which there are very few astrophysical sources, and $r_{\rm O}$ stands for the conformal time today;

$$\bar{\Omega}_{\rm GW}(f) = \int_{r_*}^{r_{\rm O}} {\rm d}r\,\partial_r\bar{\Omega}_{\rm GW}(f, r),\ \partial_r\bar{\Omega}_{\rm GW}(f, r) = \frac{f}{\rho_{\rm c}}\,\mathcal{A}(f, r)\,, \tag{3.2}$$

where the partial derivative of the background over distance can be written as a function of frequency, critical density and the astrophysical kernel $\mathcal{A}(f, r)$. The kernel is related to the GW energy produced in the galaxy source frame by [129]

$$\mathcal{A}(f, r) = \frac{a^4}{4\pi}\int {\rm d}\mathcal{L}_{\rm GW}\,\bar{n}_{\rm G}(\mathcal{L}_{\rm GW}, r)\,\mathcal{L}_{\rm GW}\,, \tag{3.3}$$

where a is the Universe scale factor, $\bar{n}_G$ is the average number density of galaxies at distance r, and $\mathcal{L}_{\rm GW}$ is the GW luminosity. As stated in Chapter 1, astrophysical sources of GWs can be CBCs (BBH, BNS, BHNS), rotating neutron stars and core-collapse supernovae. These sources are hosted within galaxies, therefore they reflect the underlying processes of galactic evolution and star formation. Here we focus on SGWB from BBHs. In [98], they constructed a reference model that depends on several parameters, as well as several alternative models, each differing from the reference model in one key aspect, keeping the other parameters fixed. For example, the BH mass cutoff $M_{\rm co} = 45\,M_\odot$ for the reference model, it is $40\,M_\odot$ for the *dMco* model and is $50\,M_\odot$ for the *uMco* model. The reference model assumes the stellar Salpeter-like initial mass function (IMF) has a slope $p = 2.35$ [134], it is 2.6 for the *imf-high* model and is 2.1 for the *imf-low* model. The reference model assumes the initial separation of the BHs is distributed over the scale factor of the Universe a as $P(a) \propto a^{-1}$, which is equivalently for the delay time $P(t_{\rm d}) \propto t_{\rm d}^{-1}$. The *aconst* model stands for $P(a) \sim$ const. The model *limongi* uses a set of stellar evolution models proposed by Marco Limongi in [135], while the reference model uses the ones in [136]. These various astrophysical models describe the kernel in different scenarios [98]. Figure 3.1 shows the astrophyscial kernel $\mathcal{A}$ at fixed frequency $f = 63\,{\rm Hz}$ as a function of redshift for

different astrophysical models.

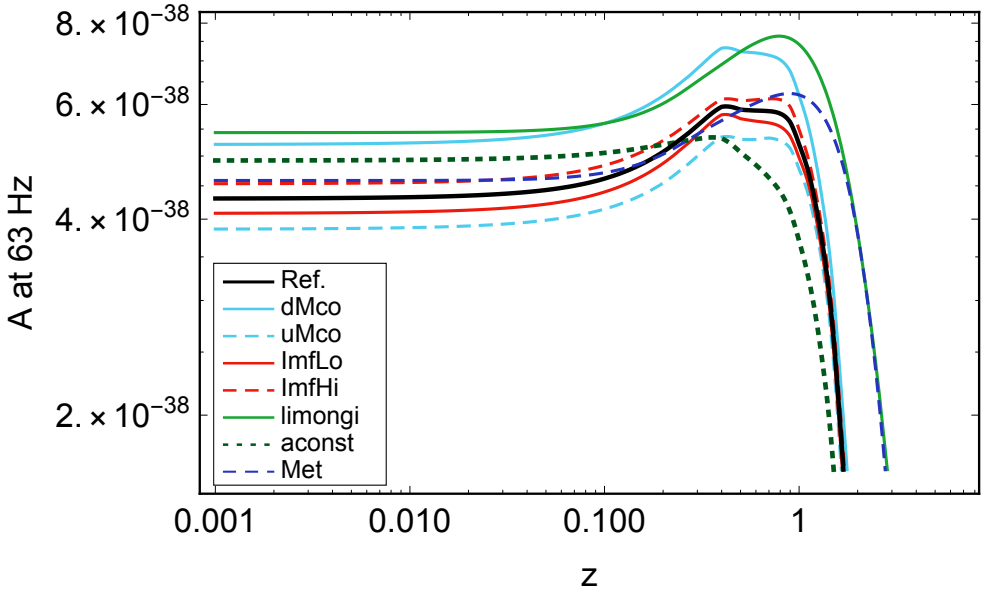

Figure 3.1: The astrophyscial kernel $\mathcal{A}$ at fixed frequency $f = 63\,\mathrm{Hz}$ as a function of redshift for different astrophysical models. This figure is from [98].

Detailed calculation of the model and of the kernel is computationally expensive, therefore I need to use an empirical approximation of Eq. (3.3). For the frequency dependence of the the kernel, as discussed in Chapter 2, for the BBH/BNS background, it follows the power law of $\Omega_{\rm GW} \sim f^{2/3}$ in the frequency band where $f \lesssim 100$ Hz. For the redshift dependence of the kernel at low redshifts ($z \leq 2$), the astrophysical models' prediction can be approximated to the leading order by a Gaussian parameterization. Together we have

$$\mathcal{A}(f, z) = \mathcal{A}(f)\, \mathrm{e}^{-(z-z_c)^2/2\sigma_z^2} = A_{\rm max}\, f^{-1/3}\, \mathrm{e}^{-(z-z_c)^2/2\sigma_z^2}\,, \tag{3.4}$$

note that we're switching from r to z from now on. This kernel has three parameters: $\theta = (A_{\rm max},\, z_c,\, \sigma_z)$, where $A_{\rm max}$ represents the amplitude of the kernel, z_c stands for the peak redshift and σ_z being the peak width. By fitting all the astrophysical models' predictions of the kernel in [98], I find that the peak redshift $z_c \in [0.3, 1.8]$ and the peak width $\sigma_z \in [0.3, 1.2]$. In Figure 3.2, we can see the astrophysical kernel predicted by a reference model as a function of redshift at two representative frequencies in the LIGO band [98], together with a power-law-Gaussian

fit at $z \leq 2$.

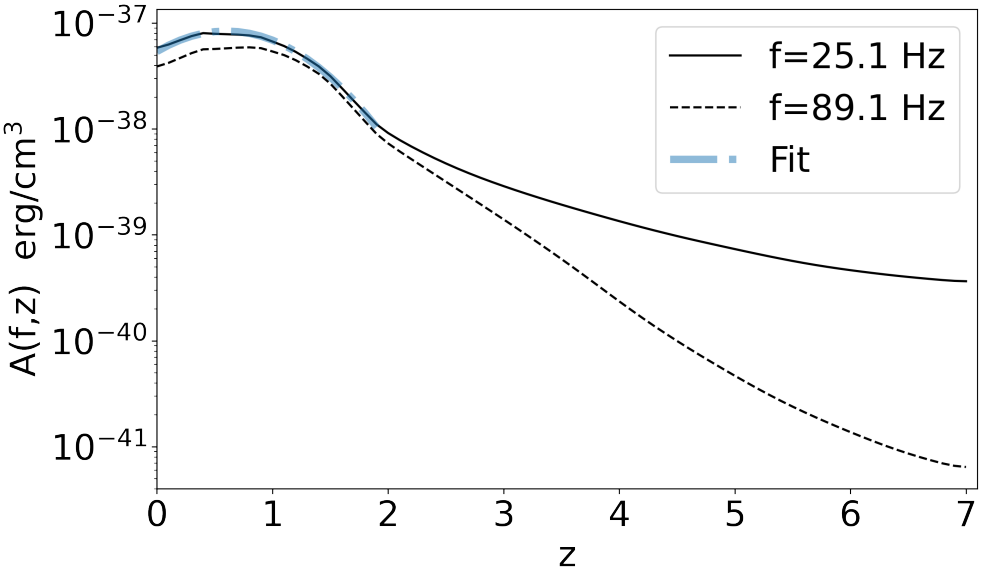

Figure 3.2: Astrophysical kernel for the astrophysical model used as a reference in [98], as function of redshift and for frequencies 25.1 and 89.1 Hz, with a power-law-Gaussian fit of $A_{\rm max} = 4 \times 10^{-37} \mathrm{erg\,cm^{-3}\,s^{-1/3}}$, $z_c = 0.6$, $\sigma_z = 0.9$.

Following the work in Chapter 2, I am searching for the cross-correlation between SGWB and galaxy number counts. Let us define this quantity Δ as the over-density of the galaxies number count per unit redshift and solid angle:

$$\Delta(\mathbf{e}, z) \equiv \frac{N(z, \mathbf{e}) - \bar{N}(z)}{\bar{N}(z)} \,. \tag{3.5}$$

In Chapter 2, I computed the cross-correlation of SGWB in frequency and redshift bins. In this chapter, I combine galaxies at all redshifts instead of slicing them into redshift bins so as to ensure maximized SNR of cross-correlation.

The angular power spectra of the GW and galaxy counts auto- and cross-correlations are

defined as functions of frequency f and astrophysical parameters θ

$$(2\ell+1)\,C_\ell^{\rm GW}(f;\theta) \equiv \sum_{m=-\ell}^{\ell} \langle a_{\ell m}(f;\theta)\, a^*_{\ell m}(f;\theta)\rangle\,, \tag{3.6}$$

$$(2\ell+1)\,C_\ell^{\rm GC} \equiv \sum_{m=-\ell}^{\ell} \langle b_{\ell m}\, b^*_{\ell m}\rangle\,, \tag{3.7}$$

$$(2\ell+1)\,C_\ell^{\rm cross}(f;\theta) \equiv \sum_{m=-\ell}^{\ell} \langle a_{\ell m}(f;\theta)\, b^*_{\ell m}\rangle\,, \tag{3.8}$$

where the bracket denotes an ensemble average and $a_{\ell m}(f)$ and $b_{\ell m}$ are the coefficients of the spherical harmonics decomposition of the SGWB energy density and galaxy number counts respectively:

$$\delta\Omega_{\rm GW}(\mathbf{e},f;\theta) = \sum_{\ell=0}^{\infty}\sum_{m=-\ell}^{\ell} a_{\ell m}(f;\theta)\, Y_{\ell m}(\mathbf{e})\,, \tag{3.9}$$

$$\Delta(\mathbf{e}) = \sum_{\ell=0}^{\infty}\sum_{m=-\ell}^{\ell} b_{\ell m}\, Y_{\ell m}(\mathbf{e})\,. \tag{3.10}$$

Following [70], the angular power spectra of the auto- and cross-correlation can be written as integrals over the wave-number k:

$$C_\ell^{\rm GW}(f;\theta) = \frac{2}{\pi}\int {\rm d}k\, k^2\, |\delta\Omega_{{\rm GW},\ell}(k,f;\theta)|^2\,, \tag{3.11}$$

$$C_\ell^{\rm GC} = \frac{2}{\pi}\int {\rm d}k\, k^2\, |\Delta_\ell(k)|^2\,, \tag{3.12}$$

$$C_\ell^{\rm cross}(f;\theta) = \frac{2}{\pi}\int {\rm d}k\, k^2\, \delta\Omega^*_{{\rm GW},\ell}(k,f;\theta)\,\Delta_\ell(k)\,. \tag{3.13}$$

The leading order term of the SGWB power is a Fourier-space integral over comoving distance r on the astrophysical kernel $\mathcal{A}$, the dark-matter over-density $\delta_{\rm m}$, the bias factor $b(z)$ and spherical Bessel functions j_l [137, 138]:

$$\delta\Omega_{{\rm GW},\ell}(k,f;\theta) = \frac{f}{4\pi\rho_{\rm c}}\int {\rm d}r\, \mathcal{A}(r,f;\theta)\,[b(r)\,\delta_{{\rm m},k}(r)\, j_\ell(kr)]\,. \tag{3.14}$$

The dark-matter over-density $\delta_{\rm m}$ is related to galaxy over-density by the bias factor $b(z)$. The bias factor is assumed to be independent of scale and evolves with redshift by $b(z) = b_0\,\sqrt{1+z}$, $b_0 =$

1.5,

Similarly the leading-order contribution to galaxy over-densities is given by an integral over the comoving distance, with the astrophysical kernel being replaced by a window function $W(r)$. This window function selects the redshift bin in the galaxy catalog being used in the cross-correlation, and is normalized to unity:

$$\Delta_\ell(k) = \int \mathrm{d}r\, W(r) \left[b(r)\, \delta_{\mathrm{m},k}(r)\, j_\ell(kr) \right]. \tag{3.15}$$

As mentioned above, I do not bin galaxies in redshift in this chapter, therefore I am using a square window function $W(r)$ which covers the entire range of redshift of the galaxy catalog I am using.

3.2.2 Shot Noise

The above contents in this chapter are based on two assumptions: 1) astrophysical sources are located in galaxies and are spatially distributed as a continuous field; 2) GW emission is continuous and stationary throughout the observation time. The stochastic gravitational wave background from compact binary coalescences, originating from a finite number of sources distributed across a finite number of galaxies, is subject to shot noise governed by Poissonian statistics in both space and time [93, 129]. This noise introduces additional anisotropic components to both the SGWB and the galaxy count distribution. Therefore, the observed angular power spectra C_ℓ's for both SGWB and GC, SGWB-GC cross-correlation and the corresponding covariance matrices will all be affected. Following the derivation in [129], the shot noise contribution to the cross-correlation angular power spectrum is independent of ℓ, but still dependent on astrophysical parameters $\theta = (A_{\max}, z_c, \sigma_z)$. Hence one can write the predicted C_ℓ^{cross} with shot noise as

$$C_\ell^{\mathrm{cross,tot}}(\theta) = C_\ell^{\mathrm{cross}}(\theta) + N_{\mathrm{shot}}^{\mathrm{cross}}(\theta), \tag{3.16}$$

where the first term on the right-hand side is the contribution from clustering, Eq. (3.13), and the second term is the contribution of shot noise.

If we only consider shot noise and omit instrumental noise, then the signal-to-noise ratio

(SNR) of the cross-correlation scales as [129]

$$\left(\frac{S}{N}\right)^2_{\rm cross} = \sum_\ell \frac{(2\ell+1)\, C_\ell^{\rm cross}}{\left(C_\ell^{\rm cross} + N_{\rm shot}^{\rm cross}\right)^2 + \left(C_\ell^{\rm GW} + N_{\rm shot}^{\rm GW}\right)\left(C_\ell^{\rm GC} + N_{\rm shot}^{\rm GC}\right)}\,, \tag{3.17}$$

where $C_\ell^{\rm GW}$ and $N_{\rm shot}^{\rm GW}$ are the angular power spectrum and the shot noise of the SGWB map, respectively, while $C_\ell^{\rm GC}$ and $N_{\rm shot}^{\rm GC}$ are the angular power spectrum and shot noise of the galaxy map (the parameter θ is omitted for simplicity).

The corresponding shot noise contributions are given by [129]

$$N_{\rm shot}^{\rm GW}(\theta) = \left(1 + \frac{1}{\beta_T}\right)\left(\frac{f}{4\pi\rho_{\rm c}}\right)^2 \int \frac{{\rm d}r}{r^2} \frac{1}{a^3\bar{n}_{\rm G}} \mathcal{A}^2(r, f; \theta)\,, \tag{3.18}$$

$$N_{\rm shot}^{\rm cross}(\theta) = \frac{f}{4\pi\rho_{\rm c}} \int \frac{{\rm d}r}{r^2} \frac{1}{a^3\bar{n}_{\rm G}} W(r)\, \mathcal{A}(r, f; \theta)\,, \tag{3.19}$$

$$N_{\rm shot}^{\rm GC} = \int \frac{{\rm d}r}{r^2} \frac{1}{a^3\bar{n}_{\rm G}} W^2(r)\,. \tag{3.20}$$

For the GW shot noise in Eq. (3.18), there is both spatial and temporal shot noise contribution, causing the $(1 + 1/\beta_T)$ pre-factor. β_T is the probability of each galaxy containing a merger during the observation time T, it is defined as

$$\beta_T \equiv \frac{T}{a^3\bar{n}_{\rm G}} \frac{{\rm d}^2\mathcal{N}}{{\rm d}t\, {\rm d}V}\,, \tag{3.21}$$

where $a^3\bar{n}_{\rm G}$ is the comoving number density of galaxies, which is assumed to be a constant value: $a^3\bar{n}_{\rm G} \sim 0.1$ Mpc^{-3}. Meanwhile, ${\rm d}^2\mathcal{N}/{\rm d}V{\rm d}t$ is the local merger rate of the GW detector. The above expressions are obtained assuming a monochromatic GW luminosity function and all galaxies emit GW. To estimate β_T, here I use the observed local rate of BBH mergers, as the value of the local rate of BNS or BHNS has large uncertainty, being: ${\rm d}^2\mathcal{N}/{\rm d}V{\rm d}t \sim 100$ Gpc^{-3}yr^{-1}. This estimate does not include the contribution of BNS or BHNS mergers, so it is a lower bound for the total merger rate in the ~ 100 Hz band, and it leads to a conservative estimate for the GW shot noise. For LIGO-Virgo-KAGRA O3, the observation time period was $T \sim 1$ yr. Together the estimate is $\beta_T \sim 10^{-6}$, and the pre-factor for shot noise of the GW map $\propto \beta_T^{-1}$ is significantly larger than those for the cross-correlation and galaxy map.

As for the SNR of cross-correlation, the denominator of Eq. (3.17) scales linearly with the

GW shot noise $N_{\rm shot}^{\rm GW}$ in Eq. (3.18), while the SNR of SGWB auto-correlation scales quadratically; therefore the SNR of cross-correlation is typically much larger than that of the SGWB auto-correlation (see [129] for a detailed analysis). The shot noise contribution to the cross-correlation is much smaller than the corresponding term for the SGWB auto-correlation, due to the fact that galaxy distribution does not associate with temporal but only spatial shot noise. Therefore, cross-correlating SGWB with galaxy distribution may be a promising method to obtain a first detection of the SGWB anisotropy.

3.3 Measurement of SGWB Angular Power Spectra

In this chapter, I measure the SGWB anisotropy using the LIGO O3 folded data set [139, 140] of H1 and L1 by dividing the data into 10 Hz-wide frequency bins from 20 to 100 Hz to analyze the frequency dependence of the astrophysical model in Section 3.2, then compute the unbiased estimator of the angular power spectra of SGWB. The difference from the O2 data I used in Chapter 2 is that O3 data uses $H_0 = 67.4\,\mathrm{km\,s^{-1}\,Mpc^{-1}}$ [141], with a reference frequency of $f_{\rm ref} = 25\,\mathrm{Hz}$. The choice of other parameters such as power-law index $\alpha = 2/3$ for a compact binary coalescence SGWB remains the same.

3.3.1 Unbiased Regularized Estimator

Following the data processing in Chapter 2, here I obtain the *dirty map* $X_{\ell m}$ and Fisher matrix $\Gamma_{\ell m,\ell' m'}$ from Eqs. (2.6,2.7) by summing over 192 second time-segments t and 1/32 Hz frequency bins f of the data in 10 Hz-wide f bins. Then I compute the *clean map* $\hat{P}_{\ell m}$ using Eq. (2.8). This is an unbiased estimator of the SGWB angular power:

$$\langle \hat{P}_{\ell m} \rangle = P_{\ell m}\,. \tag{3.22}$$

From Eqs. (2.9,2.10), we know that the Fisher matrix $\Gamma_{\ell m,\ell' m'}$ is the covariance matrix of the *dirty map*, while the inverse Fisher matrix $(\Gamma^{-1})_{\ell m,\ell' m'}$ is the covariance matrix of the *clean map*.

Since the *dirty map* is obtained by averaging over many time segments and frequency bins, according to the central limit theorem, the resulting $\hat{X}_{\ell m}$'s are multi-variate Gaussian variables with zero means and the covariance matrix being $\Gamma_{\ell m,\ell' m'}$. Further, since the *clean map* is obtained by a linear transformation of the *dirty map* as shown in Eq. (2.8), the $\hat{P}_{\ell m}$'s are also

multi-variate Gaussian variables with zero means and the covariance matrix being $(\Gamma^{-1})_{\ell m,\ell' m'}$.

Now we can introduce an estimator for the SGWB angular power spectrum that characterizes the scale of angular structures in the *clean map* by

$$\hat{C}_\ell = \frac{1}{2\ell+1} \sum_{m=-\ell}^{\ell} |\hat{P}_{\ell m}|^2 \,. \tag{3.23}$$

This is a biased estimator. I will show how to obtain an unbiased estimator from it after introducing the regularization method of the Fisher matrix in the following text.

The Fisher matrix $\Gamma_{lm,l'm'}$ needs to be regularized before inverting as the LIGO detectors are less sensitive in some directions in the sky (or equivalently, certain ℓm modes) than others. As a result, the determinant of the Fisher matrix is usually zero (or too small to cause numerical error), making the Fisher matrix not having an inverse. Therefore, one has to use instead a regularized pseudo-inverse, which modifies the original matrix to prevent numerical errors. Various regularization methods have been explored in the literature [111, 142–144]. Here I am using the most popular method: the singular value decomposition (SVD) regularization scheme [111]. As the Fisher matrix $\Gamma_{\ell m,\ell' m'}$ is a Hermitian matrix, one can decompose it into a product of three matrices:

$$\Gamma = USV^* \,, \tag{3.24}$$

where U and V are unitary matrices and S is a diagonal matrix with non-negative elements being the real eigenvalues of the Fisher matrix (s_i). Then the problematic ℓm modes will correspond to the smallest elements of S. I present the eigenvalues of the Fisher matrix in the 20–30 Hz GW data set as a function of the ℓm modes with $\ell_{\rm max} = 10$ in Figure 3.3.

In order to set a proper threshold on the eigenvalues of the Fisher matrix $S_{\rm min}$, below which all the lower-level eigenvalues will be replaced, we need to ensure that sufficient number of low-level eigenvalues are ruled out without increasing the level of numerical noise from less sensitive modes. Especially as I am using data in narrow frequency bands with a width of 10 Hz, this choice must be tested by the variance of the estimator and the induced biases. The eigenvalues lower than this threshold can be replaced either by infinity or by the smallest eigenvalue above this threshold. I have tested thresholds being $10^2, 10^3$ and 10^4 times smaller than the largest eigenvalue and also the two different replacements ($S_{\rm min}$ and infinity) in the 10 Hz-wide frequency bands stated above. After comparing the effects of the above regularization

parameters and methods, I decide to use the threshold parameter of 10^2 and replace all eigenvalues smaller than the threshold by $S_{\rm min}$. The regularized eigenvalues corresponding to this choice in the same frequency band are also shown in Figure 3.3.

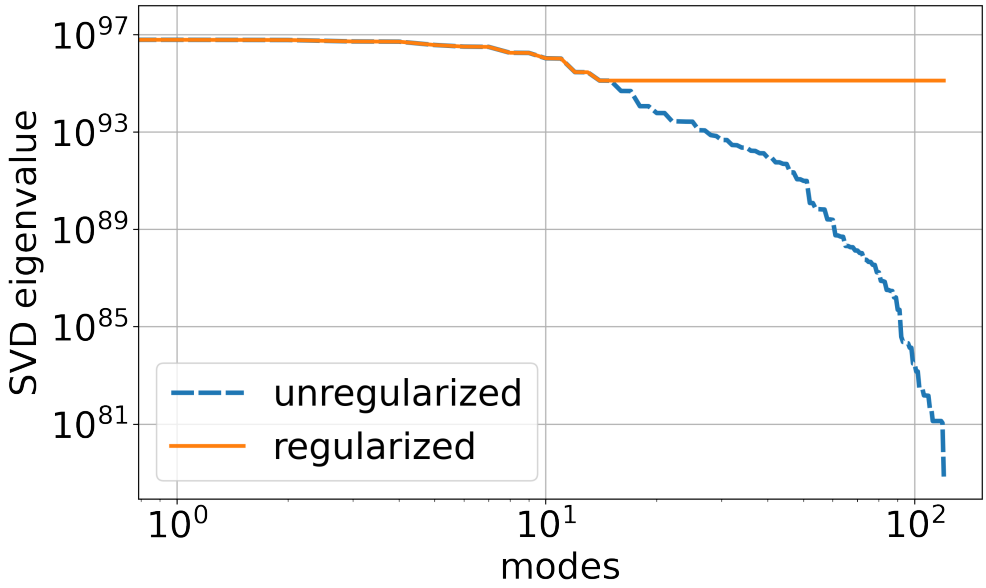

Figure 3.3: SVD eigenvalues of the Fisher matrix in the 20–30 Hz band are shown. Regularization of the Fisher matrix is accomplished by replacing eigenvalues smaller than $S_{\rm min}$ with $S_{\rm min}$, where $S_{\rm min}$ is defined to be 10^{-2} of the maximum eigenvalue and is depicted by the horizontal part of the orange line. This figure is plotted using the data from Jishnu Suresh and is taken from [145].

Given the regularized inverse Fisher matrix Γ_R^{-1} obtained by the method and parameter chosen above, the *clean map* in Eq. (2.8) then becomes [111, 146]

$$\hat{P}^R_{\ell m} = \sum_{\ell',m'} \left(\Gamma_R^{-1}\right)_{\ell m,\ell' m'} \hat{X}_{\ell' m'} \,, \tag{3.25}$$

which still obeys the multi-variate Gaussian distribution. The covariance matrix of this *clean map* in Eq. (3.25) under weak-signal approximation also takes a different form compared to the one in Eq. (2.10). It can be written as

$$K_{\ell m,\ell' m'} = \langle \hat{P}^R_{\ell m} \hat{P}^{R*}_{\ell' m'} \rangle - \langle \hat{P}^R_{\ell m} \rangle \langle \hat{P}^{R*}_{\ell' m'} \rangle = \Gamma_R^{-1}\, \Gamma\, \Gamma_R^{-1} \,, \tag{3.26}$$

here I did not write out the indices the Fisher and regularized inverse Fisher matrices for simplicity.

From the expectation value and uncertainty in the estimators defined in Eq. (2.9), one can show that the regularized SGWB angular power spectrum estimators obey

$$\langle \hat{C}_\ell^R \rangle \approx C_\ell + \frac{1}{2\ell+1} \sum_m (\Gamma_R^{-1})_{\ell m,\ell m} \,, \tag{3.27}$$

$$\langle (\hat{C}_\ell^R)^2 \rangle - \langle \hat{C}_\ell^R \rangle^2 \approx \frac{2}{(2\ell+1)^2} \sum_{mm'} |(\Gamma_R^{-1})_{\ell m,\ell m'}|^2 \,. \tag{3.28}$$

From the above equations we can see that the estimators of the *clean map* and the angular power spectra both depend on inverting the Fisher matrix $\Gamma_{\ell m,\ell' m'}$. Therefore these estimators are biased. The unbiased estimators of the SGWB angular power spectrum are then

$$\hat{C}'_\ell = \hat{C}_\ell^R - \frac{1}{2\ell+1} \sum_m (\Gamma_R^{-1})_{\ell m,\ell m} \,. \tag{3.29}$$

The covariance matrix of this unbiased estimator $\hat{C}'_\ell$ is given by Eq. (3.26).

3.3.2 Choice of Maximum Spherical Harmonics Expansion Degree

The choice of maximum spherical harmonics expansion degree $\ell_{\rm max}$ in the expansion in Eq. (2.4) is ultimately determined by the detector sensitivity and the frequency dependence of the searched SGWB model [144]. However, when the Fisher matrix is ill-defined, the regularization process introduces a bias that increases with $\ell_{\rm max}$. In particular, larger $\ell_{\rm max}$ leads to a Fisher matrix of larger size, regularization of a larger number of eigenvalues, therefore larger bias.

One way to assess this is to examine the diagonal entries of the Fisher and regularized inverse Fisher matrices, as in Figure 3.4. The Fisher matrix diagonal elements decrease significantly as ℓ increases for the same m. If the Fisher matrix could be inverted, the diagonal elements of the inverse Fisher matrix would correspondingly increase with ℓ for a fixed m. Figure 3.4 (bottom) indeed shows this increasing trend, but the trend saturates (reaches a plateau) after $\ell = 5$ due to the regularization scheme. Propagating this to the covariance matrix K for the *clean map* in Eq. (3.26) reveals that K could have artificially low values and implying artificially good sensitivity if one uses too large value of $\ell_{\rm max}$. In this chapter I choose $\ell_{\rm max} = 5$ to minimize the side effects of the regularization process.

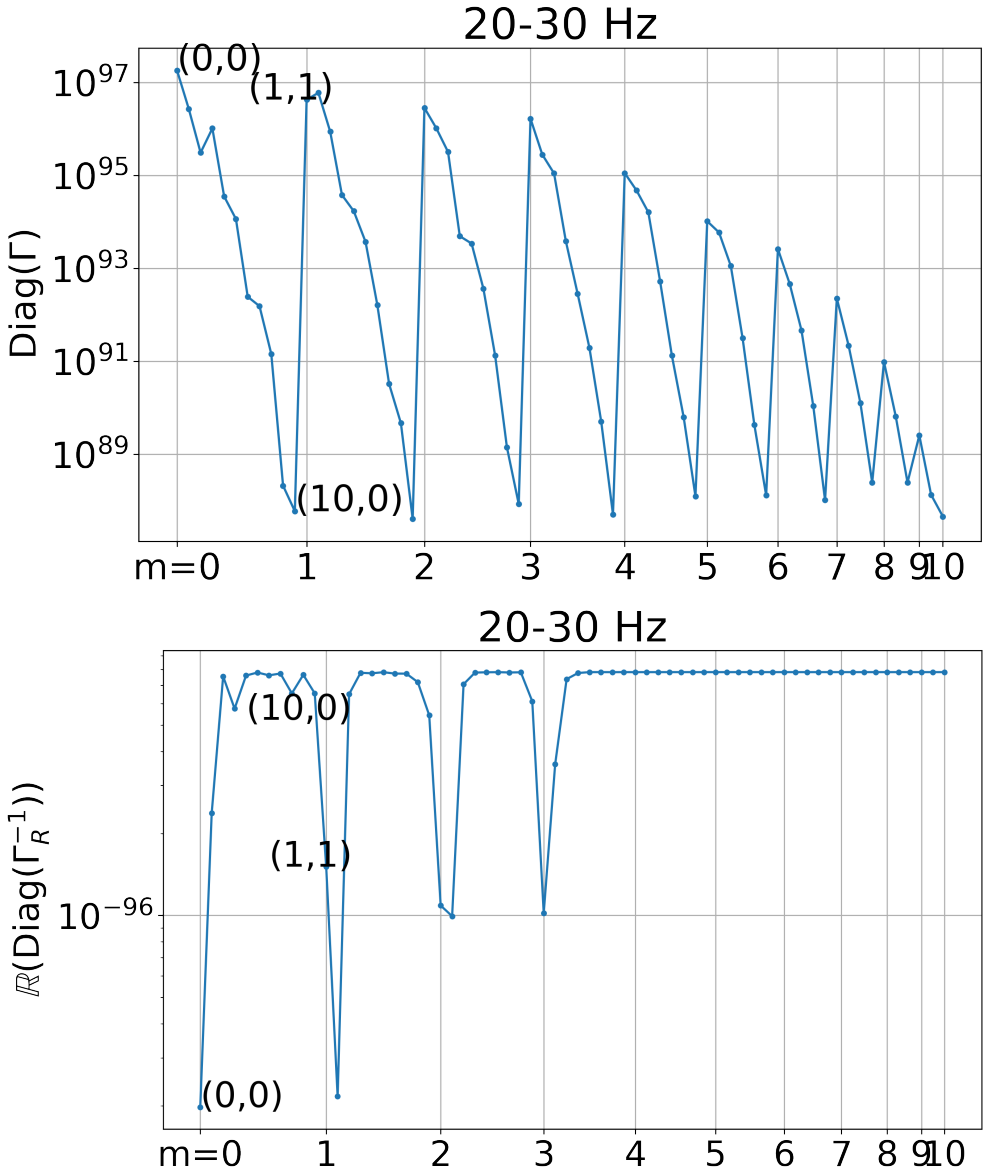

Figure 3.4: Diagonal entries of the SGWB Fisher matrix (top) and the real parts of its inverse Fisher matrix (bottom) are shown for the 20–30 Hz band, with regularization defined in the text. The indices along the x-axis are (ℓ, m)=(0,0),(1,0)...,($\ell_{\rm max}$,0),(1,1),..., ($\ell_{\rm max}$,1),...,($\ell_{\rm max}$-1,$\ell_{\rm max}$-1),($\ell_{\rm max}$,$\ell_{\rm max}$), with $\ell_{\rm max}$=10.

3.3.3 SGWB Angular Power Spectrum Estimator

In order to build my SGWB anisotropy estimator that is directly compatible with the astrophysical model in Section 3.2 with a definition of the SGWB anisotropy $\delta\Omega_{\rm GW}$ in Eq. (3.9), and following the definition of the same quantity in SGWB formalism in Eqs. (2.1-2.3), let us introduce a pre-factor:

$$\mathcal{K} \equiv \frac{2\pi^2 f_{\rm ref}^3}{3H_0^2}\left(\frac{f}{f_{\rm ref}}\right)^{\alpha} . \tag{3.30}$$

I then define frequency dependent estimators of the spherical harmonic coefficients of the *clean map* by scaling up $\mathcal{K}$ times:

$$\hat{a}_{\ell m}(f) = \mathcal{K}\hat{P}_{\ell m} . \tag{3.31}$$

These estimators will have expectation values that are consistent with the ones in the astrophysical model in Eq. (3.9). The covariance matrix of the above coefficients follows a squared power of scaling:

$$K^{\rm GW}_{\ell m,\ell' m'} = \mathcal{K}^2 K_{\ell m,\ell' m'} . \tag{3.32}$$

Then the frequency-dependent estimators of the SGWB angular power spectrum with proper normalization are

$$\hat{C}_\ell^{GW}(f) = \frac{1}{2\ell+1}\sum_{m=-l}^{l}|\hat{a}_{\ell m}(f)|^2 . \tag{3.33}$$

As stated above, these estimators are biased. The unbiased angular power spectrum of the SGWB auto-correlation is given by Eq. (3.29):

$$\hat{C}_\ell^{\prime GW}(f) = \hat{C}_\ell^{GW}(f) - \frac{\mathcal{K}^2}{2\ell+1}\sum_m (\Gamma_R^{-1})_{\ell m,\ell m} , \tag{3.34}$$

with their variance squared being Eq. (3.28) scaled by $\mathcal{K}^4$ as

$$\langle(\hat{C}_\ell^{\prime GW}(f))^2\rangle - \langle\hat{C}_\ell^{\prime GW}(f)\rangle^2 \approx \frac{2\,\mathcal{K}^4}{(2\ell+1)^2}\sum_{mm'}|(\Gamma_R^{-1})_{\ell m,\ell m'}|^2 . \tag{3.35}$$

The above analysis is applied to the LIGO O3 folded data set [139, 140] in 10 Hz-wide frequency bands between 20 to 100 Hz with $\ell_{\rm max} = 5$, in use of `PyStoch` pipeline [147, 148] to compute the unbiased $\hat{C}_\ell^{\prime GW}$ estimators of the angular power spectra and the corresponding $\hat{a}_{\ell m}$. The $\hat{C}_\ell^{\prime GW}$ estimators and their variance in these frequency bands are shown in Figure 3.5, as a

function of ℓ for different frequency bands (top panel) and as a function of frequency (center of every frequency bin) with various values of the multipole ℓ (bottom panel). This Figure shows that the SGWB auto power spectra in all 10 Hz-wide frequency bands and at all ℓs are consistent with zero at 2-σ, implying no evidence for an anisotropic SGWB in these data. Note that the error bars increase at higher frequencies, which is a consequence of the lower strain sensitivity of LIGO detectors at higher frequencies and of the power law frequency dependence in Eq. (3.30). These SGWB auto power and their error bars are consistent with the noise in [149]. It is not straightforward to have a one-to-one comparison, as my results are in 10 Hz-wide frequency bands, while the result in [149] is of a broadband search. Nevertheless, my result of the SGWB auto power is in good agreement with the all-sky all-frequency SGWB angular power spectra in [150].

3.4 Measurement of Galaxy Overdensity Angular Power Spectra

In this chapter, I again use the galaxy number count from the Sloan Digital Sky Survey (SDSS) [115], and compute the galaxy over-density angular power spectra based on its spectroscopic catalog, which contains 2.8 million galaxies with r-band magnitude $17 < m_r \leq 21$. I do not include stripe No. 82, which is scanned many more times compared to other stripes in the survey and is hence much brighter. This leaves us with 1.7 million galaxies, whose redshift range extends to 0.8, with a median redshift of 0.39. Similar to what I did in Chapter 2, the systematic issues in the survey are addressed following [130]. In particular, I select only galaxies with r-band seeing < 1.5 arcsec and extinction $E(B-V) < 0.13$. The seeing, or the angular size of astronomical seeing in a specific band of wavelength of light, represents the diameter of a blurred "seeing disk" in the image of a point source such as galaxy. It is denoted by the Full Width at Half Maximum (FWHM) in r-band in SDSS. The extinction is the absorption and scattering of EM radiation by dust and gas between the galaxy and the observer. It is denoted by the $B-V$ color excess, being the difference of the observed and intrinsic $B-V$ color (calibrated blue minus calibrated visible). Galaxy counts in pixels that are affected by these data quality cuts are replaced by the average galaxy counts of the remaining unaffected neighboring pixels. This leads to the final sky map of the galaxy number count in `HEALPix`-based representation [119], with the systematic effects accounted for. This sky map is shown in equatorial coordinates in Figure 3.6. The pixels with information cover around 20% of the full sky.

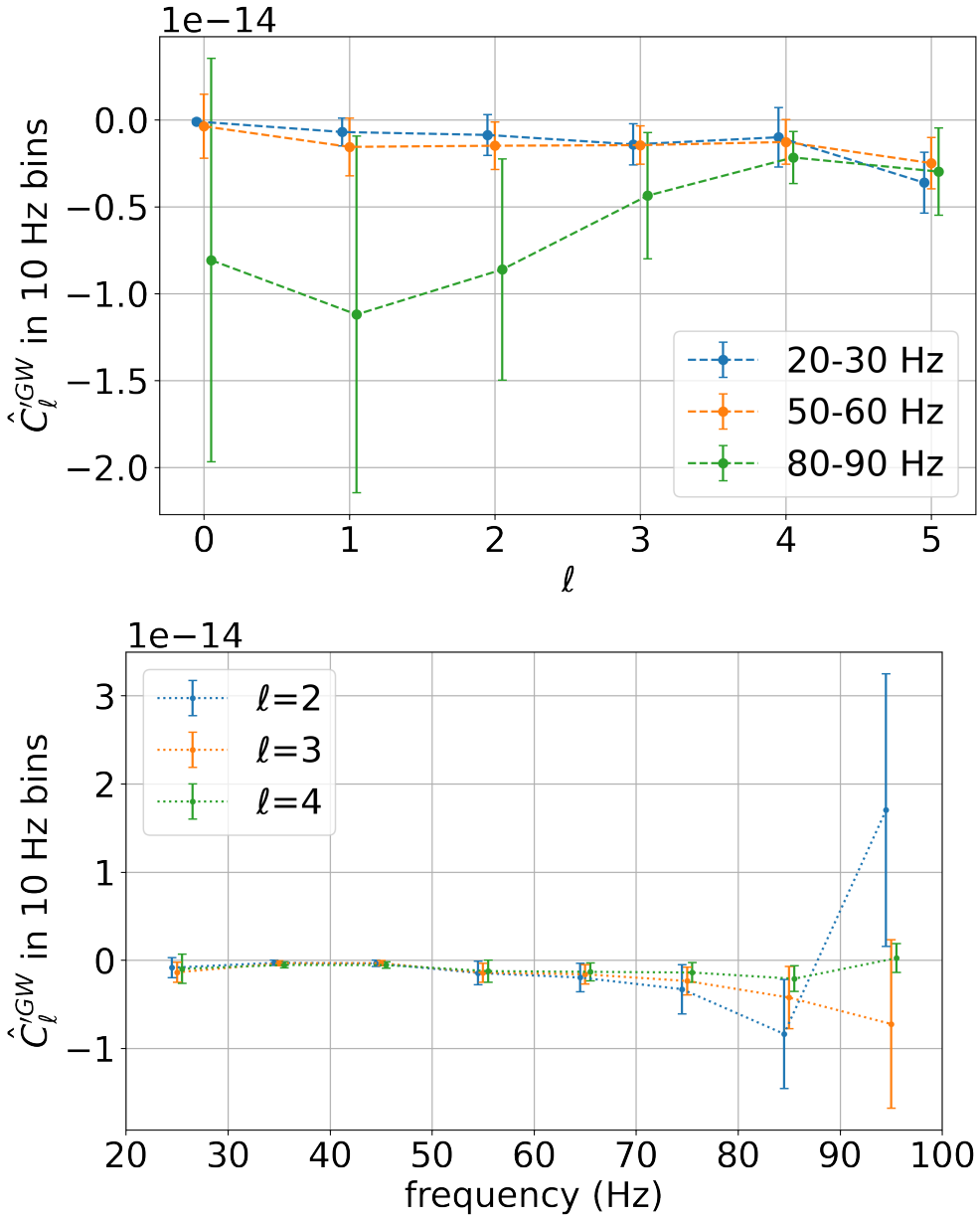

Figure 3.5: Unbiased $\hat{C}_\ell^{\prime GW}$ estimators with standard deviation error-bars of the SGWB angular power spectrum are shown in 10 Hz-wide frequency bands (20–30 Hz, 50–60 Hz, and 80–90 Hz) as a function of ℓ (top) and as a function of frequency for $\ell = 2, 3, 4$ (bottom).

Based on this galaxy count sky map, I then calculate the galaxy over-density as a function of the sky direction and expand it in spherical harmonics as defined in Eq. (3.10). To account for

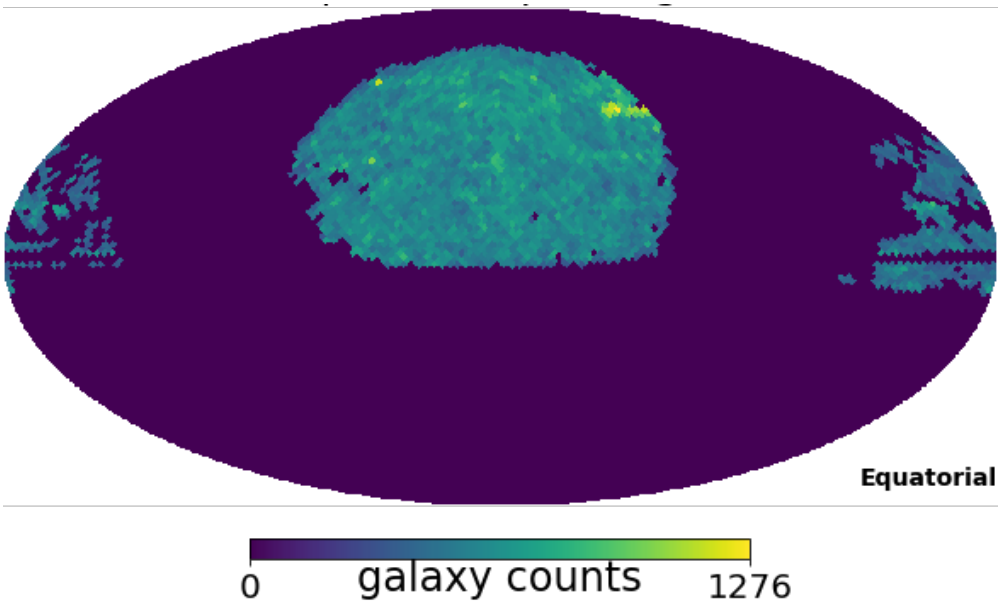

Figure 3.6: Galaxy number count sky map in equatorial coordinates from the SDSS spectroscopic catalog. I have selected galaxies with r-band magnitude between 17 to 21 after removing quasars and stars and applied a mask to correct for systematics. The color bar stands for galaxy count in each `HEALPix` basis pixel with resolution of $N_{\rm side}$=32.

the pixels with missing information, I apply a binary mask to the galaxy over-density sky map in pixel basis, where I mask out every pixel without information (due to no observations or high systematics), before applying the spherical harmonic transformation. The obtained spherical harmonic coefficient estimators, $\hat{b}_{\ell m}$'s, are then used to compute the angular power spectrum for the galaxy over-density auto-correlation:

$$\hat{C}_\ell^{\rm GC} = \frac{1}{f_{\rm sky}} \frac{1}{2\ell+1} \sum_{m=-l}^{l} |\hat{b}_{\ell m}|^2 \,, \tag{3.36}$$

where the factor $f_{\rm sky}$ is the fraction of the sky covered by the survey with valid information, and is needed to account for the missing power in the sky map when performing the spherical harmonic transformation. The same scaling must also be applied when computing the cross-correlation angular power spectrum between SGWB and GC partial sky maps. The resulting GC angular power spectrum of the SDSS spectroscopic catalog is shown in Figure 3.7, including uncertainties given by the cosmic variance. The maximum ℓ used in this Figure is determined

by the angular resolution in Figure 3.6 and is larger than the maximum ℓ obtained from the SGWB analysis above. Furthermore, due to the partial sky coverage, there is a lower limit on ℓ that can be estimated by the spot size in the sky θ (in radians) with the relation: $\ell_{\rm min} = \pi/\theta$. As we can see in Figure 3.6, SDSS spectroscopic catalog covers a part of the north Galactic Cap (NGC): $105° < \text{RA} < 260°$, $-5° < \text{DEC} < 70°$ and a part around the equator: $0° < \text{RA} < 50°$ and $320° < \text{RA} < 360°$, $-10° < \text{DEC} < 35°$, so I estimate $\theta \sim 45° = \pi/2$ rad, hence I choose $\ell_{\rm min} = 2$ for the SDSS spectroscopic catalog sky map (Figure 3.6) in Figure 3.7.

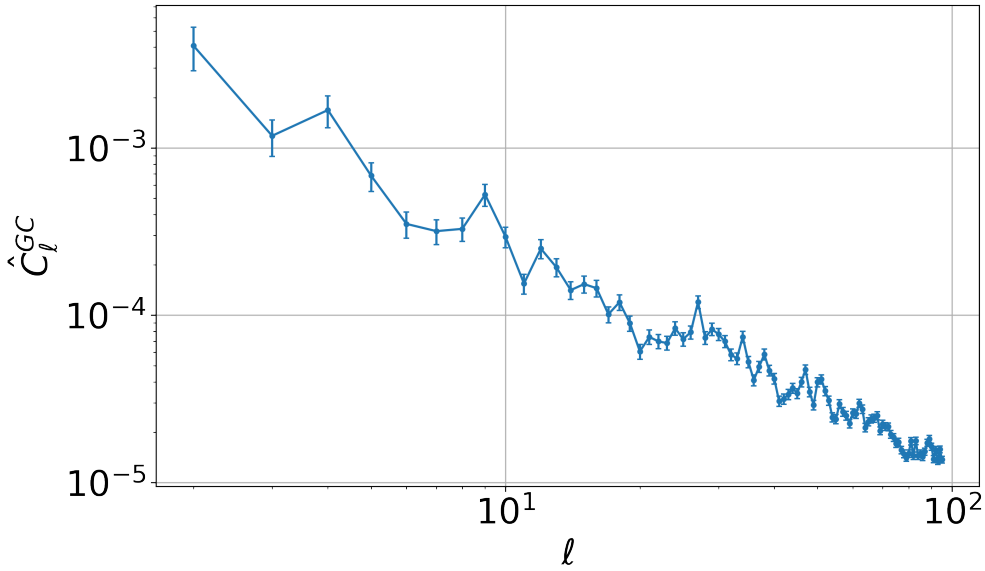

Figure 3.7: The angular power spectrum $\hat{C}_\ell^{\rm GC}$ for galaxy count over-density, corrected for the partial-sky coverage, from the SDSS spectroscopic catalog of $2 \leq \ell \leq 95$. Uncertainties associated with the cosmic variance are shown.

3.5 Measurement of Cross-correlation Angular Power Spectra

Following the work in the Sections 3.3 and 3.4, I now introduce an unbiased estimator for the angular power spectrum of the cross-correlation using the frequency-dependent SGWB multipoles $\hat{a}_{\ell m}(f)$ estimated in 10 Hz-wide frequency bands, introduced in Section 3.3.3, and the SDSS sky map multipoles $\hat{b}_{\ell m}$, introduced in Section 3.4. The estimator of their cross-correlation angular

power spectrum is defined as

$$\hat{C}_\ell^{\rm cross} = \frac{1}{f_{\rm sky}} \frac{1}{2\ell+1} \sum_{m=-\ell}^{\ell} \hat{b}^*_{\ell m}\, \hat{a}_{\ell m}\,. \tag{3.37}$$

As stated above, the $1/f_{\rm sky}$ factor accounts for the incomplete sky coverage of the SDSS spectroscopic catalog. To compute the covariance matrix K_C of this estimator, I assume that the galaxy map multipoles have much smaller uncertainties than their SGWB counterparts. This is a safe assumption since each pixel in the SDSS map in Figure 3.6 contains thousands of galaxies (implying uncertainties at the level of a few percent), while the SGWB sky map is dominated by detector noise and shows no evidence of a signal. Consequently, Eq. (3.37) can be regarded as a linear transformation of the SGWB multipoles $\hat{a}_{\ell m}$, implying that the resulting $\hat{C}_\ell^{\rm cross}$'s are also multi-variate Gaussian with the covariance matrix given by the propagation of the covariance matrix of the SGWB multipoles $K^{\rm GW}$:

$$(K_C)_{\ell,\ell'} = \frac{1}{f_{\rm sky}^2} \frac{1}{(2\ell+1)\,(2\ell'+1)} \sum_{m,m'} \hat{b}^*_{\ell m}\, K^{\rm GW}_{\ell m \ell' m'}\, \hat{b}_{\ell' m'}\,. \tag{3.38}$$

The angular power spectra of the cross-correlation between the measured SGWB sky-maps (in 10 Hz-wide frequency bands from 20 to 100 Hz) and galaxy over-density in the SDSS spectroscopic catalog are shown in Figure 3.8. Error bars shown in the figure are defined as the square root of the diagonal terms of the K_C matrix. Similar to the SGWB auto-correlation case in Section 3.3, there is no evidence for a cross-correlation signal. We can see from the figure that the noise level of cross-correlation $\hat{C}_\ell^{\rm cross}$ increases with frequency, similar to what we see in the SGWB auto-correlation in Figure 3.5. The above trends are reasonable, as there is no cross-correlation signal, and the covariance of $\hat{C}_\ell^{\rm cross}$ is given by the SGWB covariance in Eq. (3.38).

The covariance matrix K_C in Eq.(3.38) does not take into account the cosmic variance or the shot noise contributions discussed in Section 3.2.2 described by Eq. (3.17). Following [129, 151], these contributions are diagonal and should be added to the above covariance matrix,

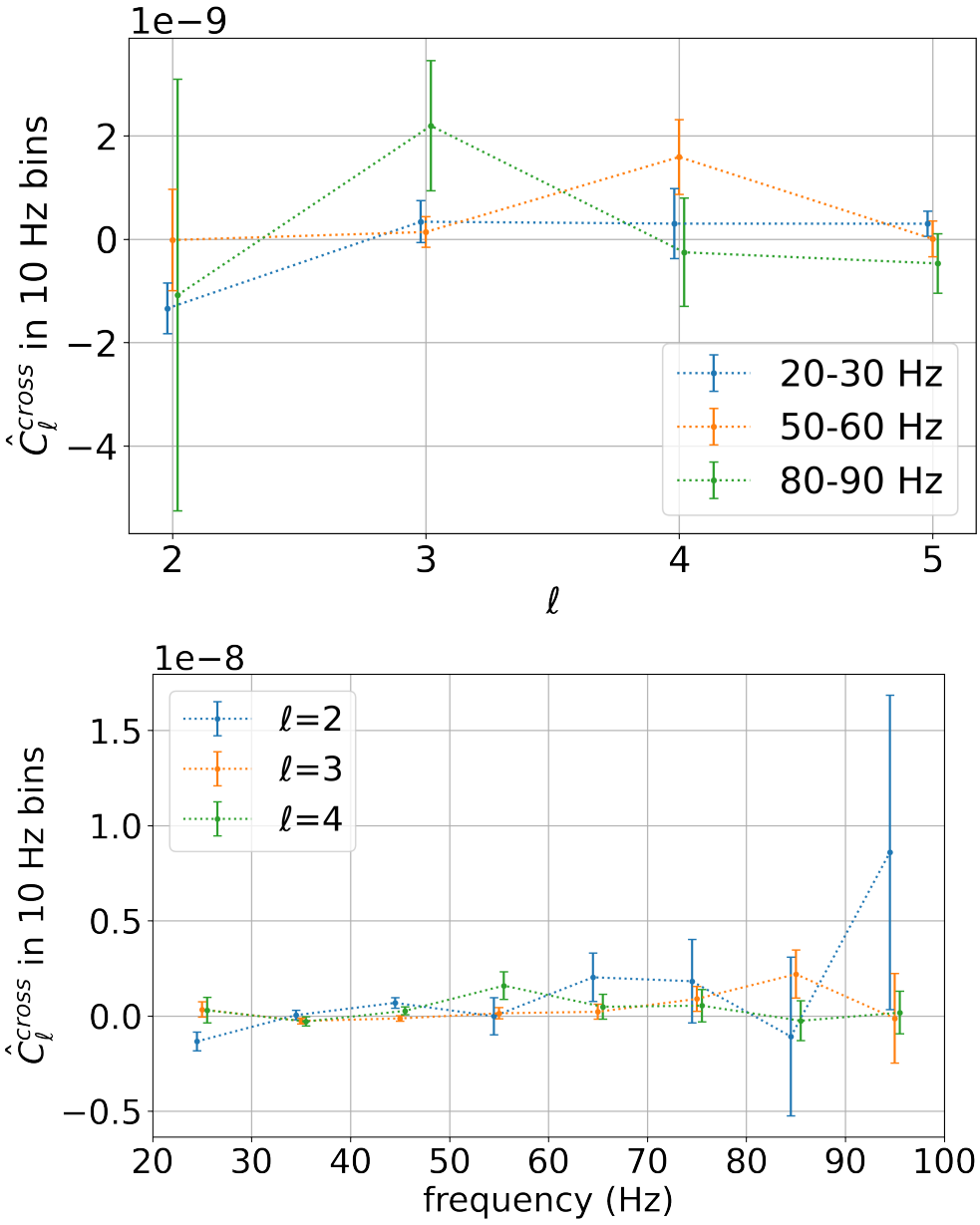

Figure 3.8: Angular power spectra $\hat{C}_\ell^{\rm cross}$ and standard deviation error-bars of the cross-correlation between the measured SGWB sky-maps (in 10 Hz-wide frequency bands) and the galaxy over-density of the SDSS spectroscopic catalog, with $\ell \geq 2$ up to $\ell_{\rm max} = 5$ are shown for several example frequency bands (top) and for several values of ℓ (bottom).

resulting in the final covariance matrix as

$$(K_C^{\rm tot})_{\ell\ell'} = (K_C)_{\ell\ell'} + \frac{\delta_{\ell\ell'}}{(2\ell+1)}\left[\left(C_\ell^{\rm GW}(\theta) + N_{\rm shot}^{\rm GW}(\theta)\right)\left(C_\ell^{\rm GC} + N_{\rm shot}^{\rm GC}\right) + \left(C_\ell^{\rm cross}(\theta) + N_{\rm shot}^{\rm cross}(\theta)\right)^2\right]. \tag{3.39}$$

Note that the shot noise is Poissonian in origin, so it can compromise the multi-variate Gaussian nature of the $\hat{C}_\ell^{\rm cross}$ estimators. In the limit when the cross-correlated signal is small, the shot noise contribution to the covariance matrix will be relatively small compared to the SGWB instrumental noise contribution, and the distribution will be approximately Gaussian. I will follow this criteria in the following work of this chapter. It is important to note that as the SGWB instrumental noise improves and the cross-correlated signal becomes more significant, the shot noise contribution will shift the $\hat{C}_\ell^{\rm cross}$ distribution away from Gaussian behavior. The parameter estimation scheme presented below will have to be correspondingly adapted.

3.6 Parameter Estimation

Now that I have measured the angular power spectra $\hat{C}_\ell^{\rm cross}$ of the cross-correlation between the SGWB and the galaxy over-density sky-maps of the SDSS spectroscopic catalog, we can try to extract the astrophysical information from these measurements. Here a Bayesian inference framework is used, and the posterior distribution of the astrophysical model parameters θ is given by

$$p(\theta\,|\,\hat{C}_\ell^{\rm cross}) \propto \mathcal{L}(\hat{C}_\ell^{\rm cross}\,|\,C_\ell^{\rm cross}(\theta))\,\pi(\theta)\,, \tag{3.40}$$

where $\pi(\theta)$ is the prior distribution of the model parameters and $\mathcal{L}$ is the likelihood of observing the data with certain model parameters. As discussed above, in the limit when the cross-correlation signal is small, the $\hat{C}_\ell^{\rm cross}$'s will approximately follow the multivariate Gaussian distribution with the covariance matrix given by either K_C if shot noise is ignored or by $K_C^{\rm tot}$ if shot noise is included. In particular, when shot noise is ignored, the log-likelihood of the measurement $\hat{C}_\ell$ under the model $C_\ell(\theta)$ specified by parameters θ is

$$\ln\mathcal{L}(\hat{C}_\ell|C_\ell(\theta)) = \frac{1}{2}\ln\left|K_C\right| - \frac{1}{2}(\hat{C}_\ell - C_\ell(\theta))^T\,K_C^{-1}\,(\hat{C}_\ell - C_\ell(\theta))\,. \tag{3.41}$$

Here I omit the superscript 'cross' for simplicity. If we are including shot noise in this analysis, $C_\ell(\theta)$ is replaced by $C_\ell^{\rm tot}(\theta)$ as in Eq. (3.16) and K_C is replaced by $K_C^{\rm tot}$ as in Eq. (3.39). This likelihood depends on the frequency of SGWB as it can be computed for the SGWB maps in all the 10 Hz-wide frequency bands. The overall likelihood is obtained by multiplying the likelihoods across individual frequency bands; equivalently, it is computed by summing the corresponding log-likelihoods. Finally, since K_C is independent of model parameters, the first term involving $|K_C|$ can be omitted. This simplification does not apply when including shot noise, where $K_C^{\rm tot}$ is used instead, as it depends on model parameters through the shot noise terms in Eq. (3.39).

The astrophysical model I am using that describes the galactic process of GW emission and the shot noise effects in Section 3.2 is parameterized by an astrophysical Gaussian kernel which depends on three parameters $\theta = (A_{\rm max}, z_c, \sigma_z)$ and peaks at around $z = 1$ (see Figure 3.2). As the SDSS spectroscopic galaxy catalog extends only up to $z \lesssim 0.8$, this analysis will not be able to assess the Gaussian peak. Instead, at small redshift, the kernel can be approximated by a linear function that monotonically increases with redshift [98]. Therefore, the two parameters z_c and σ_z are degenerate, as increasing the mean z_c or decreasing the variance σ_z both increase the slope (> 0) of the linear function. Under this circumstance, I choose to fix $\sigma_z = 0.7$, which is a reasonable value that fits the astrophysical models in [98]. Then the parameter space becomes 2-dimensional: $\theta = (A_{\rm max}, z_c)$.

Then I scan the parameter space and compute the posterior distribution of Eq. (3.40) using the measured $\hat{C}_\ell^{\rm cross}$ obtained in Section 3.5, with or without the inclusion of shot noise. These analyses will yield upper limits on the astrophysical kernel parameters θ. To show that this formalism correctly recovers the kernel parameters, and to study how the inclusion of shot noise impacts the recovery, I also try to recover simulated signals ($C_\ell^{\rm cross}(\theta)$'s) with fixed parameters θ that are injected into the measured $\hat{C}_\ell^{\rm cross}$ by scanning the parameter space and computing the posterior distribution.

3.6.1 Results Without Shot Noise

As the first step, I calculate the posterior distribution using the likelihood of Eq. (3.41), ignoring the shot noise contribution (in both the signal and in the covariance matrix) and without adding any simulated signals. I compute the log-likelihood in every 10 Hz-wide frequency band from

20 to 100 Hz, then sum them up to obtain the overall likelihood, assuming uniform prior distributions in the two parameters: $A_{\rm max} \in [1 \times 10^{-38}, 5 \times 10^{-32}]\,{\rm erg\,cm^{-3}\,s^{-1/3}}$ and $z_c \in [0, 1]$ [98]. Both ranges both are well motivated in astrophysics as stated in Section 3.2.1, and both are consistent with the sensitivity of my $\hat{C}_\ell^{\rm cross}$ measurements. I use a uniform linear grid in the above parameter space, then evaluate the model C_ℓ's, the likelihood, and the posterior at each grid point. The result for the overall 20–100 Hz frequency band is shown in the upper-left panel of Figure 3.9. While there is a slight preference for larger values of z_c, no constraint can be placed on this parameter. However, a 95% confidence upper limit on $A_{\rm max}$ can be placed on $A_{\rm max}^{95\%} = 2.9 \times 10^{-32}\,{\rm erg\,cm^{-3}\,s^{-1/3}}$.

Next, I add a simulated signal of $A_{\rm max} = 2.5 \times 10^{-32}\,{\rm erg\,cm^{-3}\,s^{-1/3}}$ and $z_c = 0.6$ to the measured $\hat{C}_\ell^{\rm cross}$'s, then evaluate the posterior distribution with the linear grid adjusted to be around these simulated values. The recovery result for the overall 20–100 Hz band is shown in the lower-left panel of Figure 3.9. From this figure we can see that the simulated parameter point is well within the recovered 2-dimensional 68% and 95% contours, and the one-dimensional distributions include the simulated values within 95% confidence, even though the z_c posterior is not very informative. Therefore we can conclude that this recovery of the simulated signal is successful without the inclusion of shot noise.

3.6.2 Results With Shot Noise

As stated in the above text under Eq. (3.40) as well as in Section 3.2.2, if we are to include shot noise, two modifications need to be applied. First, an offset is added to the angular power spectrum, as in Eq. (3.16). This offset is independent of ℓ, but it is dependent on the astrophysical model parameters θ. Second, an offset is added to the diagonal elements of the covariance matrix, as in Eq. (3.39). This offset is also dependent on astrophysical parameters θ. As a result of these two modifications, inclusion of shot noise complicates the recovery of clustering anisotropy; however, it may enhance the accuracy for estimation of astrophysical parameters.

Similar to the no-shot-noise case, I first start by computing the posterior distribution in Eq. (3.40) with the measured $\hat{C}_\ell^{\rm cross}$, model $C_\ell^{\rm cross,\,tot}(\theta)$ and covariance matrix $K_C^{\rm tot}$ in Eq. (3.41). The results are shown in the upper-right panel of Figure 3.9. Again, there is no evidence of signal, even though there is a small (statistically insignificant) preference for higher values of $A_{\rm max}$. While the z_c posterior is again not informative, we can place a 95% confidence upper limit on $A_{\rm max}$: $A_{\rm max}^{95\%} = 2.5 \times 10^{-32}\,{\rm erg\,cm^{-3}\,s^{-1/3}}$. Note that this upper limit is stronger than

in the no-shot-noise case, indicating that addition of shot noise improves the sensitivity of this analysis to $A_{\rm max}$. The Bayes factor between the model without shot noise and the model with shot noise is 0.475, preferring the inclusion of shot noise.

Next, I include a simulated signal. In order to keep the shot noise contribution small so as to maintain the approximate multi-variate Gaussian distribution of $\hat{C}_\ell^{\rm cross}$'s, I choose a smaller value of $A_{\rm max} = 1.0 \times 10^{-32}\,{\rm erg\,cm^{-3}\,s^{-1/3}}$ for this simulation; and keep the peak redshift the same as in the no-shot-noise case, $z_c = 0.6$. The results of recovery are shown in the lower-right panel of Figure 3.9. While $A_{\rm max}$ is not fully resolved at 95% significance, the $A_{\rm max}$ posterior distribution peaks at $9.5{\times}10^{-33}\,{\rm erg\,cm^{-3}\,s^{-1/3}}$, which is consistent with the simulated amplitude. The z_c posterior is still not informative, but it still indicates a slight preference for larger values of z_c, consistent with the simulated value of 0.6. Note that the simulated value of $A_{\rm max}$ is below the 95% upper limit on $A_{\rm max}$ from the no-shot-noise case, indicating that it would not be observable in the no-shot-noise analysis, but is successfully recovered with shot noise. This is another indication that the inclusion of shot noise in the analysis improves the sensitivity to $A_{\rm max}$. The Bayes factor between the model without shot noise and with shot noise when I add the same signal of $A_{\rm max} = 1 \times 10^{-32}{\rm erg\,cm^{-3}\,s^{-1/3}}$ is 0.428, preferring the inclusion of shot noise.

3.6.3 Parameter Estimation in 10 Hz Frequency Bands

The parameter estimation results in each 10 Hz-wide frequency band from 20 to 100 Hz (labeled by their center frequency) are shown in the following figures: Upper limits of parameters without and with shot noise effects (Figure 3.10 and 3.12, respectively); injection recovery without and with shot noise effects (Figure 3.11 and 3.13, respectively). For Figure 3.11, I choose a simulated signal with $A_{\rm max} = 2.5 \times 10^{-32}\,{\rm erg\,cm^{-3}\,s^{-1/3}}$ and $z_c = 0.6$. For Figure 3.13, I choose a simulated signal with $A_{\rm max} = 1 \times 10^{-32}\,{\rm erg\,cm^{-3}\,s^{-1/3}}$ and $z_c = 0.6$. While the recovered contours are still consistent with the simulated parameter values, the contours are rather large due to the small value of the simulated $A_{\rm max}$. Combining all frequency bands gives a much stronger estimate of $A_{\rm max}$ as shown in the lower-right panel of FIG 3.9.

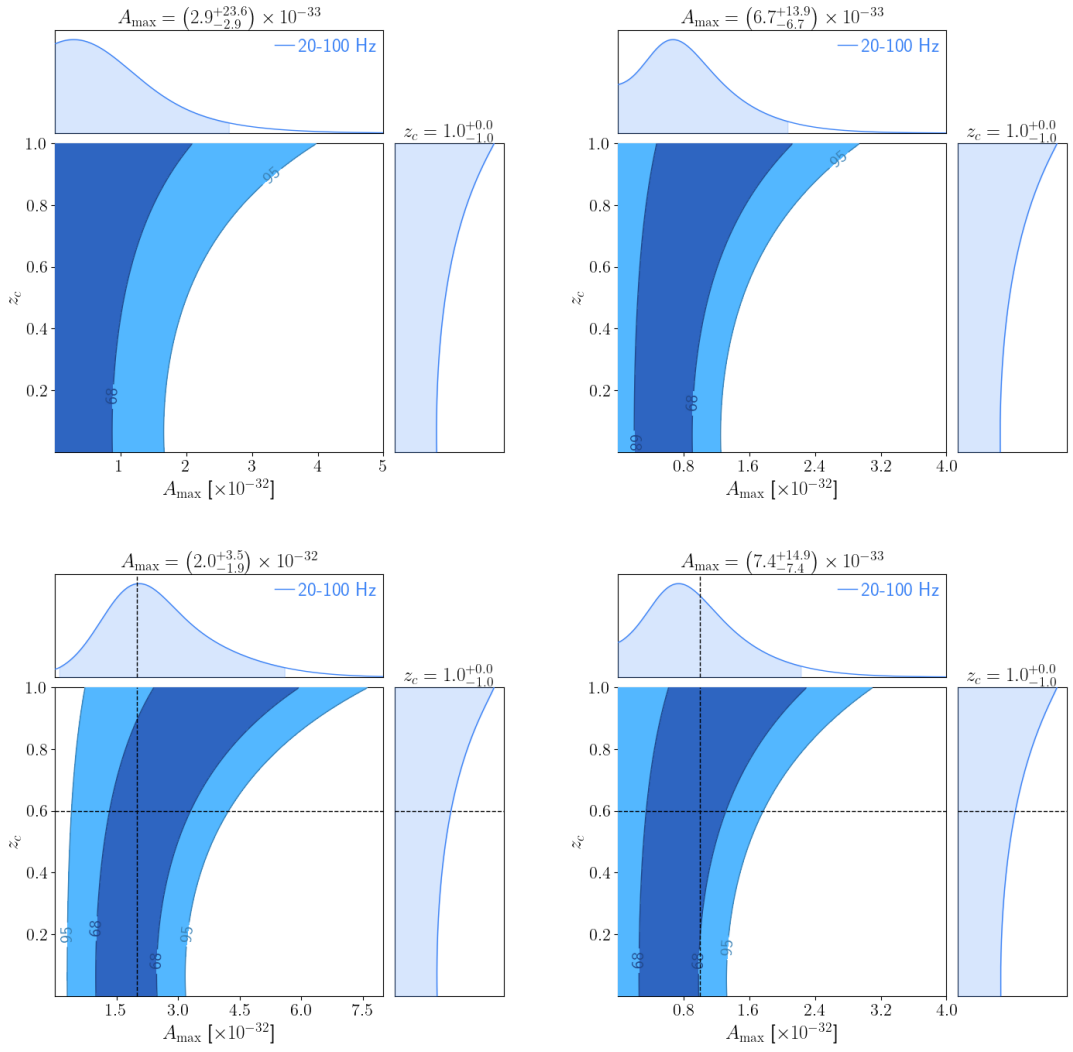

Figure 3.9: Results of the parameter estimation for the cross-correlation between the SGWB (20 to 100 Hz) and the galaxy over-density from the SDSS spectroscopic catalog plotted using *ChainConsumer* [152]. Each panel shows 2-dimensional posterior with 65% and 95% confidence contours, as well as 1-dimensional marginalized posteriors with 95% confidence intervals for the two model parameters: $A_{\rm max}$ in units of erg cm^{-3} s$^{-1/3}$ and z_c. Left column panels correspond to the no-shot-noise case, while the right column panels include the shot noise. The upper row panels present upper limits on model parameters (no simulated signal is added). The lower panels show recoveries when a simulated signal is added to the data. The dashed lines indicate the values of simulated parameters. See text for further details.

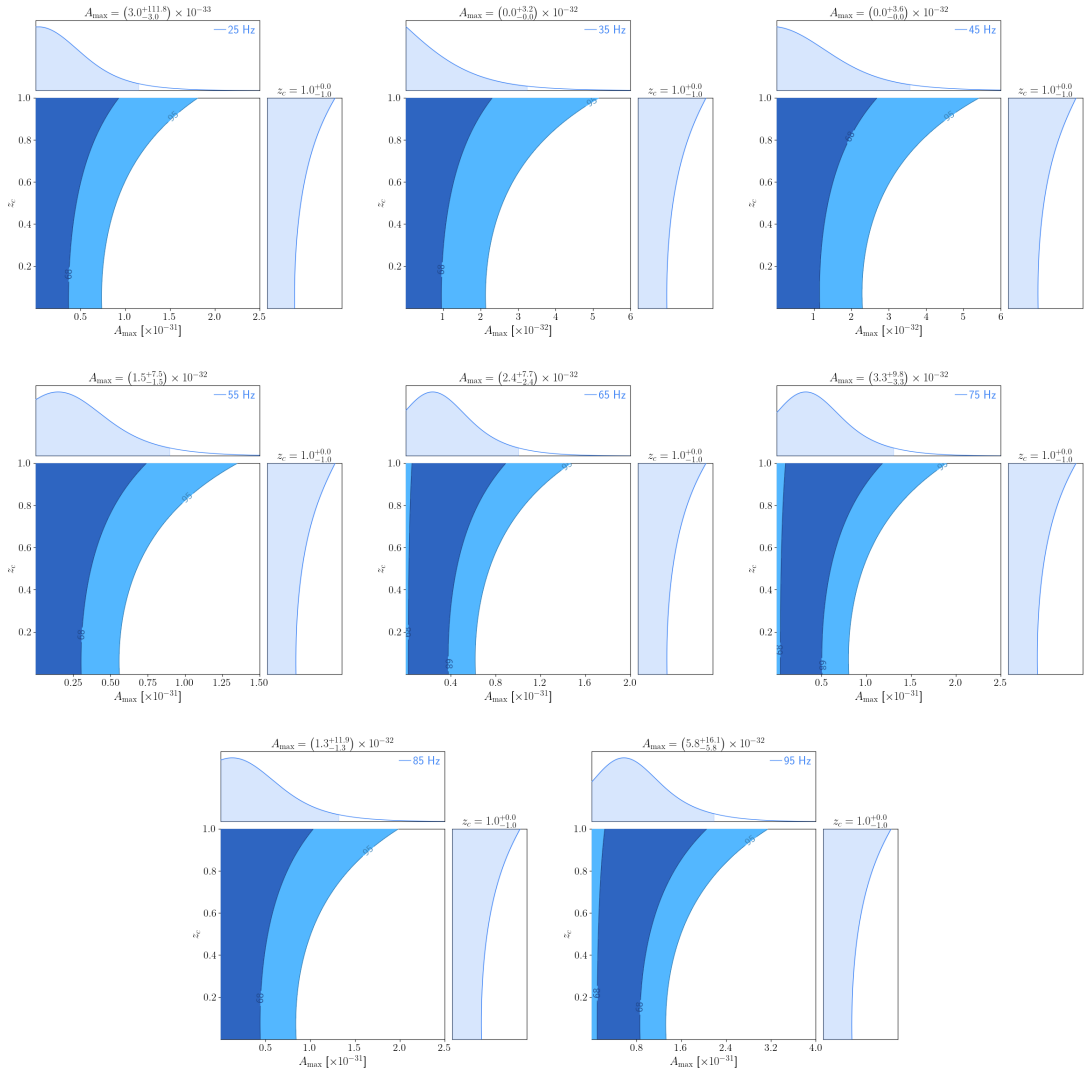

Figure 3.10: Upper limits of parameters $A_{\max}$ in units of erg cm^{-3} s$^{-1/3}$ and z_c for SGWB measured in different frequency bands, without including the shot noise.

3.7 Conclusion and Discussion

In this chapter, I studied the cross-correlation between the SGWB measured in LIGO O3 and the galaxy distribution across the sky measured by SDSS spectroscopic survey, and I measured the angular power spectra of the cross-correlation in different SGWB frequency bands. These analyses are based on the assumption that SGWB in the 20–100 Hz frequency band is dominated

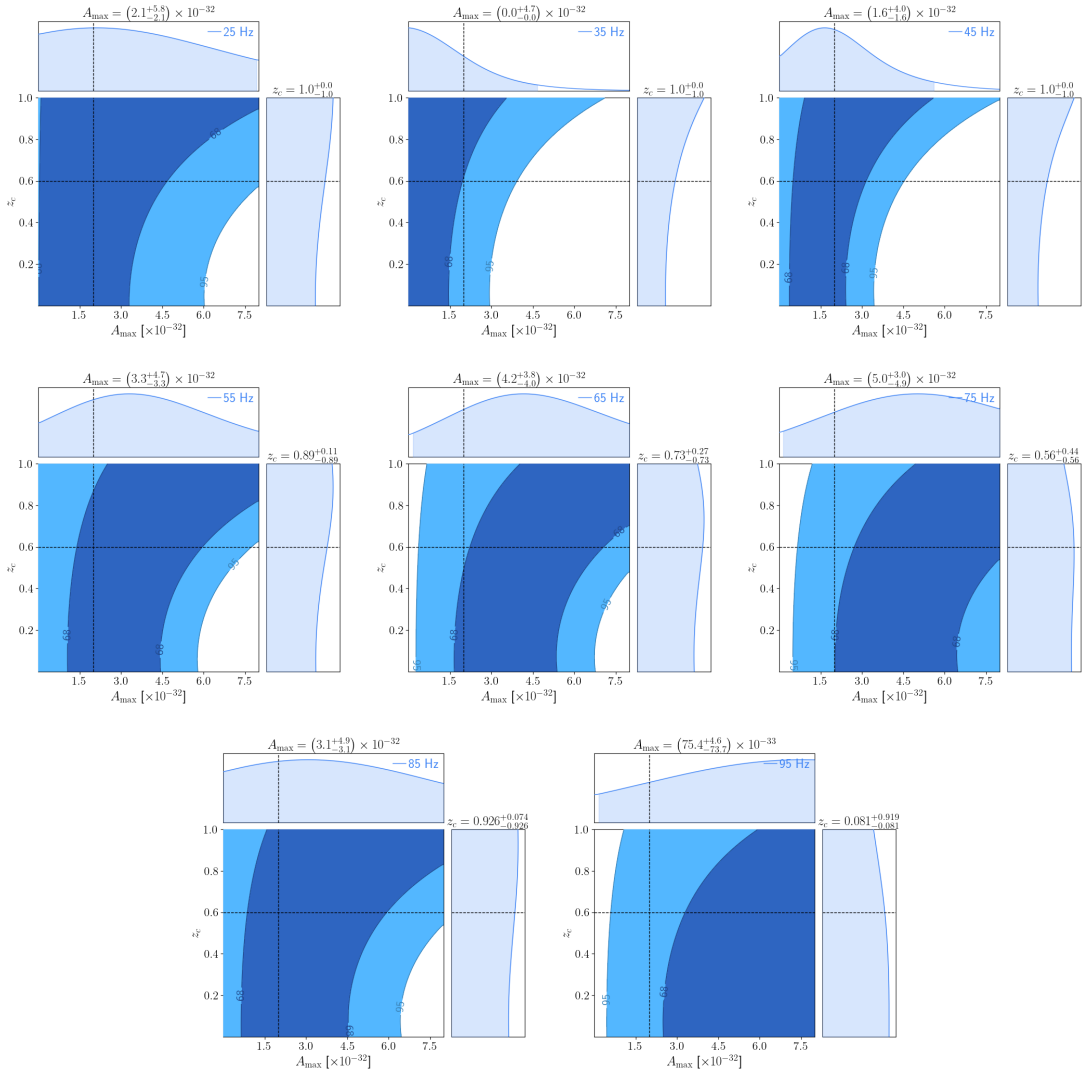

Figure 3.11: Recovery of a simulated signal with parameters $A_{\rm max} = 2.5 \times 10^{-32}$ erg cm^{-3} s$^{-1/3}$ and $z_c = 0.6$, using SGWB measured in different frequency bands and without including shot noise.

by extragalactic sources of compact mergers. As we do not have a detection yet, the resulting cross-correlation angular power spectra are dominated by instrumental noise. However, the spectra can be compared with predictions from an astrophysical model of the SGWB due to BBH mergers, helping to set upper limits on model parameters. For this astrophysical model, I assumed that the GW emission is well-captured by the quadrupole formula, so the frequency

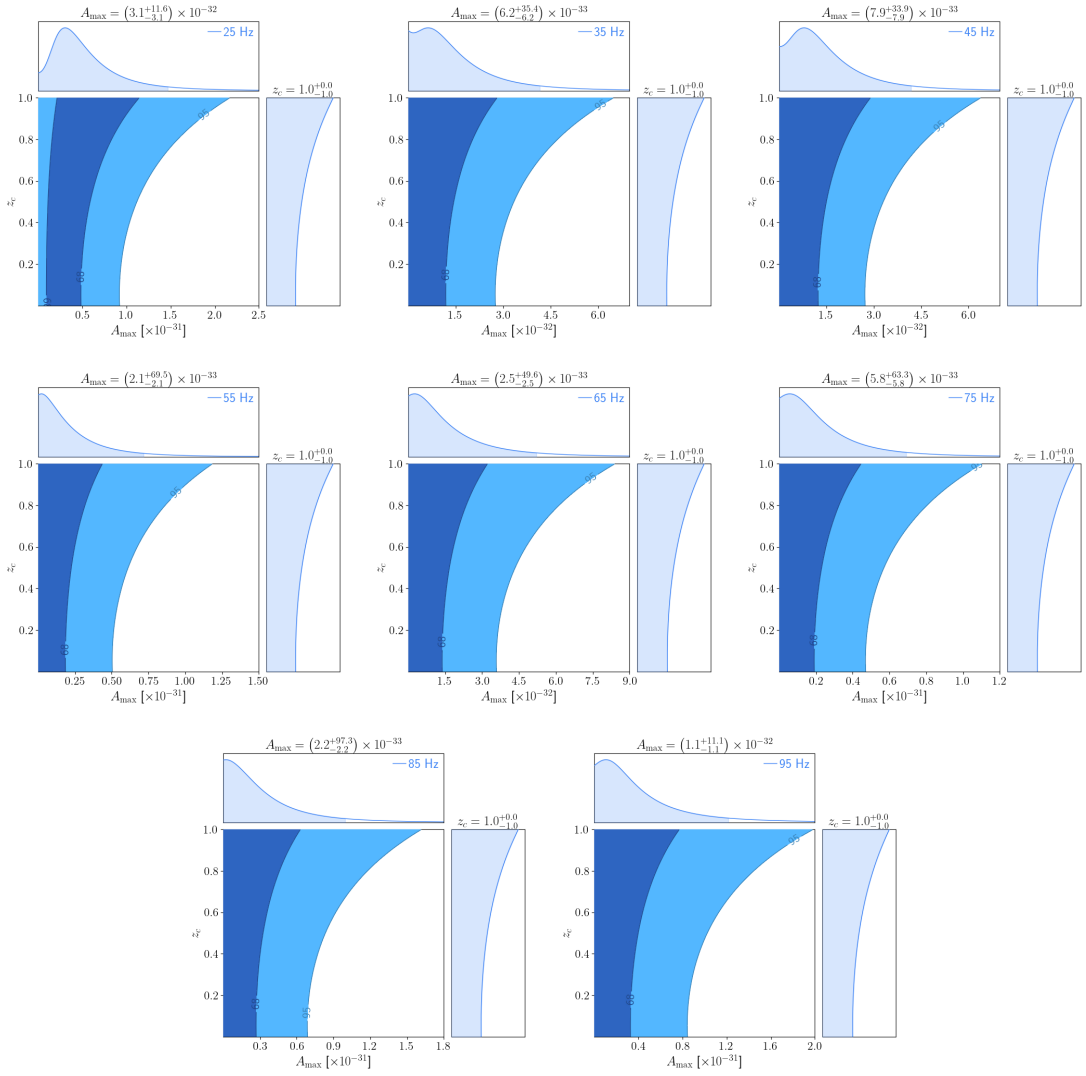

Figure 3.12: Upper limits on parameters $A_{\max}$ in units of erg cm^{-3} s$^{-1/3}$ and z_c for SGWB measured in different frequency bands, including the shot noise.

dependence can be factorized out (Eq. 3.4, 2.2-2.3). So I used a simplified parameterization for the redshift-dependent astrophysical kernel characterizing GW emission at galactic scales in terms of a global amplitude and a peak position, corresponding to the redshift range that contributes the most to the total SGWB. I searched this 2D parameter space in a Bayesian inference framework and found an upper bound for the amplitude of the kernel to be $A_{\max}$ =

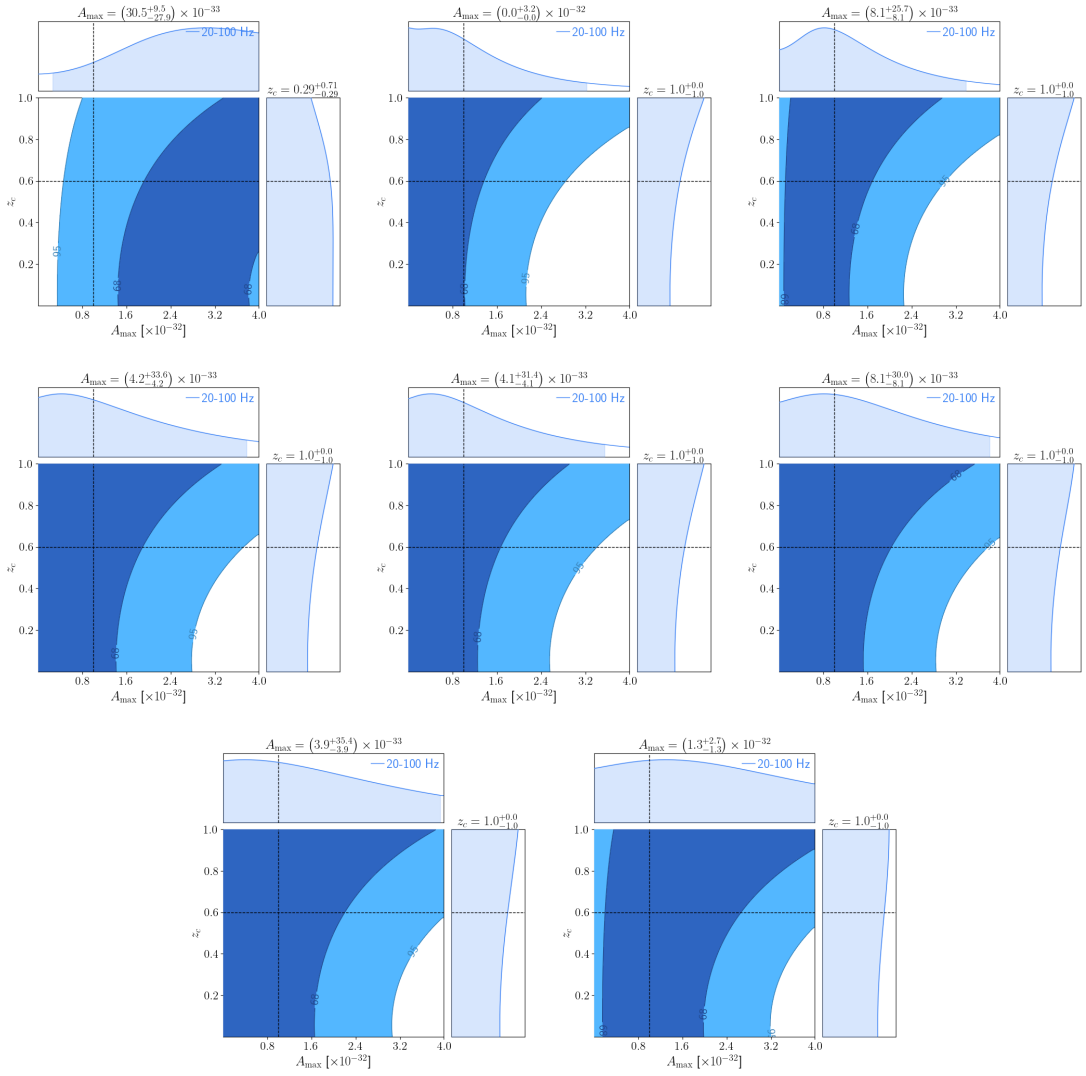

Figure 3.13: Recovery of a simulated signal with parameters $A_{\rm max} = 1 \times 10^{-32}\,{\rm erg\,cm^{-3}\,s^{-1/3}}$ and $z_c = 0.6$, using SGWB measured in 10 Hz-wide frequency bands and including shot noise.

$2.5 \times 10^{-32}\,{\rm erg\,cm^{-3}\,s^{-1/3}}$ while the peak redshift is not well constrained. My results showed that including shot noise reduces the ability to recover clustering contributions to the anisotropy but improves sensitivity to the astrophysical kernel parameters. I validate the reliability of my analysis method through injection-recovery tests. The Bayes factor comparing the model without shot noise and the model with shot noise is less than 1, demonstrating a preference for

including shot noise.

In this chapter, I did not bin galaxies by redshift as in Chapter 2; instead, I considered all galaxies with all redshifts combined. This will be an interesting step forward: applying this analysis with galaxies in redshift bins to study the redshift dependence of the constraints on the astrophysical model parameters. However, doing so requires extra attention, especially with galaxy catalogs that observe deep in the Universe. In this chapter I used the SDSS spectroscopic catalog, which only observes $0 < z < 0.8$; within this range, the anisotropy of SGWB is dominated by contributions of low redshift sources (i.e. $z < 0.1$). Then the cross-correlation of it with galaxies is dominated by clustering (or the galaxy over-density term). But when considering the cross-correlation of SGWB and galaxy distribution in a redshift slice around higher values such as $z = 2$, the line of sight effect (the κ term in Eq. (13) of [153], or see [70] for details and derivations) dominates. In this chapter, I integrated the SDSS spectroscopic catalog over redshift, hence it is safe to only consider clustering.

Another interesting step forward is to cross-correlate SGWB with other EM tracers of structure in the Universe, i.e., weak lensing, Cosmic Microwave Background, Cosmic Infrared Background, etc. Furthermore, one may develop a joint analysis of all these cross-correlations. This may improve the overall sensitivity of this approach and help distinguish different (i.e. stellar or primordial) contributions to the CBC SGWB model.

It is also interesting to test this cross-correlation analysis using realistic simulations of the GW emissions over the sky by simulating the galaxy distribution and GW emission on galactic scales. This can help study different CBC contributions to the SGWB. I am performing this simulation analysis in the next chapter 4.

We expect the sensitivity of the GW detector network to keep improving in the future, which will improve the constraints on the astrophysical model parameters. Advanced LIGO, Advanced Virgo, and KAGRA are currently performing the fourth observation run, and the first eight months of data are released now. With improved detector sensitivity, extended observation time, and availability of multiple detector pairs, the sensitivity to $\hat{C}_\ell^{\rm GW}$ is improved by 100 times compared to O3, equivalently improving $\hat{C}_\ell^{\rm cross}$ by 10 times. The next generation of ground based detectors, such as Einstein Telescope [154] and Cosmic Explorer [155] will enable another $\sim$ 1000 times improvement in sensitivity of the strain. As stated in Section 2.5 in Chapter 2, one can also use the Bayesian Search to estimate the CBC SGWB anisotropy [126], which could also lead to $\sim$ 1000 times sensitivity improvements compared to the approach in

this chapter. These improvements are expected to probe the astrophysically relevant region of the parameter space.

Finally, a big limit to this analysis comes from the process of regularizing the Fisher matrix in order to invert it (Section 3.3.1). This process introduces a bias which must be constrained by only expanding spherical harmonics to a low degree ($\ell_{\rm max} = 5$). With the improvement of the sensitivity of LVK detectors and with more baseline pairs joining the observation, there will be fewer blind spots on the sky and the Fisher matrix will be better defined with fewer low eigenvalues. It is also acceptable to conduct this analysis using the SGWB *"dirty map"* instead of *"clean map"*. Then one needs to convert the astrophysical model into the "dirty space" and set up a new likelihood function for it.

Chapter 4

Predicting Observed Gravitational Wave Energy Density of Compact Binary Mergers from galaxies in the *Euclid* Simulation

4.1 Introduction

In this chapter, I switch from LIGO data and observed galaxy distribution from SDSS to the *Euclid* Flagship Galaxy Mock Catalogue (version 2.1.10) [156] (hereafter, the *Euclid* catalogue) and predict GW energy density from it. This study provides a comparison with traditional analytic or semi-analytic models and helps with the preparation for the arrival of *Euclid* data. The *Euclid* catalogue simulates a smaller region (1/8) of the sky but deeper in redshift ($z \sim 3$) and contains much more (4.8 billion) galaxies as compared to SDSS, which covers 1/3 of the sky and extends to $z \sim 1$ with 2.6 million galaxies in its spectroscopic catalog [115].

There is a published method of predicting GW energy density of compact binary mergers from galaxies in a catalog [91] with information about redshift, metallicity, star-formation history, etc. As the *Euclid* catalogue does not include simulation of star-formation history, I set up a model for it that is driven by the current stellar mass and star-formation rate of the galaxy,

both of which are provided in the *Euclid* simulation. Then for each individual galaxy in the *Euclid* catalogue, I compute the prediction of GW energy density using the inferred local merger rate, mass and spin distributions with gravitational waves through GWTC-3 [157]. Based on this distribution of GW energy density, I obtain the anisotropy of the GW background. Finally, following the formalism in Chapter 3, I compute the angular power spectra of the SGWB anisotropy and its cross-correlation with the galaxy distribution in the *Euclid* simulation.

I also compared the cross-correlation angular power spectrum to the ones predicted by the astrophysical models parameterization in Section 3.2, then performed parameter estimation to constrain the model parameters that are consistent with the predictions derived from the catalog. This approach helps to determine which class of semi-analytic models and parameters best describes the prediction using the *Euclid* catalogue.

This chapter is structured as follows. In Section 4.2 I present the method in [91] of populating a galaxy catalog with compact binary mergers and predicting the corresponding SGWB spectrum. In Section 4.3 I present the properties of the *Euclid* catalogue. In Section 4.4 I present the prediction of SGWB angular power spectra and the parameter estimation result. Finally I conclude in Section 4.5.

4.2 Predicting GW Background from CBCs Using Galaxy Catalog

In this section I present the method of predicting the GW background energy density due to GW emissions by compact binary coalescences located in each galaxy in a catalog. Recall our definition of the SGWB intensity dimensionless density parameter $\Omega_{\rm GW}(\mathbf{e}, f)$ in Eq. (3.1). With the catalog approach in Section IV of [91], it is calculated as a summation of contributions from each galaxy:

$$\Omega_{\rm gw} = \sum_k w_k \, \delta^{(2)}(\hat{\mathbf{e}}_{\rm o}, \hat{\mathbf{e}}_k) \,, \tag{4.1}$$

where $k \in \{1, 2, ..., \mathcal{N}\}$ indexes a sum over the galaxies in the catalog of a 2-dimensional Dirac delta of the sky direction $\mathbf{e}$. The contribution from each galaxy is given by

$$w_k(f_{\rm o}) \equiv \sum_i \frac{\pi H_0}{3} (t_H f_{\rm o})^3 \, \frac{1+z_k}{r^2(z_k)} \, (1 + \hat{\mathbf{e}}_k \cdot v_{\rm o}) \int \mathrm{d}\zeta_{\rm b} \, R_i(z_k, \mathcal{Z}_k, \zeta_{\rm b}) \, \mathcal{S}_i(f_{{\rm s},k}, \zeta_{\rm b}) \,. \tag{4.2}$$

where $t_H \equiv 1/H_0$ is the Hubble time, R_i is the merger rate and $\mathcal{S}_i$ the source function, which will be discussed below. The index $i \in \{\text{BNS, BBH, BHNS}\}$ denotes different types of binary mergers with parameter $\zeta_\text{b} = (m1, m2, \chi_1, \chi_2)$ being the masses and spins of components of the binary system. Each galaxy k is described by its redshift z_k, comoving distance $r(z_k)$, sky location $\hat{\mathbf{e}}_k$, and log-normalized metallicity $\mathcal{Z}_k$ defined relative to the Solar metallicity $Z_\odot$ as

$$\mathcal{Z} \equiv \log_{10} \frac{Z}{Z_\odot} \,. \tag{4.3}$$

The source-frame GW frequency is related to the observed frequency by the redshift of the source:

$$f_{\text{s},k} = f_\text{o}\,(1+z_k)\left[1 + \hat{\mathbf{e}}_\text{o}\cdot(v_\text{g} - v_\text{o})/c\right]. \tag{4.4}$$

where v_k is the galaxy peculiar velocity along the line of sight. As the observer is considered to be static ($v_\text{o} = 0$), the v_k/c term is negligible as compared to 1 for high redshift galaxies.

The source function $\mathcal{S}_i$ defines the GW energy spectrum emitted by a binary merger. It depends on the source frame frequency $f_{\text{s},k}$ and the binaries parameters ζ_b. For BBH, it is given by

$$\mathcal{S}_\text{BBH} \equiv \int_{S^2} \mathrm{d}^2\mathbf{e}_\text{s}\, r_\text{s}^2 \tilde{h}^2_\text{BBH} = \frac{5(G\mathcal{M})^{5/3}}{6\pi^{1/3}} \times \begin{cases} f_\text{s}^{-7/3}\left[1 + \sum_{i=2}^{3}\alpha_i\,(\pi G M f_\text{s})^{i/3}\right]^2, & f_\text{s} < f_1 \\ c_1\, f_\text{s}^{-4/3}\left[1 + \sum_{i=1}^{2}\epsilon_i\,(\pi G M f_\text{s})^{i/3}\right]^2, & f_1 \le f_\text{s} < f_2 \\ c_2\left[1 + \left(\frac{f_\text{s}-f_2}{f_3}\right)\right]^2, & f_2 \le f_\text{s} < f_4 \end{cases} . \tag{4.5}$$

The definitions of $c_{1,2}, \alpha_i, \epsilon_i$ and $f_{1,2,3,4}$ can be found in [91, 158] and are dependent on the masses and spins of the binaries. Here, G is the Newton's gravitational constant, M is the total mass of the binary and $\mathcal{M}$ is the chirp mass of the binary. For BNS and BHNS systems, only $f_\text{s} < f_1$ terms will be kept and contributions from higher frequencies will be ignored. Note that an optimized inclination angle of the binary's total angular momentum with the line of sight from the observer is assumed in this calculation.

The merger rate of binary merger with type i in galaxy k depends on the galaxy's redshift, metallicity and the binary merger parameters:

$$R_i(z_k, \mathcal{Z}_k, \zeta_\text{b}) = \frac{\mathcal{R}_i^{(\text{local})}}{\mathcal{I}_i}\, p_i(\zeta_\text{b})\, f_\mathcal{Z}\, \psi_{\text{d},i}(z_k)\,, \tag{4.6}$$

and is normalized to the local merger rate $\mathcal{R}_i^{(\rm local)}$ observed by GW ground-based detectors. Here I use the fiducial merger rates at $z = 0$ in [157] for different types of binary mergers:

$$\mathcal{R}_{\rm BBH}^{(\rm local)} = 23.9^{-8.6}_{+14.9}\,{\rm Gpc^{-3}\,yr^{-1}},\ \mathcal{R}_{\rm BNS}^{(\rm local)} = 105.5^{-83.9}_{+190.2}\,{\rm Gpc^{-3}\,yr^{-1}},\ \mathcal{R}_{\rm BHNS}^{(\rm local)} = 32^{-24}_{+62}\,{\rm Gpc^{-3}\,yr^{-1}}\,. \tag{4.7}$$

The BBH and BNS merger rates are in Section IV. A in [157] and the BHNS merger rate is chosen from the BGP model in Table II in [157].

In this model, the merger rate in a galaxy follows the star-formation rate, delayed by the lifetime of the binary, from its formation to merger. The formation redshift of stars $z_{\rm f}$ is at time $t_{\rm d}$ before the merger occurs at redshift z, and under the assumption of standard flat Λ-CDM cosmology, it is given by

$$1 + z_{\rm f}(z, t_{\rm d}) = (1+z)\left[\cosh\left(\frac{3\Omega_\lambda^{1/2}\,t_{\rm d}}{2t_{\rm H}}\right) - \frac{E(z)}{\Omega_\lambda^{1/2}}\,\sinh\left(\frac{3\Omega_\lambda^{1/2}\,t_{\rm d}}{2t_{\rm H}}\right)\right]^{-2/3}\,, \tag{4.8}$$

where $E(z) \equiv H(z)/H_0 = \sqrt{\Omega_{\rm m}(1+z)^3 + \Omega_\lambda}$. The delayed star-formation rate is the convolution of the star-formation rate (SFR) with the probability distribution for the delay times $p(t_{\rm d})$ with a proper normalization:

$$\psi_{{\rm d},i}(z) = \frac{1}{\ln(t(z)/t_{{\rm min},i})}\int_{t_{{\rm min},i}}^{t(z)}\frac{{\rm d}t_{\rm d}}{t_{\rm d}}\,\psi(z_{\rm f})\,, \tag{4.9}$$

where the delay time $t_{\rm d}$ has a probability distribution $p(t_{\rm d}) \propto 1/t_{\rm d}$ between the minimum delay time $t_{{\rm min},i} = [20, 50, 50]$ Myr for binary types $i = [{\rm BNS, BBH, BHNS}]$ and the maximum delay time $t_{\rm max}$ which is the age of the Universe $t(z)$ at the redshift of galaxy.

$p_i(\zeta_{\rm b})$ is the normalized probability distribution of the binary merger parameters. For simplicity, the neutron star spins are set to zero, and their masses are uniformly distributed between $1.1M_\odot$ and $2.0M_\odot$. The black hole spins are set to be uniformly distributed between -1 and 1, with mass distribution following the fiducial Power-law + Peak (PP) model in [157] with a range of $[5.08M_\odot,\ 86.85M_\odot]$. For BNS, both neutron stars follow the mass distribution and spin set above. For BHNS, the neutron star and the black hole follow the mass and spin distribution set above for them respectively. For BBH, the primary black hole follows the above mass and spin distribution, while the secondary black hole in the binary system has the same spin distribution but its mass is always smaller than that of the primary black hole.

$f_{\mathcal{Z}}$ is a correction factor due to the assumption that heavy black holes can only be formed in galaxies with small metallicity. Following [91], I keep the assumption that black holes with mass greater than $30M_\odot$ can only be formed in galaxies with $Z \leq \frac{1}{2}Z_\odot$, or equivalently $\mathcal{Z} \leq \log_{10}\frac{1}{2} \approx -0.301 \equiv \mathcal{Z}_{\rm lim}$. Therefore,

$$f_{\mathcal{Z}}(\mathcal{Z}, m_1, m_2) = \begin{cases} 1, & m_1, m_2 < 30M_\odot, \\ \Theta(\mathcal{Z}_{\rm lim} - \mathcal{Z}), & \text{otherwise}\,. \end{cases} \tag{4.10}$$

The normalization factor $\mathcal{I}_i$ in Eq. (4.6) is

$$\mathcal{I}_i = \left[\frac{1}{\ln(t(z)/t_{\min,i})} \int_{t_{\min,i}}^{t(z)} \mathrm{d}(\ln(t_{\rm d}))\, \psi^{(V)}(z_{\rm f})\, \frac{\bar{n}(z)}{\bar{n}(z_{\rm f})} \int_{-\infty}^{\mathcal{Z}_{\max}} \mathrm{d}\mathcal{Z}\; p(\mathcal{Z}|z) \int \mathrm{d}\zeta_{\rm b}\; p_i(\zeta_{\rm b})\, f_{\mathcal{Z}} \right]\Bigg|_{z=0}, \tag{4.11}$$

where $\psi^{(V)}(z)$ is the sum of the galactic star-formation rates per unit comoving volume at redshift z, and $n(z)$ is the number of galaxies per comoving volume. $p(\mathcal{Z}|z)$ is the probability distribution of the log-normalized metallicity $\mathcal{Z}$ over redshift z, which will be discussed later in the next section.

Finally, the anisotropy of the GW energy density $\Omega_{\rm gw}$ predicted by this model can be expanded into spherical harmonics as

$$a_{\ell m}(f) \equiv \int_{\mathrm{S}^2} \mathrm{d}^2\mathbf{e}\; \Omega_{\rm gw}(f, \mathbf{e})\, Y^*_{\ell m}(\mathbf{e}) = \sum_k w_k(f)\, Y^*_{\ell m}(\mathbf{e}_k)\,. \tag{4.12}$$

4.3 The *Euclid* Flagship Simulation of Galaxies

As mentioned above, in this chapter I am using galaxies from the *Euclid* Flagship Galaxy Mock Catalogue (version 2.1.10) [156] on CosmoHub [159, 160]. This simulated catalogue was developed to provide a realistic approximation of the galaxies that will be observed by *Euclid*, based on an N-body simulation with four trillion dark matter particles. It contains ∼4.8 billion galaxies up to magnitude $H_{\rm E} < 26.6$. It covers 1 octant of the sky (∼ 5157 deg^2) centered at approximately the North Galactic Pole ($145° < \mathrm{RA} < 235°, 0° < \mathrm{Dec} < 90°$), and samples the redshift range between 0 and 3.

For each galaxy in this catalogue, I obtain the parameters that are needed in calculation using the method in Section 4.2: redshift z, star-formation rate ψ, stellar mass M_*, and oxygen

abundance "OHa" which is defined as the abundance of oxygen (O) relative to hydrogen (H): $\mathrm{OHa} = 12 + \log_{10}(\mathrm{O/H})$, and the Solar value is 8.69. Then I connect this quantity to the logarithmic metallicity in Section 4.2 by

$$\mathcal{Z} \equiv \log_{10} \frac{Z}{Z_\odot} = \log_{10} \frac{[\mathrm{O/H}]}{[\mathrm{O/H}]_\odot} = \log_{10} \frac{10^{\mathrm{OHa}-12}}{10^{8.69-12}} = \mathrm{OHa} - 8.69\,. \tag{4.13}$$

In order to compute the merger rate in Eq. (4.6), I need to model the galaxy delayed star-formation rate ψ_d, which requires a model of the galaxy star-formation history (SFH) as this information is not provided by the *Euclid* catalogue. I impose a SFH model that is parameterized by the information provided by the *Euclid* catalogue: stellar mass M_* and star-formation rate $\psi(z_\mathrm{obs})$ of the galaxy at redshift z_obs.

Following former literature on the topic [161–165], I implement a mixed model: for galaxies of stellar mass $M_* > 10^{10} M_\odot$ I choose a log-normal exponential SFH model [166], given by

$$\psi(t) = \frac{A}{\sqrt{2\pi\tau^2} \times t} \exp\left\{ - \frac{\left[\ln\left(\frac{t}{1\,\mathrm{Gyr}}\right) - T_0 \right]^2}{2\tau^2} \right\}, \tag{4.14}$$

where A, T_0, τ are parameters, t is the time since the big bang in Gyr. A illustration of the log-normal SFH is shown in Figure 4.1.

The cumulative SFH ψ_c, which is the integral of the SFR, gives the current stellar mass M_* of the galaxy at the time of observation:

$$\psi_\mathrm{c}(t) \equiv \int_0^t \mathrm{d}t'\ \psi(t') = \frac{A}{2} \left\{ 1 - \mathrm{erf}\left[- \frac{\ln\left(\frac{t}{1\,\mathrm{Gyr}}\right) - T_0}{\tau\sqrt{2}} \right] \right\}, \tag{4.15}$$

$$\psi_\mathrm{c}(t_\mathrm{obs}) = 10^9\, M_*\,. \tag{4.16}$$

In order to constrain the three parameters A, T_0, τ with the two known quantities ψ, M_*, the power-law approximation of the relation between the size and center of the $\psi - t$ curve peak is needed:

$$\sigma_\mathrm{SFR} = 0.83\, t_\mathrm{peak}^{3/2}\,. \tag{4.17}$$

These two peak parameters also depend on the three parameters mentioned above:

$$t_\mathrm{peak} = \mathrm{e}^{T_0 - \tau^2},\ \sigma_\mathrm{SFR} = 2\, t_\mathrm{peak}\ \sinh\left(\sqrt{2\ln(2)}\,\tau\right). \tag{4.18}$$

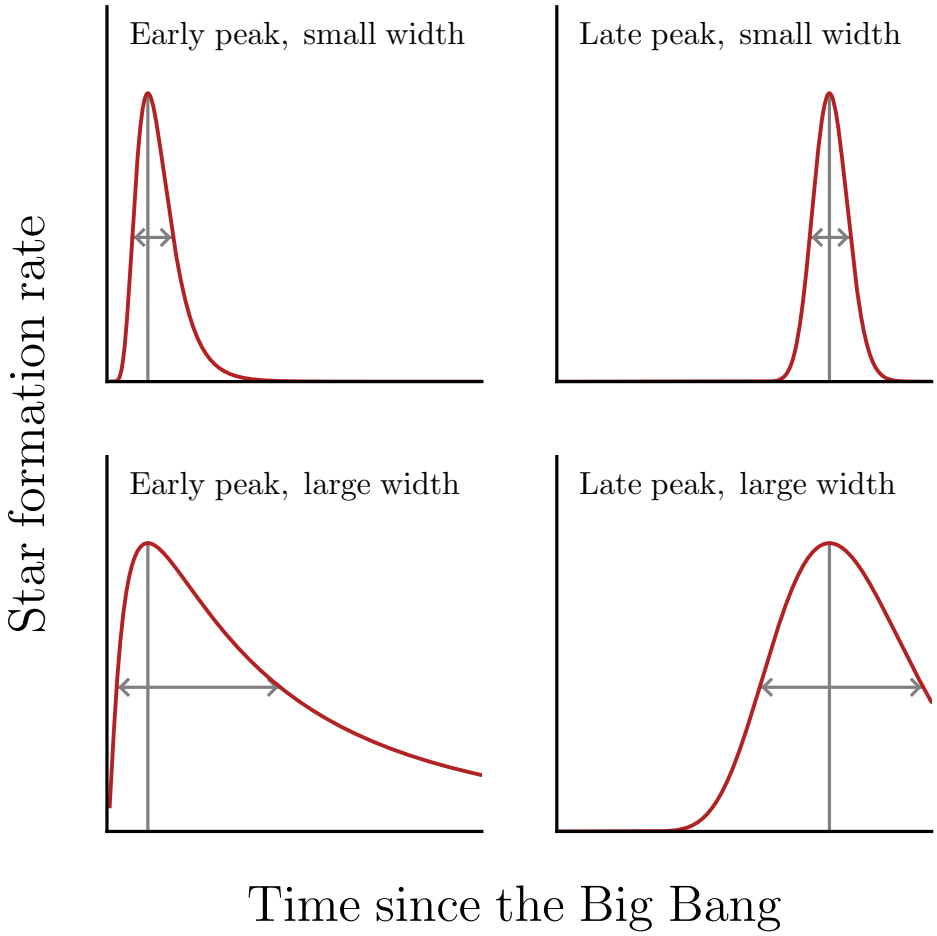

Figure 4.1: Illustration of the log-normal SFH. The shape is determined by the peak time $t_{\rm peak}$ and width $\sigma_{\rm SFR}$ (defined as full width at half maximum). This figure is from [166].

The power-law relation in Eq. (4.17) is valid for a small portion of galaxies; therefore, not all galaxies have numerical solutions using the log-normal exponential model. For those galaxies without valid solutions in this model, especially less massive galaxies, their $\sigma_{\rm SFR}$ is large enough that it is reasonable to treat their SFH as flat:

$$\psi(t) = \psi(t_{\rm obs})\,, \tag{4.19}$$

between a start time t_0 and the time the galaxy is observed $t_{\rm obs}$. So the integral of the SFH gives

the stellar mass M_*:

$$\int_{t_0}^{t_{\rm obs}} {\rm d}t' \; \psi(t') = (t_{\rm obs} - t_0)\, \psi(t_{\rm obs}) = M_* \,, \tag{4.20}$$

hence the start time $t_0 = t_{\rm obs} - M_*/\psi(t_{\rm obs})$.

The galaxy delayed star-formation rate is defined in Eq. (4.9). For some galaxies, the time since the first stars formed is shorter than 50 Myr, so they are not able to form BBH or BHNS ($\psi_{\rm d,BBH} = \psi_{\rm d,BHNS} = 0$). On the other hand, all *Euclid* catalogue galaxies have SFH longer than 20 Myr, so they are all able to form BNS. The median value with the 16th and 84th percentile of the distribution of $\psi_{{\rm d},i}$ for catalogue galaxies in redshift bins of width 0.1 between 0 and 3 is shown in Figure 4.2.]

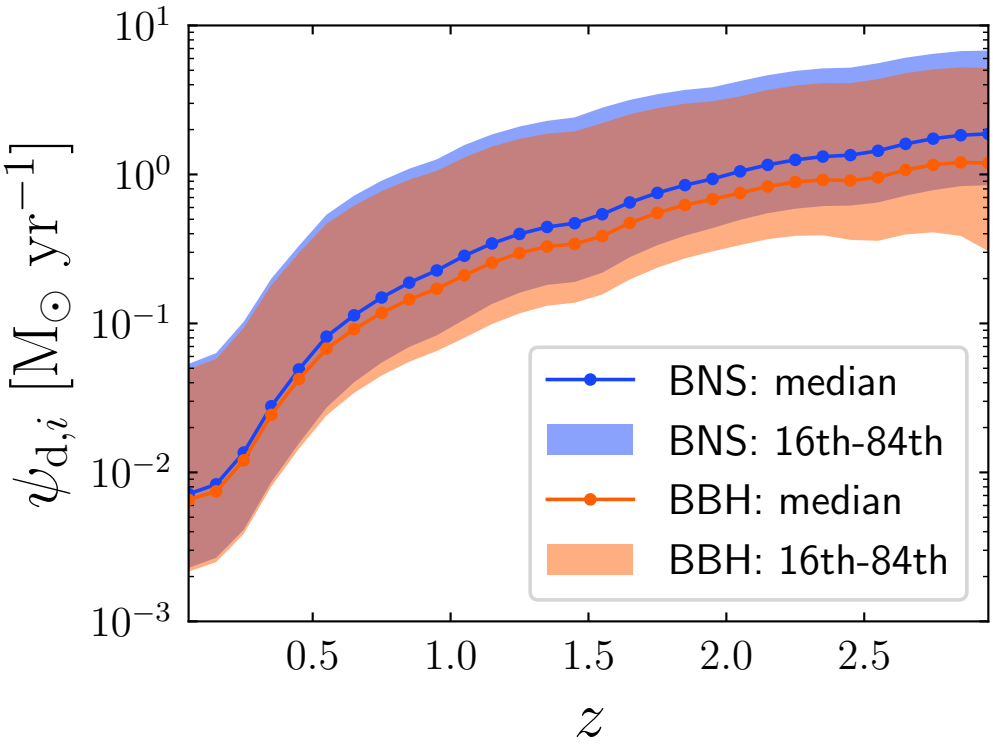

Figure 4.2: The median, 16th and 84th percentile for the delayed star-formation rate computed for minimum time 20 and 50 Myr (corresponding to BNS and BBH or BHNS respectively) using the exponential-flat mixed SFH model for all *Euclid* catalogue galaxies with $H_{\rm E}$ less than 26.6 in redshift bins of 0.1 width.

In order to evaluate the normalization factor I_i in Eq. (4.6), I need to estimate the redshift

dependence of the galaxy number density $\bar{N}$, the star-formation rate density $\psi^{(V)}$ and the log-normalized metallicity probability distribution $p(\mathcal{Z}|z)$, as in Eq. (4.11). I compute the three quantities in redshift bins of width 0.01, as shown in Figure 4.3. The SFR density and metallicity

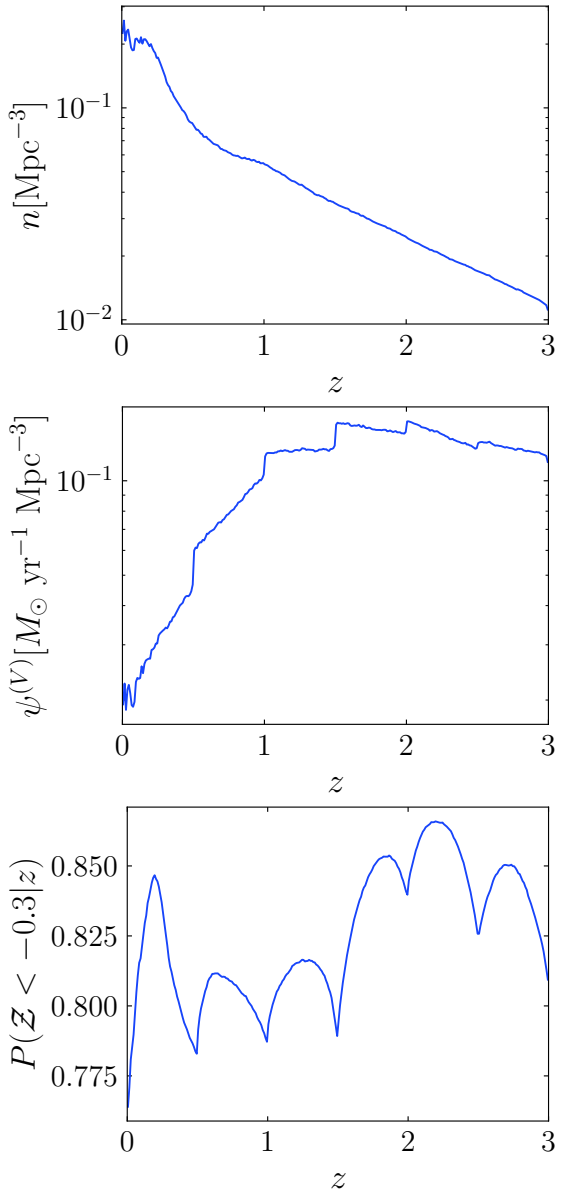

Figure 4.3: (Top:) number density (center:) star-formation rate density in unit comoving volume (bottom:) probability distribution of log-normalized metallicity smaller than $\mathcal{Z}_{\mathrm{lim}}$ at redshift z for galaxies in the *Euclid* catalogue.

distributions in Figure 4.3 show discrete steps in redshift by step 0.5, which is a result of how the *Euclid* simulation is performed. I then use these distributions and a local estimation of $\bar{N}(z=0) \approx 0.223\ \mathrm{Mpc}^{-3}$ to compute I_i in Eq. (4.11) for all types of binaries. As $f_{\mathcal{Z}}$ (defined in Eq. (4.10)) is a selection function for the formation of black holes with mass $\geq 30M_\odot$ in galaxies, the last two integrals of $\mathcal{I}_i$ in Eq. (4.11) for i=BNS are unity; for i=BBH or BHNS, they can be written as

$$\int_{-\infty}^{\mathcal{Z}_{\max}} \mathrm{d}\mathcal{Z}\ p(\mathcal{Z}|z) \int \mathrm{d}\zeta_{\mathrm{b}}\ p_i(\zeta_{\mathrm{b}})\, f_{\mathcal{Z}} = \left[p(\mathcal{Z} < \mathcal{Z}_{\mathrm{lim}}|z) \int_{M_{\mathrm{BH}}^{\min}}^{M_{\mathrm{BH}}^{\max}} \mathrm{d}m_1 + p(\mathcal{Z} \geq \mathcal{Z}_{\mathrm{lim}}|z) \int_{M_{\mathrm{BH}}^{\min}}^{30M_\odot} \mathrm{d}m_1 \right] \times \begin{cases} \displaystyle\int_{M_{\mathrm{BH}}^{\min}}^{m_1} \mathrm{d}m_2 \int_{-1}^{1} \mathrm{d}\chi_1 \int_{-1}^{1} \mathrm{d}\chi_2\ p_i(\zeta_{\mathrm{b}})\,, & \mathrm{BBH} \\ \displaystyle\int_{1.1M_\odot}^{2.0M_\odot} \mathrm{d}m_2 \int_{-1}^{1} \mathrm{d}\chi_1\ \delta(\chi_2)\, p_i(\zeta_{\mathrm{b}})\,, & \mathrm{BHNS} \end{cases} . \tag{4.21}$$

Note that there are the three observational limitations of the *Euclid* catalogue stated above. First, the catalogue covers only 1/8 of the sky. This can be addressed by evaluating all the galaxy properties within 1/8 of the comoving volume, and scaling up their density per comoving value by 8. The angular power spectra C_ℓ for galaxy over-density and cross-correlation with predicted GW energy density anisotropy should both scale up by 8, based on the discussion in Section 3.4 Eq. (3.36) and Section 3.5 Eq. (3.37).

Second, the catalogue contains only galaxies with magnitude $H_{\mathrm{E}} < 26.6$ for the one octant of the sky it covers. However, it also includes a $5 \times 5\ \mathrm{deg}^2$ deep region ($5^\circ < \mathrm{Dec} < 10^\circ, 150^\circ < \mathrm{RA} < 155^\circ$) that contains all galaxies with redshift between 0 and 3 without any H_{E} magnitude constraint. A large portion (80%) of galaxies in this catalogue have $H_{\mathrm{E}} \geq 26.6$. Nevertheless, as they are relatively far away from Earth, they contribute very little (5%) to the total GW energy density, as shown in Figure 4.4. I ignore contributions from these galaxies in subsequent sections of this chapter, and this does not have a significant effect on my results.

Third, the catalogue contains only galaxies with a redshift smaller than 3. Under the assumption that most of the star formation takes place at redshifts below 3, combined with the strong distance suppression of GW signals from higher redshifts, as in Eq. (4.2), the GW energy density will be dominated by low-redshift contributions (i.e., $z < 2$). This redshift cutoff does not have a significant effect on my results.

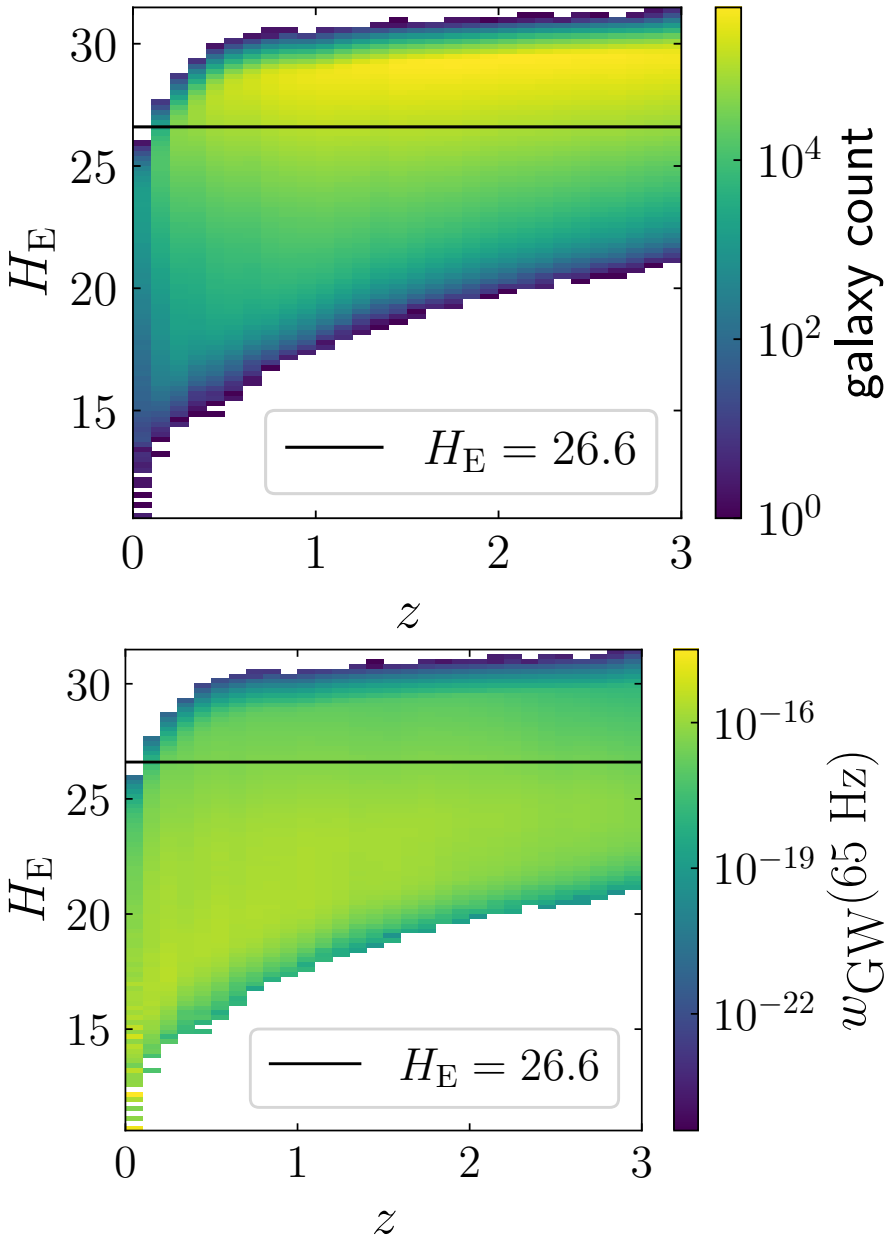

Figure 4.4: 2D histogram of $H_{\rm E}$ and redshift for (top) galaxy number (bottom) total GW energy density at 65 Hz for *Euclid* deep region galaxies. The horizontal lines stand for $H_{\rm E}$ = 26.6.

4.4 Estimates of the Gravitational-Wave Background and Its Angular Power Spectra

4.4.1 Total Gravitational-Wave Energy Density

Using data from the *Euclid* catalogue and following the method in Section 4.3 and 4.2, I computed the expected GW energy density contribution w_k (cf. Eq. 4.1) in every *Euclid* simulated galaxy for the three types of binaries: BNS, BBH, and BHNS. Summing over all galaxies and scaling by the factor of 8 (due to the partial sky coverage of the *Euclid* catalogue) yields a prediction for the total GW energy density due to CBCs. These predictions are shown in Table 4.1 as well as the predictions of the fiducial model inferred using observations during the first three observing runs of LIGO-Virgo in GWTC-3 catalog [157]. My predictions of the GW energy density are 7 times smaller than the predictions of the model in [157]. However, this model assumes the merger rate to follow the global star-formation rate in the Universe, convolved with the formation-to-merger time delay distribution. This is different from the catalog-based approach I use, which is limited to the galaxies available in the *Euclid* catalogue and handles star-formation history separately for each individual galaxy. Nevertheless, my predictions are consistent with the 95% upper limit $\Omega_{\rm GW}(25\ {\rm Hz}) \leq 3.4\times10^{-9}$ for a power-law GW background with a spectral index $\alpha = 2/3$ using data from Advanced LIGO and Advanced Virgo O3 combined with upper limits from O1 and O2 [167]. This paper [91] has a similar calculation of the catalog approach using the *Millennium* simulation. They do not give predictions of the total GW energy density, as they used a restricted sample of galaxies with $z < 0.78$. However, they give an analytical prediction that is 10 times bigger than the semi-analytic model. Note that this analytical calculation was based on earlier estimates of binary merger rates that were higher than those used in this work and in the GWTC-3 estimate [167].

Predictions	frequency [Hz]	$\Omega_{\rm GW}^{\rm tot}$	$\Omega_{\rm GW}^{\rm BNS}$	$\Omega_{\rm GW}^{\rm BBH}$	$\Omega_{\rm GW}^{\rm BHNS}$
Euclid	65	1.73×10^{-10}	2.15×10^{-11}	1.25×10^{-10}	2.57×10^{-11}
GWTC-3	65	1.3×10^{-9}	1.1×10^{-10}	9×10^{-10}	1.7×10^{-10}

Table 4.1: Predicted GW energy density of all types of binaries from various methods.

In order to study the contributions to the GW energy density from galaxies at different redshifts, I compute a 2D histogram of the 10-base logarithm of $w_k^{\rm GW}$ at 65 Hz for galaxy k and its redshift, shown in Figure 4.5. The histogram also shows that most of the galaxies contribute

to the GW energy density $w_k \sim 10^{-22} - 10^{-21}$, and the galaxies at the lowest redshifts can contribute to the GW energy density as much as 10^{-15} although there are relatively fewer of them.

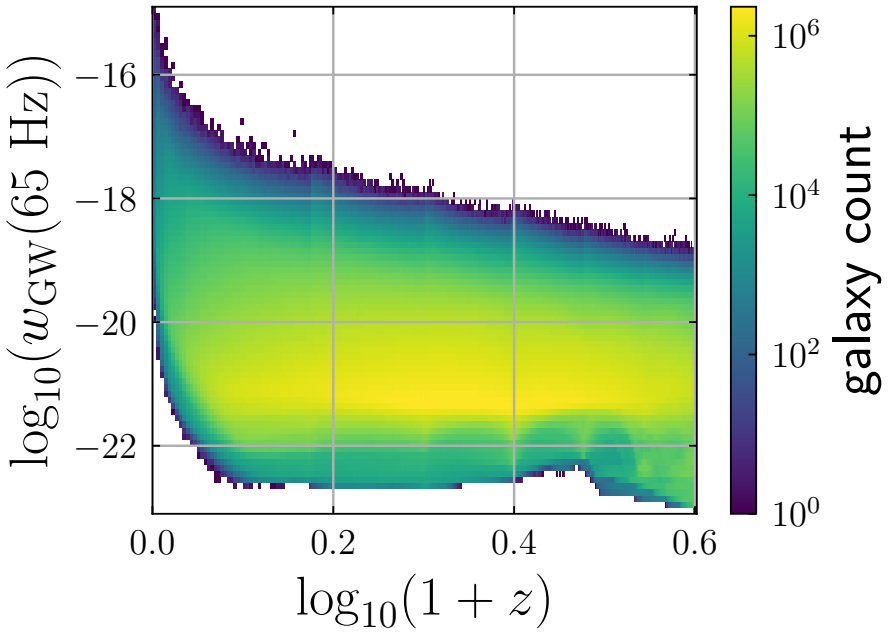

Figure 4.5: 2D binned histogram of $\log_{10} w_k^{\rm GW}$ at 65 Hz and its $\log_{10}(1+z)$ for all *Euclid* galaxies. The colourbar shows number of galaxies more than 200 in each bin.

I also compute the sum of GW energy density from galaxies binned in 0.1-wide redshift bins, shown in Figure 4.6. This figure shows that most of the GW energy density comes from relatively low redshifts ($z \lesssim 1$), which is consistent with past works [36]. This figure also shows that the sum of GW energy density at redshift $z = 3$ is only 15 percent of that at $z = 0.1$. Therefore, this result confirms that the redshift cut of $z < 3$ does not have a significant effect on my predictions.

4.4.2 Gravitational-Wave Background Anisotropy

In order to compute the anisotropy of the GW energy density predicted by this model, I divide the sky into $N_{\rm pix} = 786\,432$ pixels in `HEALPix`-basis, each size of 0.052 deg^2, then sum the GW energy density contributions from all galaxies in each pixel p, and normalize it to the angular

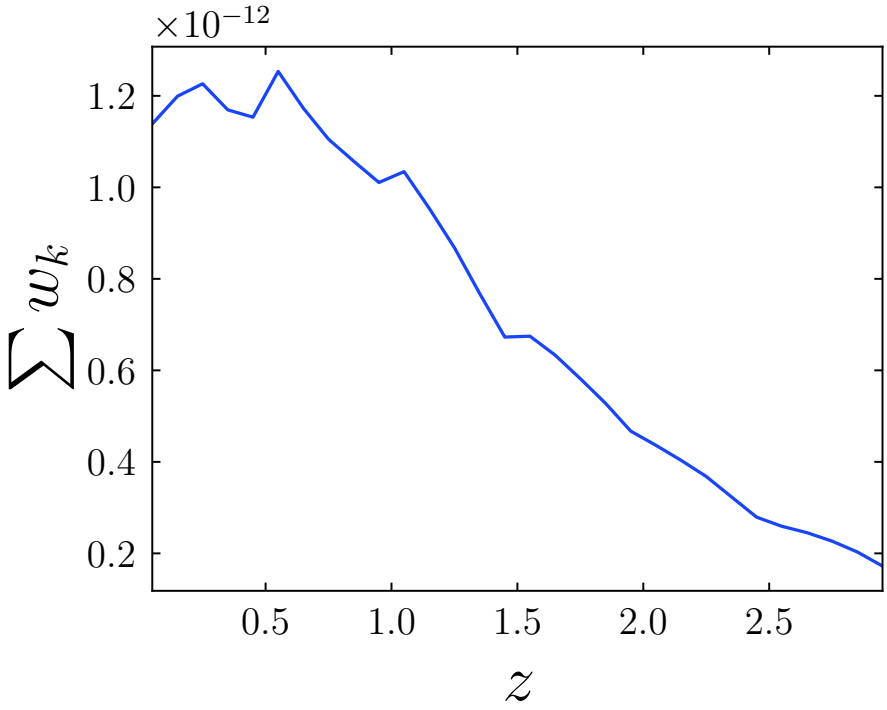

Figure 4.6: Sum of total GW energy density in width-0.1 redshift bins from 0 to 3.

area of the pixel:

$$\hat{\Omega}_p(f) = \frac{N_{\rm pix}}{4\pi} \sum_{k\in p} \sum_i w_{k,i}(f)\,. \tag{4.22}$$

Then I plot the GW energy density sky map of Ω_p using `HEALPix` [168, 169]. As edge pixels are not fully covered by galaxies in the *Euclid* catalogue, in order to get a better estimate of the anisotropies, I removed these pixels, as shown in Figure 4.7. Therefore the sky coverage fraction $1/f_{\rm sky}$ is now 8.028 instead of 8.

Next, I compute the fluctuations of GW energy density in pixels as $\delta\hat{\Omega}_p = \hat{\Omega}_p - \bar{\Omega}_p$, where the average pixel value $\bar{\Omega}_p$ is computed over pixels that are fully covered by the *Euclid* catalogue. The spherical harmonics expansion of the GW energy density fluctuation `HEALPix` sky map is defined in [168] as

$$\hat{a}_{\ell m} = \frac{4\pi}{N_{\rm pix}} \sum_{p=0}^{N_{\rm pix}-1} Y^*_{\ell m}(\gamma_p)\, \delta\hat{\Omega}_p\,, \tag{4.23}$$

where γ_p is a unit vector pointing at the center of pixel p with sky location (θ, ϕ).

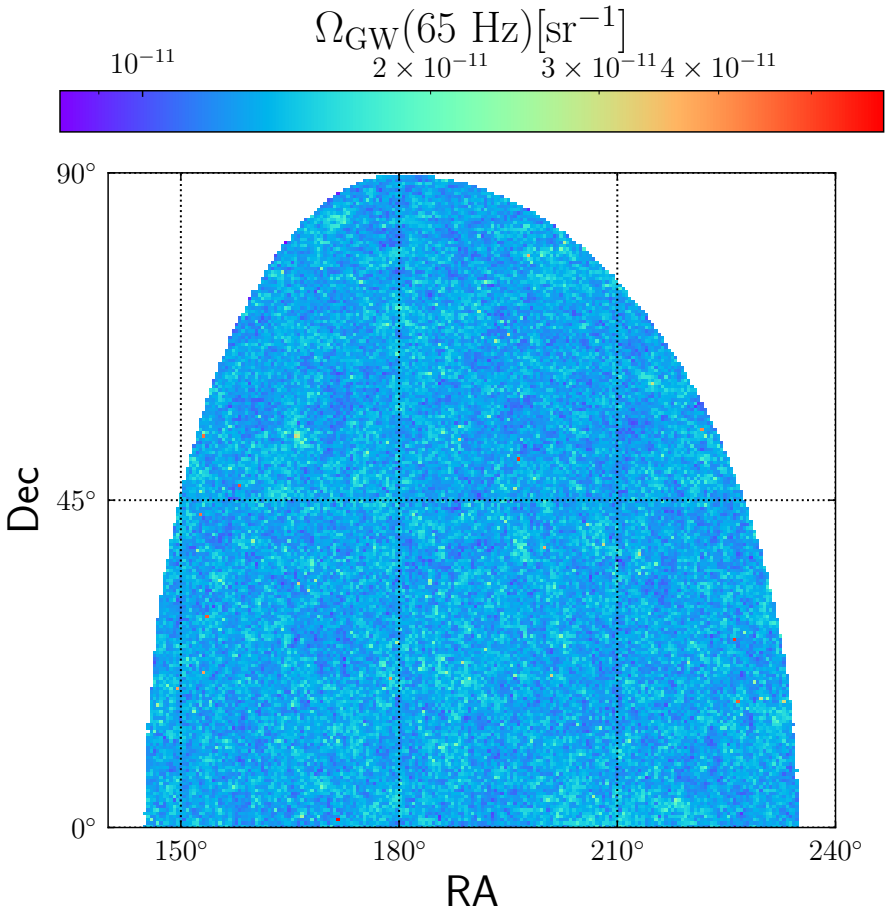

Figure 4.7: GW total energy density summed over all types of binaries at 65 Hz for all *Euclid* Flagship galaxies with $H_{\rm E}$ less than 26.6 per angular size in `HEALPix` for pixels of $N_{\rm pix} = 786\,432$ with removal of the edge pixels. The colors are on a log scale.

The angular power spectrum is then estimated as

$$\hat{C}_\ell^{\rm GW} = \frac{1}{(2\ell+1)\,f_{\rm sky}} \sum_{m=-\ell}^{\ell} \left|\hat{a}_{\ell m}\right|^2 , \tag{4.24}$$

with the corresponding cosmic variance being

$$\sigma_{\rm C}^2(\hat{C}_\ell^{\rm GW}) = \frac{2\,(\hat{C}_\ell^{\rm GW})^2}{(2\ell+1)\,f_{\rm sky}} . \tag{4.25}$$

Another source of variance comes from the uncertainty in the local merger rate. This contribution can be estimated from the upper (95%) and lower (5%) bounds as

$$\sigma_{\rm R}^2(\hat{C}_\ell^{\rm GW}) = \left(\frac{\hat{C}_\ell^{\rm up} - \hat{C}_\ell^{\rm low}}{2 \cdot 1.6}\right)^2 , \tag{4.26}$$

where $\hat{C}_\ell^{\rm up}$ (or $\hat{C}_\ell^{\rm low}$) is computed from the GW map with the GW energy density of different types of binaries using the corresponding 95% upper bound (or 5% lower bound) of the local merger rate in Eq. (4.7).

The total variance is then given by the two variances added quadratically

$$\sigma_{\rm tot}^2(\hat{C}_\ell^{\rm GW}) = \sigma_{\rm C}^2(\hat{C}_\ell^{\rm GW}) + \sigma_{\rm R}^2(\hat{C}_\ell^{\rm GW}) . \tag{4.27}$$

The results of the prediction of $\hat{C}_\ell^{\rm GW}$ and the corresponding variances in Eqs. (4.25-4.27) of the GW energy density fluctuations are shown in Figure 4.8. We can see from this figure that the total variance $\sigma_{\rm tot}^2$ is dominated by the uncertainty of the local merger rate $\sigma_{\rm R}^2$ at high ℓ, but for $\ell < 40$, it is dominated by the cosmic variance $\sigma_{\rm C}^2$, and its lower bound lies below the visible range on the logarithmic scale. This is due to the partial sky coverage of the *Euclid* catalogue, as the cosmic variance is of similar magnitude as the $\hat{C}_\ell^{\rm GW}$ at low ℓ. The figure also reveals oscillatory features in the $\hat{C}_\ell^{\rm GW}$ as a function of ℓ, primarily resulting from the partial sky coverage of the *Euclid* catalogue, which leads to information loss at low multipoles. To mitigate these fluctuations at higher ℓ, the curve can be smoothed by averaging over adjacent multipole bins rather than evaluating each integer ℓ individually.

This prediction of $\hat{C}_\ell^{\rm GW}$ is around 10^{10} times smaller than the 95% upper limits on broadband (20–1000 Hz) C_ℓ for SGWB from CBC ($\alpha = 2/3$) using combined O1, O2 and O3 data [149]. This prediction is also 10^{12} times smaller compared to the measurements of $\hat{C}_\ell^{\rm GW}$ in the 60–70 Hz frequency band with $\ell_{\rm max} = 5$ in Section 3.3.3 (see Figure 3.5 for reference), which is dominated by LIGO detector noise.

When computing the estimations of the angular power spectra of GW energy density fluctuations, I found a shot-noise limitation which affects the high-ℓ spectra that rises when the catalog contains a relatively small number of galaxies. In order to demonstrate this effect, I focus on the *Euclid* catalogue in redshift bin $0 < z < 0.1$, which contains about 8.5 million galaxies. Following the procedure in the above text, I similarly divide these galaxies into $N_{\rm pix} = 786\,432$

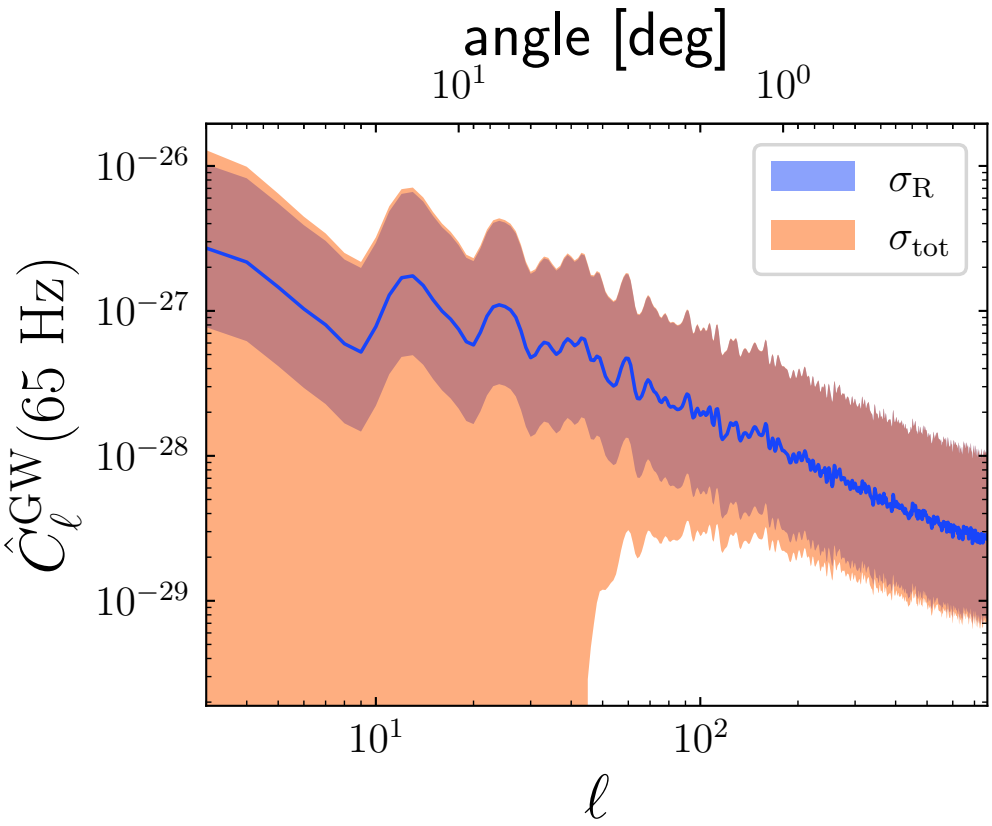

Figure 4.8: GW energy density C_ℓ is shown as a solid line, including contributions from all three binary types (BBH, BNS, and BHNS). Two 90% confidence uncertainty regions are shown: the blue region shows the uncertainty due to the uncertainty in the local merger rate, while the orange region shows the total uncertainty in Eq. (4.27).

pixels in `HEALPix`-basis, and compute the angular power spectrum $\hat{C}_\ell^{\rm GW}$ defined in Eq. (4.24), which is shown as the blue solid curve in Figure 4.9. Then I randomly sample 15%, 20% and 30% of galaxies in each `HEALPix` pixel and repeat this calculation. As galaxy count in pixels must be integers, the above choices of percentages ensure that every valid pixel is included during sampling (i.e., sample number in pixel $\geq$ 1), so that the same pixels are used for the no-sampling case and all the choices of samples. For every choice of samples, I replace the average of the GW energy density of all galaxies in every pixel by the average of the sampled galaxies. The result is shown in Figure 4.9. It shows that, when computed with fewer galaxies, $\hat{C}_\ell^{\rm GW}$ plateaus at high values of ℓ as compared to the no-sampling case when all galaxies are

used, and the plateau starts at lower ℓ as the sample size decreases. Please note that the $\hat{C}_\ell^{\rm GW}$ with 15% sampling is at lower level at $\ell \geq 10^2$ compared to 20% sampling, this is possibly due to the loss of energy with an incomplete catalog. Nevertheless, this does not affect the trend that larger size of samples plateaus at higher values of ℓ, as the 20% sampling curve plateaus at higher values of ℓ compared to the 15% sampling curve. It is worth noting that Figure 4 in [91] shows similar behavior. As their result is computed using a subset of the catalogue from the *Millennium* simulation containing 5.7 million galaxies, one can see that high-ℓ limit of their catalog approach may have been impacted by the shot-noise limitation.

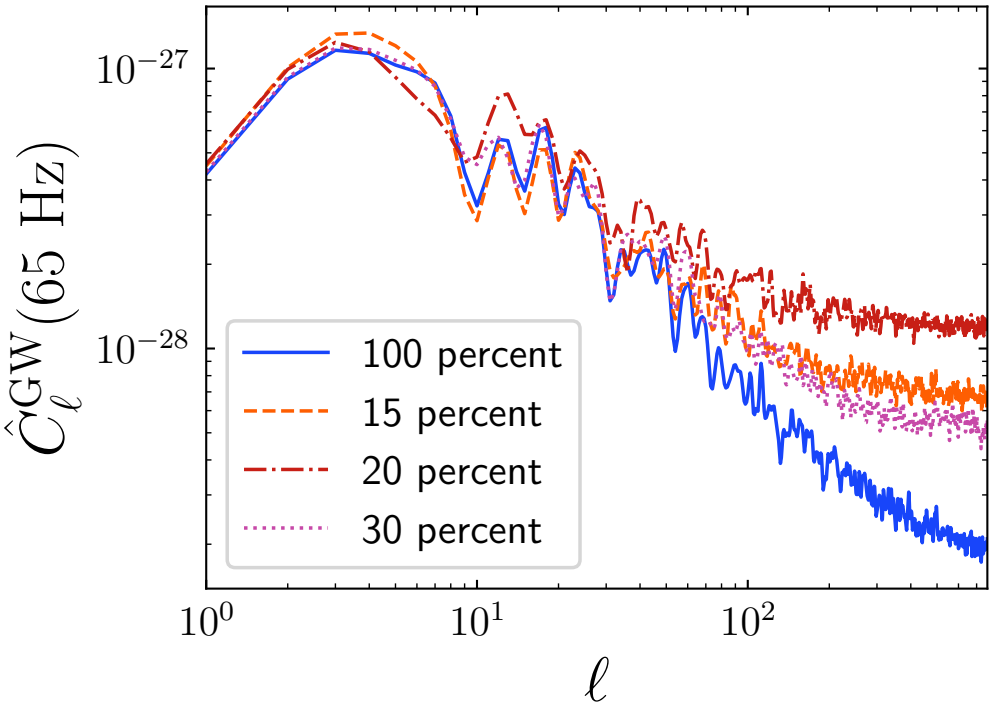

Figure 4.9: Angular power spectra of GW energy density fluctuations at 65 Hz using all (100%) or 15%, 20%, 30% of galaxies with $0 < z < 0.1$ in the *Euclid* catalogue. The angular spectra computed with fewer galaxies plateau at high values of ℓ, and the plateau starts at lower values of ℓ if there are fewer galaxies in the sample.

4.4.3 Cross Correlating GW Background and Galaxy Distribution

I then compute the cross-correlation angular power spectra of the GW energy density fluctuation and galaxy count over-density in the *Euclid* catalogue. Similar to the process in Section 4.4.2,

I label the number count of galaxies in the sky pixel p as $\hat{n}_p$, and the galaxy count over-density as $\hat{\Delta}_p = (\hat{n}_p - \bar{n})/\bar{n}$, where $\bar{n}$ is the average number of galaxies in pixels. Its spherical harmonics expansion is

$$\hat{b}_{\ell m} = \frac{4\pi}{N_{\rm pix}} \sum_{p=0}^{N_{\rm pix}-1} Y^*_{\ell m}(\mathbf{e}_p)\, \hat{\Delta}_p \,. \tag{4.28}$$

Then the angular power spectrum of its cross-correlation with the GW energy density fluctuations is

$$\hat{C}_\ell^{\rm cross} = \frac{1}{(2\ell+1)\, f_{\rm sky}} \sum_{m=-\ell}^{\ell} \hat{b}^*_{\ell m}\, \hat{a}_{\ell m} \,, \tag{4.29}$$

Note that $\hat{a}_{\ell m}$ is computed using Eq. (4.12). The corresponding cosmic variance is [170]

$$\sigma^2_{\rm C}(\hat{C}_\ell^{\rm cross}) = \frac{\hat{C}_\ell^{\text{GW-GW}}\, \hat{C}_\ell^{\text{gal-gal}} + (\hat{C}_\ell^{\rm cross})^2}{(2\ell+1)\, f_{\rm sky}} \,. \tag{4.30}$$

Note that the $f_{\rm sky}$ in the denominator remains necessary to maintain the appropriate level of variance under partial sky coverage. Recall that we have included it in Eq. (4.29) to obtain the estimation of $\hat{C}_\ell^{\rm cross}$.

Variance due to the range of local merger rate is similar to Eq. (4.26):

$$\sigma^2_{\rm R}(\hat{C}_\ell^{\rm cross}) = \left(\frac{\hat{C}_\ell^{\rm up} - \hat{C}_\ell^{\rm low}}{2 \cdot 1.6}\right)^2 , \tag{4.31}$$

where $\hat{C}_\ell^{\rm up}$ and $\hat{C}_\ell^{\rm low}$ are computed by Eq. (4.29) using the $\hat{a}_{\ell m}$ from the upper and lower bound GW maps treated the same way as in Eq. (4.26), with the same $\hat{b}_{\ell m}$ as in Eq. (4.29). The total variance is then

$$\sigma^2_{\rm tot}(\hat{C}_\ell^{\rm cross}) = \sigma^2_{\rm C}(\hat{C}_\ell^{\rm cross}) + \sigma^2_{\rm R}(\hat{C}_\ell^{\rm cross}) \,. \tag{4.32}$$

The results of $\hat{C}_\ell^{\rm cross}$ and the variances in Eqs. (4.30-4.32) are shown in Figure 4.10. Similar to the SGWB auto-correlation case in Figure 4.8, for $\ell < 40$ the total variance $\sigma^2_{\rm tot}(\hat{C}_\ell^{\rm cross})$ is dominated by the cosmic variance of similar magnitude of $\hat{C}_\ell^{\rm cross}$ and its lower bound falls below the display threshold on a logarithmic scale due to partial sky coverage. The wiggling trend over ℓ is stressed for the SGWB auto-correlation case (see Figure 4.8). The result is compared to the measurements of $\hat{C}_\ell^{\rm cross}$ in the 60–70 Hz frequency band in Section 3.5 (see Figure 3.8 for reference), which is around 10^7 times larger with $\ell_{\rm max} = 5$. I also compare the results to the

Gaussian parameterized astrophysical models in Section 3.2, which is shown in this figure in red dotted line with the best-fit parameter values obtained by exploring the parameter space. This process will be done in the following text. The figure shows good agreement between my results and the best-fit model for $\ell \geq 40$. At lower multipoles, the trend is not captured, likely due to limited information from partial sky coverage.

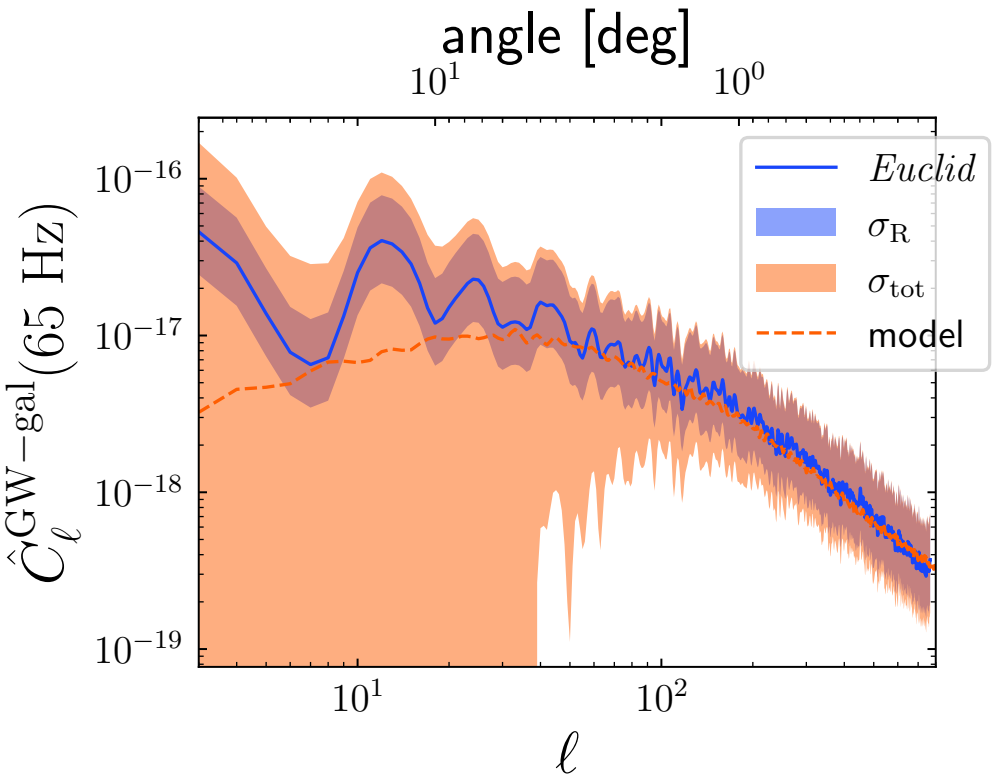

Figure 4.10: Angular spectrum for cross-correlation between GW background and galaxy overdensity is shown as a solid blue line. Two 90% confidence uncertainty regions are also shown including the uncertainty due local binary merger rate (blue) and due to the total variance (orange). For comparison, we show the red dashed line which is the astrophysical model $C_\ell^{\mathrm{cross}}(\theta)$ in Eq. (3.13) with $\theta = [A_{\mathrm{max}} = 1.42 \times 10^{-37} \mathrm{erg\,cm^{-3}\,s^{-1/3}}$, $z_c = 1.08$, $\sigma_z = 0.27]$.

I further compare the estimate using the above catalog approach with the astrophysical models of cross-correlation in Section 3.2. As the *Euclid* catalogue contains galaxies with $0 < z < 3$, I update the flat window function $W(r)$ in Eq. (3.15) to cover this redshift range ($z = z(r)$) while its integration over conformal distance r still yields 1. The astrophysical models in [98] are also mentioned in Section 3.2. These models describe the formation and evolution of

merging BBHs differently through the astrophysical kernel $\mathcal{A}(f, z)$, whose redshift dependence can be parameterized by a Gaussian distribution in Eq. (3.4) constrained by three parameters $\theta = (A_{\rm max}, z_c, \sigma_z)$, where $A_{\rm max}$ represents the amplitude of the kernel, z_c is the peak redshift, σ_z is the peak width of the Gaussian distribution of redshift dependence of the kernel. For the models in [98], the range of parameters of the Gaussian fit for $0 < z < 2$ (note that for $z > 2$ the Gaussian distribution breaks) at 63 Hz are: $A_{\rm max} \in [1, 3] \times 10^{-37} \mathrm{erg\,cm^{-3}\,s^{-1/3}}$, $z_c \in [0, 3, 1.8]$, $\sigma_z \in [0.3, 1.2]$. This is also stated in Section 3.2.1.

Following the parameter estimation procedure in Section 3.6, I explore the parameter space for comparison of these parameterized astrophysical models with my predictions using the *Euclid* catalogue. Following the definition of logarithmic likelihood in Eq. (3.41) for cross-correlation angular power spectra, I similarly define a logarithmic likelihood with my predictions $\hat{C}_\ell$, the models $C_\ell(\theta)$ that depend on parameters θ and a diagonal covariance matrix K_C given by the total variance in Eq. (4.32) assuming perfect observation:

$$\begin{aligned} \ln \mathcal{L}(\hat{C}_\ell | C_\ell(\theta)) &= -\frac{1}{2} \ln |K_C| - \frac{1}{2} (\hat{C}_\ell - C_\ell(\theta))^T \, K_C^{-1} \, (\hat{C}_\ell - C_\ell(\theta)) \\ &= -\frac{1}{2} \sum_l \ln \sigma^2(\hat{C}_\ell) - \frac{1}{2} \frac{(\hat{C}_\ell - C_\ell(\theta))^2}{\sigma^2(\hat{C}_\ell)} \,, \end{aligned} \tag{4.33}$$

where all superscripts of "cross" are omitted for simplicity.

Then I search in the 3-dimensional parameter space $(A_{\rm max}, z_c, \sigma_z)$ with uniform priors of all three parameters $A_{\rm max} \in [1.0 \times 10^{-38}, 5.0 \times 10^{-37}] \,\mathrm{erg\,cm^{-3}\,s^{-1/3}}$, $z_c \in [0.20, 1.80]$, $\sigma_z \in [0.01, 1.20]$. The resulting posterior probability curves and contour plots are shown in Figure 4.11. This figure yields the best-fit parameters $A_{\rm max} = 1.4 \times 10^{-37} \mathrm{erg\,cm^{-3}\,s^{-1/3}}$, $z_c = 1.08$, $\sigma_z = 0.27$. The $C_\ell(\theta)$ with the best-fit θ is shown in a red dashed line in Figure 4.10. We can see that it matches with my prediction of cross-correlation $\hat{C}_\ell$ in a solid blue line for $\ell > 30$. The best-fit value for the kernel amplitude $A_{\rm max}$ is within the range of values that describe the astrophysical models in [98].

4.5 Discussion and Conclusion

In this chapter, I predicted the GW energy density due to compact binary coalescences from the galaxies in the *Euclid* catalogue. I implemented a model of star-formation history for each galaxy, parameterized by its current stellar mass and star-formation rate. Then I combined the

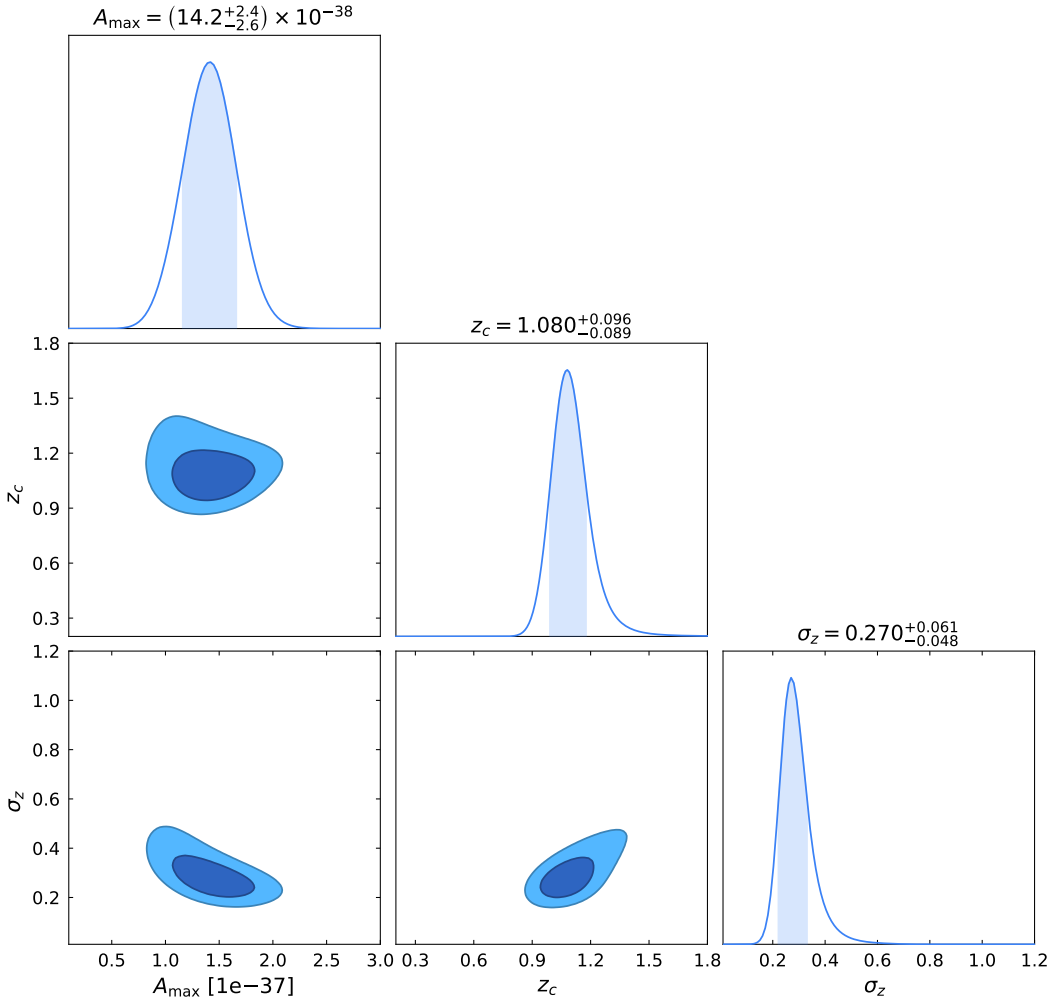

Figure 4.11: Contour plots in 3D parameter space of ($A_{\rm max}$, z_c, σ_z) for GW fluctuation × galaxy over-density cross-correlation $\hat{C}_\ell$ and astrophysical model $C_\ell(\theta)$, $\theta = (A_{\rm max}, z_c, \sigma_z)$ with uniform priors for all parameters.

modelled SFH with the probability distribution of $p(t_{\rm d})$ to obtain the delayed SFR $\psi_{\rm d}$. Combined with the metallicity distribution $p(\mathcal{Z})$ and the inferred distribution of binary masses and spins in [167], I obtain the local merger rate following the model in [91]. I computed the GW energy density and its anisotropy due to three types of CBC (BNS, BBH and BHNS) using this method. Following the approach in Chapter 3, I predicted the angular power spectra of the GW anisotropy and its cross-correlation with the galaxy distribution. Finally I compared my prediction of cross-correlation to the predictions of the models in Section 3.2 or in [98] and

applied a Bayesian approach to explore the parameter space of the models, with assumptions of perfect experiment with zero instrumental noise. Similarly to the approach in Section 3.6, I set constraints on the model parameters, and the best-fit values lie within the range of values that fit the models in [98].

This study serves as an initial step toward developing a consistent framework for utilizing future *Euclid* data. Future measurements of the SGWB angular power spectrum and the SGWB-galaxy correlation angular power spectrum can be used to constrain the combination of ψ, $p(t_{\rm d})$, and $p(\mathcal{Z})$. Moreover, combining these measurements with other observations such as SFH measurements by *Euclid* can then further constrain the remaining quantities.

The next step will involve incorporating simulated noise components into the *Euclid* catalogues and replicating realistic LVK background noise. This preparation will enhance our ability to analyze both galaxy and background data, allowing us to anticipate the expected outcomes of future correlations.

Chapter 5

Conclusion and Discussion

The Advanced Laser Interferometer Gravitational-wave Observatory (LIGO) detects various sources of gravitational waves including compact binary coalescences, supernova explosions, and stochastic sources. The stochastic gravitational wave background results from many unresolved weak gravitational wave sources across the Universe. LIGO-Virgo-KAGRA have published the measurement of the persistent directional stochastic gravitational-wave background (SGWB) based on data from their first, second and third observing runs. The fourth observing run is ongoing, and the first eight months of data have just been released.

The stochastic gravitational wave background is thought to arise from two primary classes of sources: cosmological and astrophysical. Both components are expected to exhibit anisotropies, resulting from different mechanisms. Therefore, the energy density of the SGWB may exhibit correlations with anisotropies in electromagnetic tracers of large-scale structure, such as galaxy number counts, weak lensing signals, cosmic microwave background, cosmic infrared background, etc.

Measuring these correlations offers tools to probe matter distribution and its evolution in the Universe. Studying the frequency and redshift spectrum of these correlations may reveal differences between mechanisms. Furthermore, as we have not detected an SGWB signal, measuring the correlations can help us in the upper limit measurement of the SGWB by improving the sensitivity of searches for anisotropy in the SGWB. Cross-correlation can also expand the use of SGWB anisotropy to probe the formation of structure in the Universe.

I focused on searching for the cross-correlation between the anisotropy of the stochastic background and galaxy count distributions. I started with LIGO second observing run data,

computed the spherical harmonic decomposition of the anisotropic SGWB measured in 50 Hz-wide frequency bands, and converted them into pixel-based sky maps in HEALPIX basis. Then I computed the distribution of galaxies in the Sloan Digital Sky Survey (SDSS) photometric and spectroscopic catalogs, binned in redshift intervals of width 0.1. These counts were projected onto the sky using the HEALPIX pixelization scheme, producing number count maps at the same angular resolution as the SGWB maps. I further computed the pixel-based coherence between the SGWB maps in frequency bands and galaxy count maps in redshift bins. I found that the coherence is dominated by the null measurement noise in the SGWB maps and lacks statistical significance.

As a step forward, I then moved on to the more sensitive data during LIGO's third observing run (O3). Building on the anisotropic SGWB measurements from LIGO's first three observing runs (O1-O3), I used the strain data segments summed into narrower 10 Hz frequency bins to investigate the spectral dependence across frequencies. I also focused on the SDSS spectroscopic catalog only and studied the galaxy count overdensity distributions without binning in redshift. Subsequently, I computed the angular power spectra for both the auto-correlations and the cross-correlation between the SGWB and galaxy count overdensity. The measured cross-correlation was then compared against estimations from a Gaussian parameterization of astrophysical models of the SGWB due to BBH mergers. To probe the theoretical parameter space, I employed a Bayesian framework, enabling the derivation of constraints on key astrophysical parameters that characterize the kernel governing galactic gravitational-wave (GW) emission processes. I also repeated this process with inclusion of shot noise and compared the results to the case without inclusion of shot noise. Including shot noise enhances sensitivity to weaker signals, but also introduces greater uncertainty in their recovery. The Bayes factor comparing the model without shot noise and the model with shot noise is less than 1, showing the preference for inclusion of shot noise.

This analysis built a new formalism to measure the cross-correlation of SGWB and galaxy count overdensities, which can help improve the sensitivity of measurements of the SGWB and set better constraints on astrophysical models. One possible extension of this analysis is to study the redshift dependence of the cross-correlation by binning galaxies in narrow redshift slices. This may help discriminate among different contributions of mechanisms of SGWB from compact binary mergers. Future work could explore the cross-correlations between SGWB and

other electromagnetic tracers of structure in the Universe such as weak lensing, Cosmic Microwave Background, Cosmic Infrared Background, and others. Establishing a joint analysis of all these cross-correlations may improve the overall sensitivity of the approach and enable distinguishing different contributions to the model of SGWB due to compact binary coalescences. Advanced LIGO, Advanced Virgo, and KAGRA are expecting to keep improving the sensitivity of the GW detector network and extend the observation time in the future observing runs (04, 05,...). The next generation of ground based detectors-including the Einstein Telescope [154] and Cosmic Explorer [155]-will significantly advance sensitivity. Applying the approach to the future datasets, will then consequently improve its sensitivity and enable more stringent constraints on the Gaussian parameters of the astrophysical models.

Building on the previous stage, I proceeded to estimate the amplitude and spatial anisotropy in the SGWB energy density from compact binary coalescence (CBC) events residing within galaxies. I made use of the Flagship Galaxy Mock Catalogue developed by the Euclid Consortium. This catalogue is produced to provide a realistic approximation to the galaxies that will be observed by *Euclid*, and it contains 4.8 billion galaxies in one octant of the sky up to redshift $z = 3$. This catalogue uses models of galaxy properties' distributions to simulate these properties for each galaxy. Modeled galaxy properties include redshifts, positions and velocities, stellar masses, star formation rates, metallicities and others. For each galaxy in the catalogue, I used the simulated stellar mass and star formation rate to constrain the galaxy's star formation history (SFH) with a mixed model. I used the SFH and metallicity to predict the contribution of galaxies to the SGWB from different types of compact binary mergers, based on the inferred values of local merger rates and mass/spin distributions of binaries from GW data through GWTC-3. I then computed the total SGWB energy density and compared it to the inferred value from GWs through GWTC-3, my predictions were 10 times smaller. I also predicted the anisotropy of SGWB energy density, and computed the angular power spectra for both the auto-correlations and the cross-correlation between the SGWB anisotropy and galaxy count overdensity from the *Euclid* Mock catalogue without binning in redshift. I compared my predictions to the astrophysical models following the same process stated above. I explored the parameter space with a combined covariance of cosmic variance and deviations in the inferred local merger rate and set constraints on the model parameters. The resulting best-fit values lie within the realistic range of values of the Gaussian parameterized astrophysical models.

This analysis represents a preliminary effort toward establishing a coherent framework for

the interpretation of forthcoming *Euclid* data. Future measurements of the SGWB angular power spectrum, along with its cross-correlation with the *Euclid* measurements of the galaxy count overdensities, will enable constraints on models of galaxy properties. Furthermore, integrating these datasets with complementary observations such as star formation history measurements from *Euclid* will allow for tighter constraints on residual astrophysical parameters. The next step will incorporate simulated noise components into the *Euclid* catalogues and emulate realistic LVK background noise. This preparatory step will improve the robustness of our analysis of both galaxy and background datasets, enabling more accurate forecasts of expected correlation signals in future observations.

References

[1] Steven Weinberg. *Gravitation and Cosmology: Principles and Applications of The General Theory of Relativity*. John Wiley and Sons, Inc., 1971.

[2] Michele Maggiore. *Gravitational Waves: Volume 1: Theory and Experiments*. Oxford University Press, 2007.

[3] Benjamin P. Abbott et al. Sensitivity of the Advanced LIGO detectors at the beginning of gravitational wave astronomy. *Phys. Rev. D*, 93(11):112004, 2016, 1604.00439. [Addendum: Phys.Rev.D 97, 059901 (2018)].

[4] LIGO Scientific Collaboration. Advanced LIGO. *Classical and Quantum Gravity*, 32(7):074001, April 2015, 1411.4547.

[5] Aaron Buikema et al. Sensitivity and performance of the Advanced LIGO detectors in the third observing run. *Phys. Rev. D*, 102(6):062003, 2020, 2008.01301.

[6] B. P. Abbott et al. Observation of Gravitational Waves from a Binary Black Hole Merger. *Phys. Rev. Lett.*, 116(6):061102, 2016, 1602.03837.

[7] B. P. Abbott et al. GW150914: First results from the search for binary black hole coalescence with Advanced LIGO. *Phys. Rev. D*, 93(12):122003, 2016, 1602.03839.

[8] B. P. Abbott et al. Binary Black Hole Mergers in the first Advanced LIGO Observing Run. *Phys. Rev. X*, 6(4):041015, 2016, 1606.04856.

[9] B. P. Abbott et al. GW151226: Observation of Gravitational Waves from a 22-Solar-Mass Binary Black Hole Coalescence. *Phys. Rev. Lett.*, 116(24):241103, 2016, 1606.04855.

[10] Benjamin P. Abbott et al. GW170104: Observation of a 50-Solar-Mass Binary Black Hole Coalescence at Redshift 0.2. *Phys. Rev. Lett.*, 118(22):221101, 2017, 1706.01812.

[11] B. P. Abbott et al. GW170608: Observation of a 19-solar-mass Binary Black Hole Coalescence. *Astrophys. J. Lett.*, 851:L35, 2017, 1711.05578.

[12] B. P. Abbott et al. GW170814: A Three-Detector Observation of Gravitational Waves from a Binary Black Hole Coalescence. *Phys. Rev. Lett.*, 119(14):141101, 2017, 1709.09660.

[13] B. P. Abbott et al. GWTC-1: A Gravitational-Wave Transient Catalog of Compact Binary Mergers Observed by LIGO and Virgo during the First and Second Observing Runs. *Phys. Rev.*, X9(3):031040, 2019, 1811.12907.

[14] B. P. Abbott et al. GW170817: Observation of Gravitational Waves from a Binary Neutron Star Inspiral. *Phys. Rev. Lett.*, 119(16):161101, 2017, 1710.05832.

[15] R. Abbott et al. GWTC-2: Compact Binary Coalescences Observed by LIGO and Virgo During the First Half of the Third Observing Run. *Phys. Rev. X*, 11:021053, 2021, 2010.14527.

[16] R. Abbott et al. GWTC-2.1: Deep extended catalog of compact binary coalescences observed by LIGO and Virgo during the first half of the third observing run. *Phys. Rev. D*, 109(2):022001, 2024, 2108.01045.

[17] R. Abbott et al. GWTC-3: Compact Binary Coalescences Observed by LIGO and Virgo during the Second Part of the Third Observing Run. *Phys. Rev. X*, 13(4):041039, 2023, 2111.03606.

[18] R. Abbott et al. Tests of general relativity with GWTC-3. *arXiv:2112.06861, accepted for publication in Phys. Rev. D*, 2022.

[19] R. Abbott et al. Constraints on the cosmic expansion history from GWTC-3. *arXiv:2111.03604, accepted for publication Ap.J.*, 2022.

[20] B. P. Abbott et al. GW170817: Measurements of neutron star radii and equation of state. *Phys. Rev. Lett.*, 121:161101, Oct 2018.

[21] R. Abbott et al. All-sky search for continuous gravitational waves from isolated neutron stars using Advanced LIGO and Advanced Virgo O3 data. *Phys. Rev. D*, 106(10):102008, 2022, 2201.00697.

[22] R. Abbott et al. Search for Gravitational Waves Associated with Gamma-Ray Bursts Detected by Fermi and Swift During the LIGO-Virgo Run O3a. *Astrophys. J.*, 915(2):86, 2021, 2010.14550.

[23] R. Abbott et al. Search for Gravitational Waves Associated with Gamma-Ray Bursts Detected by Fermi and Swift during the LIGO–Virgo Run O3b. *Astrophys. J.*, 928(2):186, 2022, 2111.03608.

[24] A. G. Abac et al. GWTC-4.0: Updating the Gravitational-Wave Transient Catalog with Observations from the First Part of the Fourth LIGO-Virgo-KAGRA Observing Run. *arXiv e-prints*, August 2025, 2508.18082.

[25] A. G. Abac et al. Upper Limits on the Isotropic Gravitational-Wave Background from the first part of LIGO, Virgo, and KAGRA's fourth Observing Run. *arXiv e-prints*, August 2025, 2508.20721.

[26] A. G. Abac et al. All-sky search for long-duration gravitational-wave transients in the first part of the fourth LIGO-Virgo-KAGRA Observing run. *arXiv e-prints*, July 2025, 2507.12282.

[27] A. G. Abac et al. Search for Continuous Gravitational Waves from Known Pulsars in the First Part of the Fourth LIGO-Virgo-KAGRA Observing Run. *Astrophys. J.*, 983(2):99, 2025, 2501.01495.

[28] A. G. Abac et al. All-sky search for short gravitational-wave bursts in the first part of the fourth LIGO-Virgo-KAGRA observing run. *arXiv e-prints*, July 2025, 2507.12374.

[29] Michele Maggiore. Gravitational wave experiments and early universe cosmology. *Physics Reports*, 331(6):283–367, 2000.

[30] Tania Regimbau. The astrophysical gravitational wave stochastic background. *Research in Astronomy and Astrophysics*, 11(4):369–390, mar 2011.

[31] T. Regimbau and J. A. de Freitas Pacheco. Stochastic background from coalescences of neutron star–neutron star binaries. *The Astrophysical Journal*, 642(1):455–461, may 2006.

[32] Xing-Jiang Zhu, E. Howell, T. Regimbau, D. Blair, and Zong-Hong Zhu. Stochastic gravitational wave background from coalescing binary black holes. *The Astrophysical Journal*, 739(2):86, sep 2011.

[33] S. Marassi, R. Schneider, G. Corvino, V. Ferrari, and S. Portegies Zwart. Imprint of the merger and ring-down on the gravitational wave background from black hole binaries coalescence. *Phys. Rev. D*, 84:124037, Dec 2011.

[34] Pablo A. Rosado. Gravitational wave background from binary systems. *Phys. Rev. D*, 84:084004, Oct 2011.

[35] T Regimbau and V Mandic. Astrophysical sources of a stochastic gravitational-wave background. *Classical and Quantum Gravity*, 25(18):184018, sep 2008.

[36] C. Wu, V. Mandic, and T. Regimbau. Accessibility of the gravitational-wave background due to binary coalescences to second and third generation gravitational-wave detectors. *Phys. Rev. D*, 85:104024, May 2012.

[37] B. P. Abbott et al. GW150914: Implications for the stochastic gravitational wave background from binary black holes. *Phys. Rev. Lett.*, 116(13):131102, 2016, 1602.03847.

[38] Benjamin P. Abbott et al. GW170817: Implications for the Stochastic Gravitational-Wave Background from Compact Binary Coalescences. *Phys. Rev. Lett.*, 120(9):091101, 2018, 1710.05837.

[39] David M. Coward, Ronald R. Burman, and David G. Blair. Simulating a stochastic background of gravitational waves from neutron star formation at cosmological distances. *Mon. Not. Roy. Astron. Soc.*, 329:411–416, 2002.

[40] Stefania Marassi, Raffaella Schneider, and Valeria Ferrari. Gravitational wave backgrounds and the cosmic transition from Population III to Population II stars. *Mon. Not. Roy. Astron. Soc.*, 398:293, 2009, 0906.0461.

[41] Pearl Sandick, Keith A. Olive, Frederic Daigne, and Elisabeth Vangioni. Gravitational waves from the first stars. *Phys. Rev. D*, 73:104024, May 2006.

[42] Alessandra Buonanno, Gunter Sigl, Georg G. Raffelt, Hans-Thomas Janka, and Ewald Muller. Stochastic gravitational-wave background from cosmological supernovae. *Phys. Rev. D*, 72:084001, Oct 2005.

[43] K. Crocker, V. Mandic, T. Regimbau, K. Belczynski, W. Gladysz, K. Olive, T. Prestegard, and E. Vangioni. Model of the stochastic gravitational-wave background due to core collapse to black holes. *Phys. Rev. D*, 92:063005, Sep 2015.

[44] Kyle Crocker, Tanner Prestegard, Vuk Mandic, Tania Regimbau, Keith Olive, and Elisabeth Vangioni. Systematic study of the stochastic gravitational-wave background due to stellar core collapse. *Phys. Rev. D*, 95:063015, Mar 2017.

[45] Bella Finkel, Haakon Andresen, and Vuk Mandic. Stochastic gravitational-wave background from stellar core-collapse events. *Phys. Rev. D*, 105:063022, Mar 2022.

[46] Curt Cutler. Gravitational waves from neutron stars with large toroidal *b* fields. *Phys. Rev. D*, 66:084025, Oct 2002.

[47] S. Bonazzola and E. Gourgoulhon. Gravitational waves from pulsars: emission by the magnetic field induced distortion. *Astron. Astrop.*, 312:675, 1996.

[48] Stefania Marassi et al. Stochastic background of gravitational waves emitted by magnetars. *Mon. Not. Roy. Astron. Soc.*, 411:2549, 2011, 1009.1240.

[49] Benjamin J. Owen, Lee Lindblom, Curt Cutler, Bernard F. Schutz, Alberto Vecchio, and Nils Andersson. Gravitational waves from hot young rapidly rotating neutron stars. *Phys. Rev. D*, 58:084020, Sep 1998.

[50] Cheng-Jian Wu, Vuk Mandic, and Tania Regimbau. Accessibility of the stochastic gravitational wave background from magnetars to the interferometric gravitational wave detectors. *Phys. Rev. D*, 87:042002, Feb 2013.

[51] R. R. Caldwell and B. Allen. Cosmological constraints on cosmic-string gravitational radiation. *Phys. Rev. D.*, 45:3447, 1992.

[52] T. Damour and A. Vilenkin. Gravitational Wave Bursts from Cosmic Strings. *Physical Review Letters*, 85:3761–3764, October 2000, gr-qc/0004075.

[53] T. Damour and A. Vilenkin. Gravitational radiation from cosmic (super)strings: Bursts, stochastic background, and observational windows. *Phys. Rev. D.*, 71(6):063510, March 2005, hep-th/0410222.

[54] X. Siemens, V. Mandic, and J. Creighton. Gravitational-Wave Stochastic Background from Cosmic Strings. *Physical Review Letters*, 98(11):111101, March 2007, astro-ph/0610920.

[55] S. Ölmez, V. Mandic, and X. Siemens. Gravitational-wave stochastic background from kinks and cusps on cosmic strings. *Phys. Rev. D.*, 81(10):104028, May 2010, 1004.0890.

[56] Edmund J Copeland, Robert C Myers, and Joseph Polchinski. Cosmic f- and d-strings. *Journal of High Energy Physics*, 2004(06):013–013, jun 2004.

[57] Xavier Siemens, Jolien Creighton, Irit Maor, Saikat R. Majumder, Kipp Cannon, and Jocelyn Read. Gravitational wave bursts from cosmic (super)strings: Quantitative analysis and constraints. *Phys. Rev. D.*, 73(10):105001, May 2006, gr-qc/0603115.

[58] Larissa Lorenz, Christophe Ringeval, and Mairi Sakellariadou. Cosmic string loop distribution on all length scales and at any redshift. *JCAP*, 2010(10):003, Oct 2010, 1006.0931.

[59] Jose J. Blanco-Pillado, Ken D. Olum, and Benjamin Shlaer. Number of cosmic string loops. *Phys. Rev. D.*, 89(2):023512, Jan 2014, 1309.6637.

[60] R. Abbott et al. Constraints on cosmic strings using data from the third Advanced LIGO–Virgo observing run. *Phys. Rev. Lett.*, 126:241102, Jun 2021.

[61] Alexander C. Jenkins and Mairi Sakellariadou. Anisotropies in the stochastic gravitational-wave background: Formalism and the cosmic string case. *Phys. Rev.*, D98(6):063509, 2018, 1802.06046.

[62] E. Witten. Cosmic separation of phases. *Phys. Rev. D.*, 30:272–285, July 1984.

[63] C. J. Hogan. Gravitational radiation from cosmological phase transitions. *Mon. Not. Roy. Astron. Soc.*, 218:629–636, 1986.

[64] A. Kosowsky, M. S. Turner, and R. Watkins. Gravitational waves from first-order cosmological phase transitions. *Physical Review Letters*, 69:2026–2029, October 1992.

[65] Chiara Caprini, Ruth Durrer, and Géraldine Servant. Gravitational wave generation from bubble collisions in first-order phase transitions: An analytic approach. *Phys. Rev. D.*, 77(12):124015, Jun 2008, 0711.2593.

[66] Pierre Binétruy, Alejandro Bohé, Chiara Caprini, and Jean-François Dufaux. Cosmological backgrounds of gravitational waves and eLISA/NGO: phase transitions, cosmic strings and other sources. *JCAP*, 2012(6):027, Jun 2012, 1201.0983.

[67] Chiara Caprini et al. Science with the space-based interferometer eLISA. II: gravitational waves from cosmological phase transitions. *JCAP*, 2016(4):001, Apr 2016, 1512.06239.

[68] M. Fitz Axen, S. Banagiri, A. Matas, C. Caprini, and V. Mandic. Multiwavelength observations of cosmological phase transitions using LISA and Cosmic Explorer. *Phys. Rev. D.*, 98(10):103508, November 2018, 1806.02500.

[69] Carlo R. Contaldi. Anisotropies of Gravitational Wave Backgrounds: A Line Of Sight Approach. *Phys. Lett.*, B771:9–12, 2017, 1609.08168.

[70] Giulia Cusin, Cyril Pitrou, and Jean-Philippe Uzan. Anisotropy of the astrophysical gravitational wave background: Analytic expression of the angular power spectrum and correlation with cosmological observations. *Phys. Rev. D*, 96(10):103019, 2017, 1704.06184.

[71] Giulia Cusin, Cyril Pitrou, and Jean-Philippe Uzan. The signal of the gravitational wave background and the angular correlation of its energy density. *Phys. Rev. D*, 97(12):123527, 2018, 1711.11345.

[72] Giulia Cusin and Gianmassimo Tasinato. Doppler boosting the stochastic gravitational wave background. *JCAP*, 08(08):036, 2022, 2201.10464.

[73] Adrian Ka-Wai Chung, Alexander C. Jenkins, Joseph D. Romano, and Mairi Sakellariadou. Targeted search for the kinematic dipole of the gravitational-wave background. *Phys. Rev. D*, 106:082005, Oct 2022.

[74] B. P. Abbott et al. Supplement: The Rate of Binary Black Hole Mergers Inferred from Advanced LIGO Observations Surrounding GW150914. *Astrophys. J. Suppl.*, 227(2):14, 2016, 1606.03939.

[75] B. P. Abbott et al. GW151226: Observation of Gravitational Waves from a 22-Solar-Mass Binary Black Hole Coalescence. *Phys. Rev. Lett.*, 116(24):241103, 2016, 1606.04855.

[76] Benjamin P. Abbott et al. GW170104: Observation of a 50-Solar-Mass Binary Black Hole Coalescence at Redshift 0.2. *Phys. Rev. Lett.*, 118(22):221101, 2017, 1706.01812.

[77] B. P. Abbott et al. GW170608: Observation of a 19-solar-mass Binary Black Hole Coalescence. *Astrophys. J.*, 851(2):L35, 2017, 1711.05578.

[78] B. P. Abbott et al. Search for intermediate mass black hole binaries in the first and second observing runs of the Advanced LIGO and Virgo network. *Phys. Rev.*, D100(6):064064, 2019, 1906.08000.

[79] B. P. Abbott et al. On the Progenitor of Binary Neutron Star Merger GW170817. *Astrophys. J.*, 850(2):L40, 2017, 1710.05838.

[80] B. P. Abbott et al. Tests of general relativity with GW150914. *Phys. Rev. Lett.*, 116(22):221101, 2016, 1602.03841.

[81] B. P. Abbott et al. Gravitational Waves and Gamma-rays from a Binary Neutron Star Merger: GW170817 and GRB 170817A. *Astrophys. J.*, 848(2):L13, 2017, 1710.05834.

[82] B. P. Abbott et al. Astrophysical Implications of the Binary Black-Hole Merger GW150914. *Astrophys. J.*, 818(2):L22, 2016, 1602.03846.

[83] B. P. Abbott et al. A gravitational-wave standard siren measurement of the Hubble constant. *Nature*, 551(7678):85–88, 2017, 1710.05835.

[84] B. P. Abbott et al. Estimating the Contribution of Dynamical Ejecta in the Kilonova Associated with GW170817. *Astrophys. J.*, 850(2):L39, 2017, 1710.05836.

[85] B. P. Abbott et al. Search for the isotropic stochastic background using data from Advanced LIGO's second observing run. *Phys. Rev.*, D100(6):061101, 2019, 1903.02886.

[86] J. Aasi et al. Advanced LIGO. *Class. Quant. Grav.*, 32:074001, 2015, 1411.4547.

[87] F. Acernese et al. Advanced Virgo: a second-generation interferometric gravitational wave detector. *Class. Quant. Grav.*, 32(2):024001, 2015, 1408.3978.

[88] Benjamin P. Abbott et al. Directional Limits on Persistent Gravitational Waves from Advanced LIGO's First Observing Run. *Phys. Rev. Lett.*, 118(12):121102, 2017, 1612.02030.

[89] B. P. Abbott et al. Prospects for Observing and Localizing Gravitational-Wave Transients with Advanced LIGO, Advanced Virgo and KAGRA. *Living Rev. Rel.*, 21(1):3, 2018, 1304.0670.

[90] Rory Smith and Eric Thrane. Optimal Search for an Astrophysical Gravitational-Wave Background. *Phys. Rev.*, X8(2):021019, 2018, 1712.00688.

[91] Alexander C. Jenkins, Mairi Sakellariadou, Tania Regimbau, and Eric Slezak. Anisotropies in the astrophysical gravitational-wave background: Predictions for the detection of compact binaries by LIGO and Virgo. *Phys. Rev.*, D98(6):063501, 2018, 1806.01718.

[92] Alexander C. Jenkins, Richard O'Shaughnessy, Mairi Sakellariadou, and Daniel Wysocki. Anisotropies in the astrophysical gravitational-wave background: The impact of black hole distributions. *Phys. Rev. Lett.*, 122(11):111101, 2019, 1810.13435.

[93] Alexander C. Jenkins and Mairi Sakellariadou. Shot noise in the astrophysical gravitational-wave background. *Phys. Rev.*, D100(6):063508, 2019, 1902.07719.

[94] Alexander C. Jenkins, Joseph D. Romano, and Mairi Sakellariadou. Estimating the angular power spectrum of the gravitational-wave background in the presence of shot noise. *Phys. Rev.*, D100(8):083501, 2019, 1907.06642.

[95] Daniele Bertacca, Angelo Ricciardone, Nicola Bellomo, Alexander C. Jenkins, Sabino Matarrese, Alvise Raccanelli, Tania Regimbau, and Mairi Sakellariadou. Projection effects on the observed angular spectrum of the astrophysical stochastic gravitational wave background. *Phys. Rev. D*, 101(10):103513, 2020, 1909.11627.

[96] Giulia Cusin, Irina Dvorkin, Cyril Pitrou, and Jean-Philippe Uzan. First predictions of the angular power spectrum of the astrophysical gravitational wave background. *Phys. Rev. Lett.*, 120:231101, 2018, 1803.03236.

[97] Giulia Cusin, Irina Dvorkin, Cyril Pitrou, and Jean-Philippe Uzan. Comment on the article "anisotropies in the astrophysical gravitational-wave background: The impact of black hole distributions" by a.c. jenkins et al. [arxiv:1810.13435]. *arXiv e-prints*, page arXiv:1811.03582, November 2018, 1811.03582.

[98] Giulia Cusin, Irina Dvorkin, Cyril Pitrou, and Jean-Philippe Uzan. Properties of the stochastic astrophysical gravitational wave background: astrophysical sources dependencies. *Phys. Rev. D*, 100(6):063004, 2019, 1904.07797.

[99] Cyril Pitrou, Giulia Cusin, and Jean Philippe Uzan. Unified view of anisotropies in the astrophysical gravitational-wave background. *Phys. Rev. D*, 101(8):081301(R), 2020, 1910.04645.

[100] Guadalupe Cañas-Herrera, Omar Contigiani, and Valeri Vardanyan. Cross-correlation of the astrophysical gravitational-wave background with galaxy clustering. *arXiv e-prints*, page arXiv:1910.08353, October 2019, 1910.08353.

[101] Richard Stiskalek, John Veitch, and Chris Messenger. Are stellar mass binary black hole mergers isotropically distributed? *arXiv e-prints*, page arXiv:2003.02919, March 2020, 2003.02919.

[102] Marco Cavaglia and Ashini Modi. Two-dimensional correlation function of binary black hole coalescences. *arXiv e-prints*, page arXiv:2005.06004, May 2020, 2005.06004.

[103] Ethan Payne, Sharan Banagiri, Paul Lasky, and Eric Thrane. Searching for anisotropy in the distribution of binary black hole mergers. *arXiv e-prints*, page arXiv:2006.11957, June 2020, 2006.11957.

[104] Michael Geller, Anson Hook, Raman Sundrum, and Yuhsin Tsai. Primordial Anisotropies in the Gravitational Wave Background from Cosmological Phase Transitions. *Phys. Rev. Lett.*, 121(20):201303, 2018, 1803.10780.

[105] Giulio Scelfo, Nicola Bellomo, Alvise Raccanelli, Sabino Matarrese, and Licia Verde. GW×LSS: chasing the progenitors of merging binary black holes. *JCAP*, 2018(9):039, September 2018, 1809.03528.

[106] Toshiya Namikawa, Atsushi Nishizawa, and Atsushi Taruya. Anisotropies of gravitational-wave standard sirens as a new cosmological probe without redshift information. *Phys. Rev. Lett.*, 116(12):121302, 2016, 1511.04638.

[107] Masamune Oguri. Measuring the distance-redshift relation with the cross-correlation of gravitational wave standard sirens and galaxies. *Phys. Rev. D*, 93(8):083511, 2016, 1603.02356.

[108] Suvodip Mukherjee, Benjamin D. Wandelt, and Joseph Silk. Probing the theory of gravity with gravitational lensing of gravitational waves and galaxy surveys. *Mon. Not. Roy. Astron. Soc.*, 494(2):1956–1970, 2020, 1908.08951.

[109] Suvodip Mukherjee and Benjamin D. Wandelt. Beyond the classical distance-redshift test: cross-correlating redshift-free standard candles and sirens with redshift surveys. *arXiv e-prints*, page arXiv:1808.06615, August 2018, 1808.06615.

[110] Suvodip Mukherjee and Joseph Silk. Time-dependence of the astrophysical stochastic gravitational wave background. *Mon. Not. Roy. Astron. Soc.*, 491(4):4690–4701, 2020, 1912.07657.

[111] Eric Thrane, Stefan Ballmer, Joseph D. Romano, Sanjit Mitra, Dipongkar Talukder, Sukanta Bose, and Vuk Mandic. Probing the anisotropies of a stochastic gravitational-wave background using a network of ground-based laser interferometers. *Phys. Rev.*, D80:122002, 2009, 0910.0858.

[112] B. P. Abbott et al. Directional limits on persistent gravitational waves using data from Advanced LIGO's first two observing runs. *Phys. Rev.*, D100(6):062001, 2019, 1903.08844.

[113] N. Christensen. Measuring the stochastic gravitational radiation background with laser interferometric antennas. *Phys. Rev.*, D46:5250–5266, 1992.

[114] Joseph D. Romano and Neil J. Cornish. Detection methods for stochastic gravitational-wave backgrounds: a unified treatment. *Living Rev. Rel.*, 20(1):2, 2017, 1608.06889.

[115] Romina Ahumada et al. The 16th Data Release of the Sloan Digital Sky Surveys: First Release from the APOGEE-2 Southern Survey and Full Release of eBOSS Spectra. *Ap. J. Suppl.*, 249(1):3, July 2020, 1912.02905.

[116] Y. Wang, R. J. Brunner, and J. C. Dolence. The SDSS galaxy angular two-point correlation function. *MNRAS*, 432(3):1961–1979, July 2013, 1303.2432.

[117] Beth Reid et al. SDSS-III Baryon Oscillation Spectroscopic Survey Data Release 12: galaxy target selection and large scale structure catalogues. *Mon. Not. Roy. Astron. Soc.*, 455(2):1553–1573, 2016, 1509.06529.

[118] Ashley J. Ross et al. The clustering of galaxies in the completed SDSS-III Baryon Oscillation Spectroscopic Survey: Observational systematics and baryon acoustic oscillations in the correlation function. *Mon. Not. Roy. Astron. Soc.*, 464(1):1168–1191, 2017, 1607.03145.

[119] Krzysztof M. Gorski, Benjamin D. Wandelt, Frode K. Hansen, Eric Hivon, and Anthony J. Banday. The HEALPix Primer. *arXiv e-prints*, pages astro–ph/9905275, May 1999, astro-ph/9905275.

[120] P. A. R. Ade et al. Planck 2013 results. XXX. Cosmic infrared background measurements and implications for star formation. *Astron. Astrophys.*, 571:A30, 2014, 1309.0382.

[121] Planck Collaboration. Planck 2018 results. V. CMB power spectra and likelihoods. *arXiv e-prints*, page arXiv:1907.12875, July 2019, 1907.12875.

[122] Daniel A. Schwartz. The Development and scientific impact of the Chandra X-ray Observatory. *Int. J. Mod. Phys.*, D13:1239–1248, 2004, astro-ph/0402275.

[123] P. Paykari et al. Euclid preparation. VI. Verifying the Performance of Cosmic Shear Experiments (Corrigendum). *Astron. Astrophys.*, 638:C2, June 2020.

[124] Phillip M. Korngut et al. SPHEREx: an all-sky NIR spectral survey. In *Proceedings of SPIE*, volume 10698 of *Society of Photo-Optical Instrumentation Engineers (SPIE) Conference Series*, page 106981U, July 2018.

[125] Gregory Ashton, Eric Thrane, and Rory J. E. Smith. Gravitational wave detection without boot straps: a Bayesian approach. *Phys. Rev.*, D100(12):123018, 2019, 1909.11872.

[126] Sharan Banagiri, Vuk Mandic, Claudia Scarlata, and Kate Z. Yang. Measuring angular N-point correlations of binary black-hole merger gravitational-wave events with hierarchical Bayesian inference. *arXiv e-prints*, page arXiv:2006.00633, May 2020, 2006.00633.

[127] Giulia Cusin, Irina Dvorkin, Cyril Pitrou, and Jean-Philippe Uzan. Stochastic gravitational wave background anisotropies in the mHz band: astrophysical dependencies. *Mon. Not. Roy. Astron. Soc.*, 493(1):L1–L5, 2020, 1904.07757.

[128] Giulia Cusin, Ruth Durrer, and Pedro G. Ferreira. Polarization of a stochastic gravitational wave background through diffusion by massive structures. *Phys. Rev. D*, 99(2):023534, 2019, 1807.10620.

[129] David Alonso, Giulia Cusin, Pedro G. Ferreira, and Cyril Pitrou. Detecting the anisotropic astrophysical gravitational wave background in the presence of shot noise through cross-correlations. *Phys. Rev. D*, 102(2):023002, 2020, 2002.02888.

[130] Kate Ziyan Yang, Vuk Mandic, Claudia Scarlata, and Sharan Banagiri. Searching for Cross-Correlation Between Stochastic Gravitational Wave Background and Galaxy Number Counts. *Mon. Not. Roy. Astron. Soc.*, 500(2):1666–1672, 2020, 2007.10456.

[131] Giulia Capurri, Andrea Lapi, Carlo Baccigalupi, Lumen Boco, Giulio Scelfo, and Tommaso Ronconi. Intensity and anisotropies of the stochastic gravitational wave background from merging compact binaries in galaxies. *JCAP*, 11:032, 2021, 2103.12037.

[132] David W. Hogg. Distance measures in cosmology. *arXiv e-prints*, May 1999, astro-ph/9905116.

[133] Nico Roos, Eric Sluimer, and Bert van den Broek. Changing Redshifts caused by a Changing Expansion Velocity of the Universe. *arXiv e-prints*, October 2024, 2410.08741. arXiv:2410.08741.

[134] Edwin E. Salpeter. The Luminosity function and stellar evolution. *Astrophys. J.*, 121:161–167, 1955.

[135] Marco Limongi. Supernovae from massive stars. *arXiv e-prints*, June 2017, 1706.01913. arXiv:1706.01913.

[136] Chris L. Fryer, Krzysztof Belczynski, Grzegorz Wiktorowicz, Michal Dominik, Vicky Kalogera, and Daniel E. Holz. Compact Remnant Mass Function: Dependence on the Explosion Mechanism and Metallicity. *Astrophys. J.*, 749:91, 2012, 1110.1726.

[137] Felipe A. Marin et al. The WiggleZ Dark Energy Survey: constraining galaxy bias and cosmic growth with 3-point correlation functions. *Mon. Not. Roy. Astron. Soc.*, 432:2654, 2013, 1303.6644.

[138] Anais Rassat, Adam Amara, Luca Amendola, Francisco J. Castander, Thomas Kitching, Martin Kunz, Alexandre Refregier, Yun Wang, and Jochen Weller. Deconstructing Baryon Acoustic Oscillations: A Comparison of Methods. *arXiv e-prints*, October 2008, 0810.0003. arXiv:0810.0003.

[139] Anirban Ain, Prathamesh Dalvi, and Sanjit Mitra. Fast Gravitational Wave Radiometry using Data Folding. *Phys. Rev.*, D92(2):022003, 2015, 1504.01714.

[140] LIGO Scientific Collaboration, Virgo Collaboration, and KAGRA Collaboration. Folded data for first three observing runs of Advanced LIGO and Advanced Virgo, March 2022.

[141] N. Aghanim et al. Planck 2018 results. VI. Cosmological parameters. *arXiv e-prints*, page arXiv:1807.06209, Jul 2018, 1807.06209.

[142] Sambit Panda, Swetha Bhagwat, Jishnu Suresh, and Sanjit Mitra. Stochastic gravitational wave background mapmaking using regularized deconvolution. *Phys. Rev. D*, 100(4):043541, 2019, 1905.08276.

[143] Deepali Agarwal, Jishnu Suresh, Sanjit Mitra, and Anirban Ain. Upper limits on persistent gravitational waves using folded data and the full covariance matrix from Advanced LIGO's first two observing runs. *Phys. Rev. D*, 104(12):123018, 2021, 2105.08930.

[144] Erik Floden, Vuk Mandic, Andrew Matas, and Leo Tsukada. Angular resolution of the search for anisotropic stochastic gravitational-wave background with terrestrial gravitational-wave detectors. *Phys. Rev. D*, 106(2):023010, 2022, 2203.17141.

[145] Kate Z. Yang, Jishnu Suresh, Giulia Cusin, Sharan Banagiri, Noelle Feist, Vuk Mandic, Claudia Scarlata, and Ioannis Michaloliakos. Measurement of the cross-correlation angular power spectrum between the stochastic gravitational wave background and galaxy overdensity. *Phys. Rev. D*, 108(4):043025, 2023, 2304.07621.

[146] Sanjit Mitra, Sanjeev Dhurandhar, Tarun Souradeep, Albert Lazzarini, Vuk Mandic, Sukanta Bose, and Stefan Ballmer. Gravitational wave radiometry: Mapping a stochastic gravitational wave background. *Phys. Rev. D*, 77:042002, 2008, 0708.2728.

[147] Anirban Ain, Jishnu Suresh, and Sanjit Mitra. Very fast stochastic gravitational wave background map making using folded data. *Phys. Rev.*, D98(2):024001, 2018, 1803.08285.

[148] Jishnu Suresh, Anirban Ain, and Sanjit Mitra. Unified mapmaking for an anisotropic stochastic gravitational wave background. *Phys. Rev. D*, 103:083024, Apr 2021.

[149] R. Abbott et al. Search for anisotropic gravitational-wave backgrounds using data from Advanced LIGO and Advanced Virgo's first three observing runs. *Phys. Rev. D*, 104(2):022005, 2021, 2103.08520.

[150] Deepali Agarwal, Jishnu Suresh, Sanjit Mitra, and Anirban Ain. Angular power spectra of anisotropic stochastic gravitational wave background: developing statistical methods and analyzing data from ground-based detectors. *arXiv e-prints*, page arXiv:2302.12516, February 2023, 2302.12516.

[151] David Alonso, Carlo R. Contaldi, Giulia Cusin, Pedro G. Ferreira, and Arianna I. Renzini. Noise angular power spectrum of gravitational wave background experiments. *Phys. Rev. D*, 101(12):124048, 2020, 2005.03001.

[152] S. R. Hinton. ChainConsumer. *The Journal of Open Source Software*, 1:00045, August 2016.

[153] Marco Bruni, Robert Crittenden, Kazuya Koyama, Roy Maartens, Cyril Pitrou, and David Wands. Disentangling non-Gaussianity, bias and GR effects in the galaxy distribution. *Phys. Rev. D*, 85:041301(R), 2012, 1106.3999.

[154] M Punturo et al. The einstein telescope: a third-generation gravitational wave observatory. *Classical and Quantum Gravity*, 27(19), 2010.

[155] B.P. Abbott et al. Exploring the sensitivity of next generation gravitational wave detectors. *Classical and Quantum Gravity*, 34(4):044001, jan 2017.

[156] Euclid Collaboration: F.J. Castander et al. Euclid: V. The Flagship galaxy mock catalogue: A comprehensive simulation for the Euclid mission. *Astron. Astrophys.*, 697:A5, May 2025, 2405.13495.

[157] R. Abbott et al. Population of Merging Compact Binaries Inferred Using Gravitational Waves through GWTC-3. *Phys. Rev. X*, 13(1):011048, 2023, 2111.03634.

[158] P. Ajith et al. Inspiral-merger-ringdown waveforms for black-hole binaries with non-precessing spins. *Phys. Rev. Lett.*, 106:241101, 2011, 0909.2867.

[159] P. Tallada, J. Carretero, J. Casals, C. Acosta-Silva, S. Serrano, M. Caubet, F.J. Castander, E. César, M. Crocce, M. Delfino, M. Eriksen, P. Fosalba, E. Gaztañaga, G. Merino, C. Neissner, and N. Tonello. Cosmohub: Interactive exploration and distribution of astronomical data on hadoop. *Astronomy and Computing*, 32:100391, 2020.

[160] J. Carretero, P. Tallada, J. Casals, M. Caubet, F. Castander, L. Blot, A. Alarcón, S. Serrano, P. Fosalba, C. Acosta-Silva, N. Tonello, F. n. Torradeflot, M. Eriksen, C. Neissner, and M. Delfino. CosmoHub and SciPIC: Massive cosmological data analysis, distribution and generation using a Big Data platform. In *Proceedings of the European Physical Society Conference on High Energy Physics. 5-12 July*, page 488, July 2017.

[161] Alvio Renzini. Stellar population diagnostics of elliptical galaxy formation. *Ann. Rev. Astron. Astrophys.*, 44:141–192, 2006, astro-ph/0603479.

[162] Daniel Thomas, Claudia Maraston, Ralf Bender, and Claudia Mendes de Oliveira. The Epochs of Early-Type Galaxy Formation as a Function of Environment. *The Astrophysical Journal*, 621(2):673–694, March 2005, astro-ph/0410209.

[163] Charlotte A. Mason, Michele Trenti, and Tommaso Treu. The galaxy uv luminosity function before the epoch of reionization. *The Astrophysical Journal*, 813(1):21, oct 2015.

[164] E. Vangioni, K. A. Olive, T. Prestegard, J. Silk, P. Petitjean, and V. Mandic. The Impact of Star Formation and Gamma-Ray Burst Rates at High Redshift on Cosmic Chemical Evolution and Reionization. *Mon. Not. Roy. Astron. Soc.*, 447:2575, 2015, 1409.2462.

[165] Piero Madau and Mark Dickinson. Cosmic Star-Formation History. *Annual Review of Astronomy and Astrophysics*, 52:415–486, August 2014, 1403.0007.

[166] Benedikt Diemer, Martin Sparre, Louis E. Abramson, and Paul Torrey. Log-normal star formation histories in simulated and observed galaxies. *Astrophys. J.*, 839(1):26, 2017, 1701.02308.

[167] R. Abbott et al. Upper limits on the isotropic gravitational-wave background from Advanced LIGO and Advanced Virgo's third observing run. *Phys. Rev. D*, 104(2):022004, 2021, 2101.12130.

[168] Andrea Zonca, Leo Singer, Daniel Lenz, Martin Reinecke, Cyrille Rosset, Eric Hivon, and Krzysztof Gorski. healpy: equal area pixelization and spherical harmonics transforms for data on the sphere in python. *Journal of Open Source Software*, 4(35):1298, March 2019.

[169] K. M. Górski, E. Hivon, A. J. Banday, B. D. Wandelt, F. K. Hansen, M. Reinecke, and M. Bartelmann. HEALPix: A Framework for High-Resolution Discretization and Fast Analysis of Data Distributed on the Sphere. *The Astrophysical Journal*, 622:759–771, April 2005, arXiv:astro-ph/0409513.

[170] Thibaut Louis, Xavier Garrido, Adam Soussana, Matthieu Tristram, Sophie Henrot-Versillé, and Sylvain Vanneste. Consistency of CMB experiments beyond cosmic variance. *Phys. Rev. D*, 100(2):023518, 2019, 1905.06864.